EFFECT OF SOLUTE ELEMENTS ON THE LATTICE PARAMETERS OF MAGNESIUM

By

ANA MARIA BECERRA CORREA

Department of Mining, Metals, and Materials Engineering

McGill University, Montréal, Canada

December 2006

A thesis submitted to the Faculty of Graduate Studies and Research in partial fulfillment of the requirements of the degree of Master of Engineering

Your file Votre référence
ISBN: 978-0-494-32579-7
Our file Notre référence
ISBN: 978-0-494-32579-7

ABSTRACT

Magnesium has limited formability at room temperature due to the hexagonal close-packed (hcp) structure with an axial (c/a) ratio of 1.6240 which provides only basal slip activation. Other hcp metals with different c/a ratios such as titanium have non-basal slip at room temperature. It can be postulated that changing the c/a can change the balance of deformation mechanisms and influence formability. Solutes are known to change the lattice parameters of a metal if in solid solution and hence affect deformation behavior. The objective of this project was to determine the effects of solute additions on the c/a ratio of magnesium and to attempt and assess the resulting deformation behavior.

Changes to the lattice parameters of magnesium with addition of solute elements, Ce, Li, In, and Zn, have been investigated. Binary solid solution alloys as well as multicomponent alloys were cast in permanent copper moulds and homogenized at temperatures between 375°C and 400°C. Annealed powder specimens were prepared and lattice parameters measured using a Philips PW1710 powder diffractometer with Cu-α radiation. The experimental X-ray diffraction (XRD) results were refined and analyzed by means of the Rietveld method while characterization of the alloys was performed with optical and scanning electron microscopy and electron probe microanalysis.

The effects of solutes on lattice parameters were explained on the basis of atom size differences and the change in electron overlap of magnesium due solute additions. It was found that addition of a lower valent solute such as Li caused a contraction of the lattice parameters and a resulting axial ratio decrease. Addition of Indium, however, resulted in a contraction of the lattice parameters, but an increase in the axial ratio due to its higher valency. Conversely, neither Zn nor Ce was found to have an effect on the axial ratio.

Characterization of the binary alloys revealed grain size can vary with the type and the amount of solute present in the pure Mg. Zinc was found decrease the

grain size of Mg even at low solute content, while the Li and In concentrations had to be increased in order to achieve the same degree of grain refinement. Significant grain refinement was also observed with low Ce additions, mostly because of the presence of Ce-rich second phases.

Preliminary deformation tests were also carried out on three different alloys in order to see if changes to the axial ratio affected formability. Rolling and compression tests revealed that alloys with a finer as-cast microstructure resulted in more consistent flow curve shapes and smoother compressed surfaces.

RÉSUMÉ

Le magnésium a une formabilité limitée à cause de sa structure hexagonale compacte ce qui lui confère un rapport axial (c/a) de 1.6240 et qui permet ainsi une modification structurale seulement au niveau du plan de glissement de base. D'autres métaux avec une structure hexagonale compacte possédant des rapports axiaux différents tel que le titane n'ont pas de plan de glissement de base à la température ambiante. Ainsi, il est possible de postuler que la variation du rapport c/a peut alors modifier la balance des mécanismes de déformation et influencer par le fait même la formabilité. Les éléments d'additions sont connus pour modifier les paramètres du réseau cristallin dans les alliages à solution solide et ainsi affecter les comportements lors de la déformation. L'objectif de ce projet était de déterminer les effets des éléments d'additions sur le rapport c/a du magnésium et de tenter ainsi de déterminer les comportements résultant lors de la déformation.

Les modifications des paramètres du réseau cristallin du magnésium avec les éléments d'additions tels que le cérium, lithium, l'indium et le zinc ont été analysées. Des alliages binaires avec solution solide et des alliages contenant plusieurs éléments ont été coulés dans des moules permanents fabriqués à partir de cuivre pur et homogénéisés entre 375°C et 400°C dans un four à traitement thermique à convection. Des échantillons de poudre métallique ont été alors préparés et ont été traités thermiquement et les paramètres du réseau cristallin ont été analysés en utilisant un appareil à diffraction de rayons X à poudre de marque Philips PW1710 équipé avec une source de radiation de Cu-α. Les résultats des analyses par diffraction de rayons X ont été raffinés et analysés en utilisant la méthode Rietveld. La caractérisation des alliages a été effectuée par la microscopie optique, la microscopie électronique et la microprobe électronique.

Les effets des éléments d'additions sur les paramètres du réseau cristallin ont été expliqués sur la base de la différence entre la grosseur des atomes et le

chevauchement électronique du magnésium à cause des éléments d'additions. Il a été observé que l'addition d'éléments avec une valence plus basse tel que le lithium a provoqué une contraction des paramètres du réseau cristallin et résultant ainsi d'une diminution du rapport axial. L'addition d'indium a contribué à une contraction des paramètres du réseau cristallin, mais a aussi par la même occasion contribué à l'augmentation du rapport axial à cause d'une valence plus élevée. Par la même occasion, ni le cérium, ni le zinc n'ont démontré des effets sur la modification du rapport c/a.

La caractérisation des alliages binaires a révélé que la grosseur des grains peut varier avec le type et la quantité d'éléments d'additions présents dans le magnésium pur. L'utilisation du zinc a démontré une diminution de la grosseur des grains même lorsque la teneur d'additions était faible. Les concentrations de lithium et d'indium devaient être plus élevées afin d'obtenir le même niveau d'affinage des grains. Un affinage des grains significatif a aussi été observé par l'addition de faibles teneurs en cérium, principalement à cause de la présence de phases riches en cérium.

Des essais préliminaires de déformation ont été effectués sur trois alliages différents dans le but de voir si le changement du rapport axial avait alors un impact sur la formabilité. Les essais de laminage et de compression ont révélés qu'une microstructure plus fine au départ pouvait ainsi résulté par l'obtention de courbes d'écoulement plus uniformes et des surfaces de compression plus douces.

ACKNOWLEDGMENTS

I would like to express my deepest gratitude to my mentor and supervisor, Prof. Mihriban O. Pekguleryuz at McGill University. Her enthusiasm, knowledge, guidance, professionalism, and friendship have inspired me greatly. Secondly, I wish to thank Pierre Vermette for sharing his experience, patience, jolliness, and support with my research project, more specifically in the alloy synthesis.

Many thanks to the members of my team, Xin, Elvi, Luke, Dmytro, and Ying, for making these last two years unforgettable. Together we proved that with a positive spirit and great teamwork it is possible to overcome even the largest obstacles. Keep up the hard work and creative attitude.

I am also grateful for the expert technical assistance and support from the staff and students at McGill University's Department of Mining, Metals and Materials Engineering: Special thanks to Monique for her help with x-ray diffraction and to Edwin for his help with the compression equipment. To the rest of the staff I would like to acknowledge them for helping me in one way or another.

I would also like to take the time to thank my sponsors, General Motors of Canada and the Institute of National Sciences and Engineering Research Council of Canada (NSERC) for their financial support

To my good friends, Linda, Geoff, Ehab, Phuong, Laura, Geremi and Vikram thanks for your friendship, laugher, and good times. To Lihong, Lan, Faramarz, Claudio, Guillermo, Abdel, Rocco, Ramona, Graham, Sean and the rest of the graduate students keep up the good work and intellectual curiosity.

Finally, I would also like to thank my husband, Pablo, and my family for their support during this stage of my life.

TABLE OF CONTENTS

LIST OF FIGURES

CHAPTER 2

CHAPTER 3

CHAPTER 4

LIST OF TABLES

CHAPTER 2

CHAPTER 3

CHAPTER 4

CHAPTER 5

CHAPTER 1 - INTRODUCTION

One of the main responsibilities of industrialized nations in the 21st century is to cut down on green house emissions. There are many strategies that have taken place and new technologies are emerging. The automobile industry is doing its part investing in new lightweight materials that can be used in vehicles in an attempt to reduce fuel consumption, hence fuel emissions. Up until now, aluminum has been the material of choice because of its low weight, formability, and resistance to corrosion. Nevertheless, a lot of attention is being drawn towards magnesium since it can provide even greater weight savings. Currently, most of the magnesium produced is either used as an alloying element for aluminum or as die cast components. Production of magnesium sheet has not been fully developed, since the quantity of available Mg wrought alloys is limited and the deformation behavior of the metal is still unclear.

Magnesium, possessing an hcp crystal structure exhibits poor deformation at room temperature due to its limited number of active slip planes. Slip will be favored on those planes where the critical resolved shear stress (CRSS) is relatively low. For hcp metals such as Mg, Cd and Zn, deformation is limited to primary slip on the {0002} basal planes. Given that there is only one set of these planes, the formability at low temperatures for these metals is not high. Activation of the non-basal slip can be accomplished, among others, by increasing the deformation temperature, by decreasing the axial ratio of the hcp crystal structure or by microstructural control.

The addition of solute elements to pure Mg can improve the formability of the metal either by reducing the axial ratio (c/a) or by altering the hexagonal crystal structures to a cubic structure. A decrease in the axial ratio of hexagonal close-packed structures can be accomplished through solid solution alloying where the solutes occupy substitutional spaces in the crystal lattice. Once a solid solution is

formed, changes in lattice parameters can be caused by the size of the solute atom, the solute valency, or a combination of both. Contraction or expansion of the Mg crystal structure will occur if a solute with the same number of valent electrons but differing in atomic size is added. However, if a solute with a different number of valence electrons is added, lattice parameter changes will be attributed to a change in electronic concentration of the crystal structure and the Brillouin zone.

The aim of the present research work is to study the effect solute elements have on the lattice parameters of pure Mg at room temperature. A solute size effect was investigated by adding solutes like Ce and Zn, which have the same number of valence electrons as Mg, but that differ in atomic size. Lithium and indium, however, were added to investigate the effect of electronic concentration since they have a valency of 1 and 3 respectively.

Microstructural changes related to the effect of individual solute element additions were also investigated. Preliminary compression and rolling tests were also carried out on a number of alloys in order to compare their deformation behavior to pure Mg. The aim was to investigate if an axial ratio reduction meant better alloy formability.

CHAPTER 2 - LITERATURE REVIEW

2.1 Background

2.1.1 Advantages and Limitations of Magnesium

Magnesium is the lowest density structural metal (1.738 g/cm^3) and the 8th most abundant element on the earth's crust (2%) [1]. Magnesium's chemical properties make it an optimum alloying element in the production of aluminum alloys, where it is added to improve corrosion resistance and surface finishing. On the other hand, the automotive and aerospace (transport) industries are interested in its structural properties, more specifically its low density and excellent strength-to-weight ratio. Magnesium also possesses high specific strength, good damping capacity, and excellent machinability and castability [2]. Table 2.1 summarizes the major advantages and limitations of magnesium and its alloys.

Table 2.1: Advantages and Limitations of Magnesium and Its Alloys [1]

Advantages	**Disadvantages**
Low density (1.7 g/cm^3)	High Cost
Good Castability	Few Wrought Alloys
Compatible with Iron	Limited Room Temperature Ductility
Excellent Machinability	Highly Reactive Melt
Excellent Strength/Weight ratio	Flammable pure Mg powder
High Thermal Conductivity	High Electrochemical Potential (galvanic corrosion)
High Damping Capacity	
Less Corrosive than Iron	High susceptibility to corrosion
Fully recyclable	No existing secondary market

There is growing interest in using Mg sheet in automobile applications for body panels for weight reduction. However, while cast Mg alloys are used in automobile applications (instrument panels, steering wheels) the use of wrought alloys is limited due to its low formability. Production of magnesium sheet has been difficult due to the fact that the processing technology is not well developed and the deformation properties of magnesium are still unclear [3]. Additionally, the use of magnesium is limited because of its low elastic modulus, cold workability and toughness, creep, and low corrosion resistance [4]. Current research needs to address all these issues in order to successfully produce magnesium alloy sheet with comparable mechanical properties to that of steel and aluminum sheet [3]. Figure 2.1 shows potential uses of Mg in automobile applications.

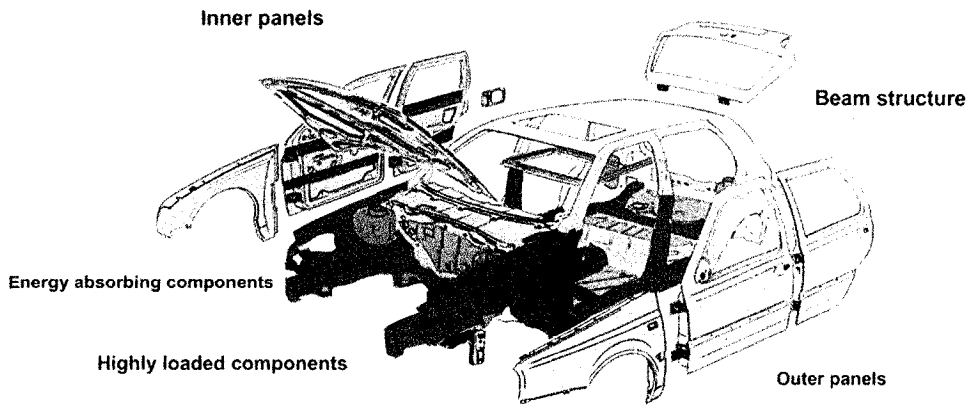

Figure 2.1: Use of Mg in automobile applications

2.1.2 Principal Uses of Magnesium

The general uses of magnesium have been divided into different categories as can be seen in Figure 2.2. For years, due to its highly flammable powder, magnesium has been used in pyrotechnics. During the war years, it was used for flares and tracer bullets. When burned, it produces a bright white light that was also used as a flashlight in photography. As an alloying element, it is used to desulfurize steel, deoxidize copper-base alloys, and to improve the ductility and

strength of cast iron. Nevertheless, about half of all magnesium produced is used as an alloying element in aluminum. Its high electrochemical potential also makes this material useful as a sacrificial anode for boats, water heaters, structures under marine environments, etc. Its structural properties make it attractive for automotive and aeronautical applications where there is a need for weight reduction. In the automotive industry magnesium is mainly used as a cast alloy, but wrought alloys are also finding interest and new technology and materials are being created so as to make it a viable alternative to steel and aluminum in the future [5].

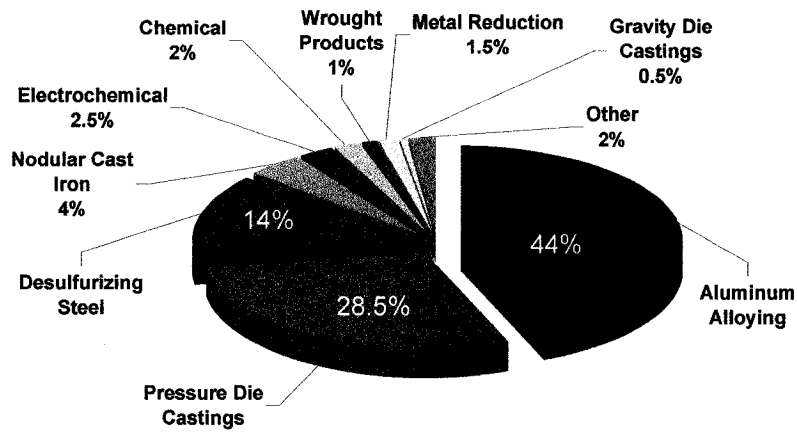

Figure 2.2: Consumption of magnesium in the western world in 1997 (total 333,770 tonnes) [5]

2.2 General Alloying Behavior of Magnesium

2.2.1 Physical and Chemical Properties of Pure Magnesium

Magnesium has a hexagonal crystal lattice where each atom is surrounded by six others. It consists of close-packed basal planes and they are arranged in an ABABAB fashion. The axial ratio is less than the ideal 1.633 since the close-packing is not of perfect spheres. Figure 2.3 illustrates the hexagonal close-packed crystal structure of magnesium with its theoretical dimensions at room temperature.

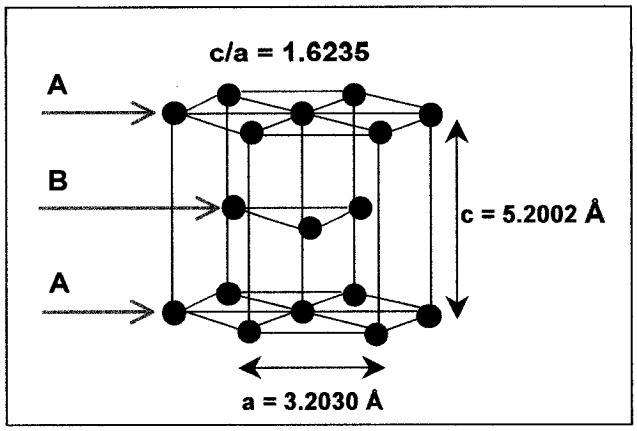

Figure 2.3: Magnesium's hexagonal crystal structure showing the close-packed layers and dimensions at room temperature

The physical metallurgy of magnesium and its alloys is influenced by atomic size and magnesium's atomic diameter is optimum in terms of being able to form extensive solid solutions with a variety of solutes elements, some of which include aluminum, copper, indium, zirconium, and zinc. Other physical and chemical properties of pure magnesium are summarized in Table 2.2.

Table 2.2: Physical Properties of Magnesium [5]

Atomic Number	12
Atomic Weight	24.305
Atomic Radius	0.320 nm
Electronic Structure	$1s^2\,2s^2\,2p^2\,3s^2$
Crystal Structure	hcp
Melting Point	650 °C
Boiling Point	1090 °C
Density at 20 °C	1.738 kg/cc
Electrical Resistivity at 20 °C	4.450 μΩ-cm
Thermal Conductivity at 25 °C	155 W/mK
Linear Expansion Coefficient at 20 °C	$25.2 \times 10^{-6}\ K^{-1}$
Latent Heat of Fusion	370 J/g
Latent Heat of Evaporation	5250 J/g

2.2.2 Alloys

Alloying is extremely important, since pure magnesium is soft and it exhibits low corrosion resistance. Unlike aluminum, the designation of magnesium alloys is easy to understand. Currently there is no international system for the designation, but the American Society for Testing Materials (ASTM) developed a letter and number designation. The classification of magnesium starts with two code letters, which represent the main alloying elements. Table 2.3 lists the code letters used and their representative alloying element.

Table 2.3: ASTM Codes for Magnesium Alloying Elements [6]

Code Letter	Alloying Element	Code Letter	Alloying Element
A	Aluminum	N	Nickel
B	Bismuth	P	Lead
C	Copper	Q	Silver
D	Cadmium	R	Chromium
E	Rare Earths	S	Silicon
F	Iron	T	Titanium
H	Thorium	W	Yttrium
K	Zirconium	Y	Antimony
L	Lithium	Z	Zinc
M	Manganese		

The first letter indicates the alloying element that is present in the highest concentration. The second letter that follows represents the second main alloying addition. Next to the letters one can find two numbers, which represent the nominal composition (in wt %) of the alloying additions; rounded off to the nearest whole number. The first number represents the composition of the first letter and the second number the composition of the second letter. For example, magnesium alloy AZ31 contains 3% aluminum and 1% zinc. Problems with this designation system are that there is no way of giving information about other alloying elements that are intentionally added to improve the alloy. Modifications to the alloy are usually designated by including letters A, B, C, etc that follow the

numbers. These usually explain variations in compositions in the form of impurity levels and if the letter X follows the numbers, it means that the alloy is experimental [5]. Temper designations for magnesium alloys are the same as those for aluminum alloys; these can be found in Table 2.4.

Table 2.4: Temper Designations for Magnesium and Aluminum Alloys

Code	Description
F	As fabricated
O	Annealed, recrystallized (wrought products only)
H1 H2 H3	Strain Hardened only Strain Hardened and then partially annealed Strain Hardened and then stabilized
T1 T2 T3 T4 T5 T6 T7 T8 T9 T10	Cooled and naturally aged Annealed Solution heat treated and then cold worked Solution heat treated and naturally aged Cooled and artificially aged Solution heat treated and artificially aged Solution heat treated and stabilized Solution heat treated, cold worked, and artificially aged Solution heat treated, artificially aged, and cold worked Cooled, artificially aged, and cold worked
W	Solution heat treated (unstable temper)

2.2.3 *Effect of Alloying Elements*

Improving the mechanical properties of magnesium is usually achieved through solid solution hardening and/or precipitation hardening. In addition, alloying additions can also influence the reactivity of the melt, the castability, corrosion properties, and microstructure. The amount of alloying element that can be added to magnesium is controlled by the liquid solubility of the element in the molten state, in addition to the interference between alloying elements [5]. Below, the effect of the alloying elements on the properties of magnesium is discussed with greater detail.

Aluminum: Of all the alloying additions, Al is the most favorable since it improves the mechanical properties, and it expands the freezing range making the alloy more castable [5]. At room temperature Mg can dissolve 2.6 wt% Al and it increases up to a maximum of 12.1 wt% at 436°C. This decreasing solubility from the eutectic temperature makes it possible for the alloy to be heat treated and aged. Improvement of the mechanical properties of magnesium upon addition of aluminum is possible by the formation of a solid solution and the precipitation of the $Mg_{17}Al_{12}$ intermetallic [6]. Nevertheless, one major disadvantage of Al is that it increases microporosity in magnesium alloys. Most commercial Mg-Al alloys contain Al in the range of 2 - 9 wt%, yet the best balance of strength and ductility is found with an addition of only 6 wt%.

Beryllium: It is added to reduce the reactivity of magnesium in its molten state. By adding less than 30 ppm, the oxidation of the melt is reduced to a great extent. Great care has to be taken with Be additions since it is toxic and it can cause allergic reactions in humans.

Calcium: It is added in small amounts to grain refine and improve creep properties. When casting, it is added before it is poured to reduce oxidation of the molten metal as well as during the subsequent heat treatment. Additionally, it improves the rollability of magnesium sheet and creep resistance by forming Ca containing intermetallics [5].

Copper: Its best property is the improvement of the high temperature strength of the alloy. Conversely, when it exceeds 0.05 wt% it becomes detrimental to the corrosion resistance.

Nickel and Iron: Both of these elements are detrimental to the corrosion resistance of magnesium alloys. They are usually present as trace elements.

Lithium: This element has been researched extensively since it can change various physical properties of magnesium. Li has high solid solubility of 5.5 wt%

in magnesium at room temperature, but the most interesting aspect of Li is that upon an increase in concentration (11 wt%) it starts changing the crystal structure from hcp to bcc. This change in crystal structure improves the formability of wrought magnesium alloys by making prismatic slip possible at room temperature [7]. Furthermore, the addition of Li to Mg decreases the density to a lower value than that of pure magnesium. A disadvantage of this element is that upon increasing its concentration it decreases strength and corrosion resistance. So far, Mg-Li alloys have found only limited applications [5].

Manganese: Addition of Mn to the Mg melt causes the Fe to precipitate out in the form of sludge, therefore reducing the corrosion tendency of the alloy. Mn increases yield strength, grain refinement, and weldability. Only 1.5 wt% is soluble in Mg, but in the presence of Al its solubility in Mg further decreases to 0.03 wt%.

Rare Earths: In the past, these were usually added as misch-metal with 50 wt% cerium content, but recently research has been focusing on the individual effect of the different rare earth metals on magnesium. Alloys with cerium and lanthanum have already been studied in the past. Cerium in solid solution with magnesium has been found to decrease the c/a ratio of the hcp crystal, thus improving the formability of wrought magnesium alloys [8]. The addition of rare earths overall, improve the strength of magnesium at elevated temperatures, corrosion resistance, and creep resistance.

Silicon: As in aluminum alloys, silicon is added to magnesium to increase the fluidity of the molten metal. Nevertheless, given that there are traces of Fe present in Si, the corrosion resistance of the metal decreases with the addition of Si to Mg.

Silver: In the presence of rare earths, it increases the high temperature strength and creep resistance. It also increases response to age hardening, thus improving mechanical properties [2].

Thorium: It was found to be the best element to increase high temperature strength and creep resistance. Yet, it is replaced by other elements as a result of its radioactivity.

Zinc: It is considered the second best alloying addition after aluminum. Nonetheless, in terms of castability and strengthening it is as effective as aluminum [6]. It is added to magnesium with a combination of Zr, RE or thorium to produce precipitation-hardenable materials. Alloyed only with aluminum, it increases room temperature strength. In addition, corrosive behavior of Fe and Ni is decreased with addition of Zn.

Zirconium: It is added for grain refinement as well as to increase the tensile strength without a loss of ductility [6]. As stated above, it is added with Zn, RE or thorium in which case it acts as the grain refiner. Zr cannot be used in alloys that contain Al or Mn, given that it will take them out of the solid solution by forming intermetallics with them.

Yttrium: This element is sometimes considered a rare earth metal because it is really similar. It is added to magnesium with the rare earths to improve creep resistance at elevated temperatures. Corrosion properties are also improved.

2.2.4 Main Alloying Elements

There are five basic groups of alloy systems that are currently being used in commercial application and they are based on the major alloying elements: aluminum, zinc, manganese, rare earths (RE), and zirconium [5]. The main systems are as follows:

Mg-Al	Mg-Al-Zn
Mg-Zn-Zr	Mg-Zn-RE-Zr
Mg-Zr	Mg-Mn
Mg-Ag-RE-Zr	Mg-Y-RE-Zr

Alloys containing thorium also exist, and they have found use in the missile and spacecraft industry. Due to the radioactivity of thorium these alloys are now banned.

In general, magnesium alloys are divided into cast and wrought alloys. In the past, research has been conducted mainly on casting alloys. These alloys exhibit a high fluidity and castability making it possible to create thin-walled parts with a high strength to weight ratio. In the aerospace industry magnesium castings are mainly found in gearbox casings and aero engine components, while in the automotive industry magnesium is mainly found in die-cast components like steering wheels, instrument panels, and in some cases power train components [9]. However, in comparison to other metals used in these industries magnesium cast products are limited by their performance at higher temperatures and their lower mechanical properties. The wrought products represent an alternative with advantageous mechanical properties and a finer grained structure without pores. Yet, the market of magnesium wrought alloys has been very limited due to the high cost and limited formability of Mg. Of the total magnesium consumption, about 37% goes into the die-cast shop, while 1.4% is used for wrought products [10]. Cast magnesium products have even replaced aluminum in some applications, due to its lower density and its compatibility with steel dies.

2.3 Wrought Alloys

Magnesium wrought products are produced as sheet, plate, extruded bars, shapes, and tubes, and forgings. The use of wrought products has been limited by the poor deformation characteristics of magnesium at room temperature. Consequently, magnesium alloys have a low production rate, which in turn makes them more expensive than aluminum wrought products. For instance, magnesium extrusions are about 5 to 10 times slower than aluminum extrusions [11]. Even though magnesium has the difficulty of being cold-worked, wrought products can still be hot-worked using almost all the bulk working methods. Products can be forged, rolled and extruded.

Current research has focused much of its attention to the development of new magnesium wrought products and to the understanding of how processes can be altered to improve their deformation [12]. The use of die cast products in cars has been an improvement in weight reduction, but their mechanical properties are not always the best. Alternatively, wrought products have higher levels of strength and ductility, which in turn makes them more appropriate for use in automobile components [13]. Sheet formability is currently the main interest since sheet metal parts make up about 25 % of the vehicle's mass. Replacement of these heavier sheet products with the lightweight magnesium would result in a significant weight reduction and in turn less fuel consumption [14].

2.3.1 Deformation Characteristics

Unlike, steel and aluminum, magnesium possessing a hexagonal close-packed (hcp) crystal structure exhibits poor deformation at room temperature due to its limited number of active slip planes. In both fcc and hcp metals slip occurs preferentially in the close-packed planes along the close-packed directions. Thus at room temperature, the fcc structure contains 12 slip systems of which five are independent, while the hcp structure has only three slip systems of which two are independent [2]. The amount of active slip systems at room temperature explains why it is easier to deform aluminum rather than magnesium, hence the large variety of wrought aluminum alloys and products.

The direction for easy slip glide in hcp metals are three <11 $\bar{2}$0> (or <a> directions) close-packed directions. The set of planes that contain this slip direction are (i) the basal {0002} plane, (ii) the prismatic {10 $\bar{1}$0} set of planes, and (iii) the pyramidal {10 $\bar{1}$1} set of planes [15]. The slip planes and slip directions of hcp metals can be observed in Figure 2.4.

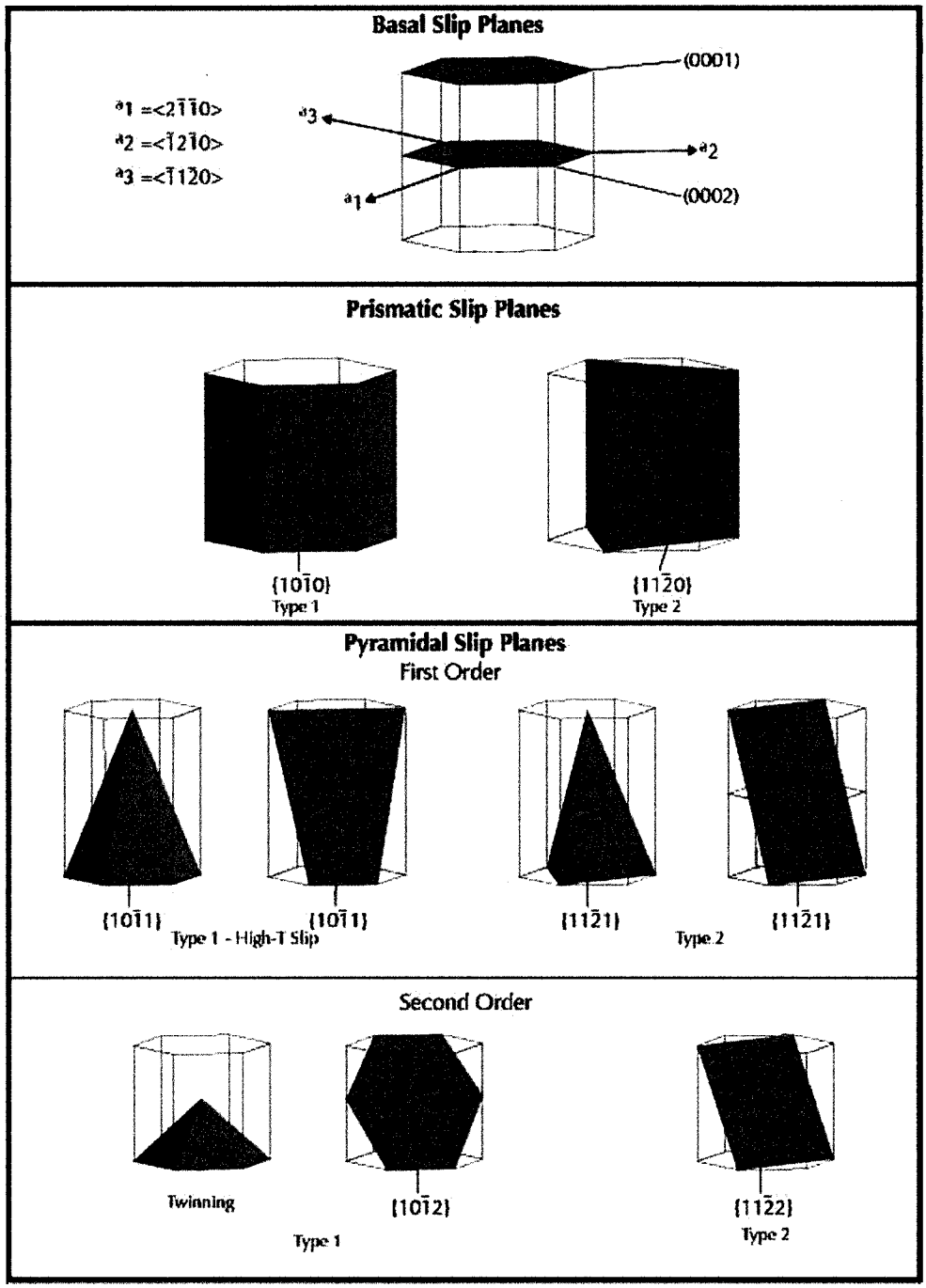

Figure 2.4: Slip planes and slip directions for hcp magnesium [1]

Deformation of hcp metals at room temperature occurs mainly by crystallographic slip and deformation twinning occurring simultaneously. Slip will be favored on those planes where the critical resolved shear stress (CRSS) is relatively low [8].

For hcp metals like Cd, Mg, and Zn, the deformation is limited to primary slip on the {0002} basal planes. Given that there is only one set of basal planes, the plasticity at low temperatures for these metals is not outstanding. On the other hand, Ti, which is also an hcp metal, exhibits a lower CRSS on non-basal planes thus, at low temperatures non-basal slip occurs rather than basal slip. All of these hcp metals deform somewhat differently probably indicating that a relationship between the CRSS and the c/a (axial) ratio of the metal exists [16]. A relationship between the axial ratio and the slip systems of various hcp metals can be observed in Table 2.5.

Table 2.5: Available Slip Systems for hcp Metals at Room Temperature

Metal	Axial Ratio (c/a)	Predominant Slip System	Basal Plane CRSS (psi)
Cd	1.886	$\{0001\} < 11\bar{2}0>$	82
Zn	1.856	$\{0001] < 11\bar{2}0>$	26
Mg	1.624	$\{0001\} < 11\bar{2}0>$	63
Ti	1.588	$\{10\bar{1}0\} < 11\bar{2}0>$	16000

In addition to slip, deformation twinning can also be observed at room temperature, where it occurs on a number of planes. This type of deformation is the dominant mechanism for the inelastic shape changes in the c-axis [15]. Twinning involves the sudden localized shear of small, well-defined regions of material, where it can only accommodate a small amount of deformation occurring mainly on the $\{10\ \bar{1}2\}$ pyramidal set of planes [17]. In some cases, Mg exhibits $\{10\ \bar{1}1\}$ twins and double twinning through $\{10\ \bar{1}2\}$ followed by $\{10\ \bar{1}1\}$ twinning [1]. However, given that the CRSS for the $\{10\ \bar{1}2\}$ twins is the lowest, twinning will occur mainly on this set of planes. Deformation twinning for Mg can be observed in Figure 2.5. However, the direction of the applied stress also influences the twinning behavior of magnesium. For example, if the applied stress is parallel to the basal planes, twinning will only occur in compression, while if the

stress is perpendicular to the basal planes, twinning will occur in tension [1]. As a result, considerable asymmetry is found between the tensile and compressive yield behaviors of textured Mg [18]. This strong tension-compression asymmetry makes magnesium and its alloys suitable for certain structural applications, since they will deform in compression long before in tension [15]. Maximum twinning occurs when the twin planes are oriented around 45° to the stress axis. Therefore, formability of Mg at low temperatures is closely related to the texture of the structure

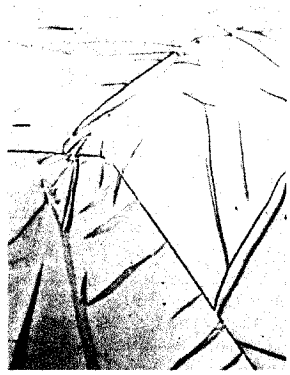

Figure 2.5: Deformation twinning in Mg [1]

It has also been found that {10 $\bar{1}$1} pyramidal planes are active in single crystals at room temperature when the stress axis is within 6° of the basal planes. Furthermore, when the temperature is decreased below room temperature, the {10 $\bar{1}$1} prismatic slip can also occur; most likely since the grain boundary sheering cannot relieve the stresses caused at the grain boundaries [1].

The poor deformation behavior of magnesium at low temperatures is explained by the limited amount of active slip systems. In order to improve plasticity it is necessary to increase the activity of the non-basal slips [19]. Activation of the non-basal slip and other deformation mechanisms can be accomplished, among others, by increasing the deformation temperature both of which decreases CRSS for non-basal slip, by decreasing the axial ratio of the hcp crystal structure or by ultra-refining the grain structure to induce grain boundary deformation.

2.4 Improvement of Formability

The need to replace heavy sheet (steel, aluminum) components in automobiles has focused research into improving the formability of magnesium sheet alloys. In recent years, a vast amount of research has been carried out on AZ31 sheet alloy. It was discovered that as the deformation temperature increases, the formability of the sheet also increases. In addition, much work has been conducted on determining other variables that can affect formability such as strain rate, grain size, texture, and solute elements [14].

2.4.1 Effect of Temperature

Magnesium alloys are much more workable at elevated temperatures, given that activation of non-basal slip systems is temperature dependent. When the temperature is increased from room temperature to 225°C, the {10 $\bar{1}$1} pyramidal slip planes start to operate making it easier for Mg to deform. H. Somekawa et al demonstrated that as the deformation temperature increased, the flow stress decreased, and the elongation increased due to activation of non-basal slip. Figure 2.6, illustrates the results obtained from tensile tests carried out on AZ31 plate samples at temperatures ranging from room temperature to 200°C [21].

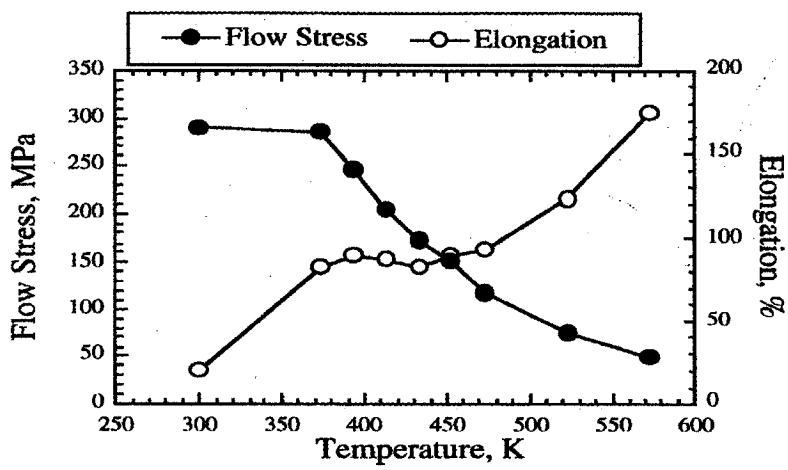

Figure 2.6: The variation of flow stress and elongation with respect to temperature of AZ31 alloy

The activation of such slip planes can be due to the fact that as temperature increases, the CRSS of the non-basal planes decreases so that at 400°C, the CRSS of the prismatic and pyramidal slip systems is only about double that of the basal planes [22]. The effect of temperature on the CRSS for the different slip planes can be observed in Figure 2.7 [23]. It can be seen from the graph that even though the CRSS for slip decreases with temperature, the CRSS for twinning is relatively temperature insensitive.

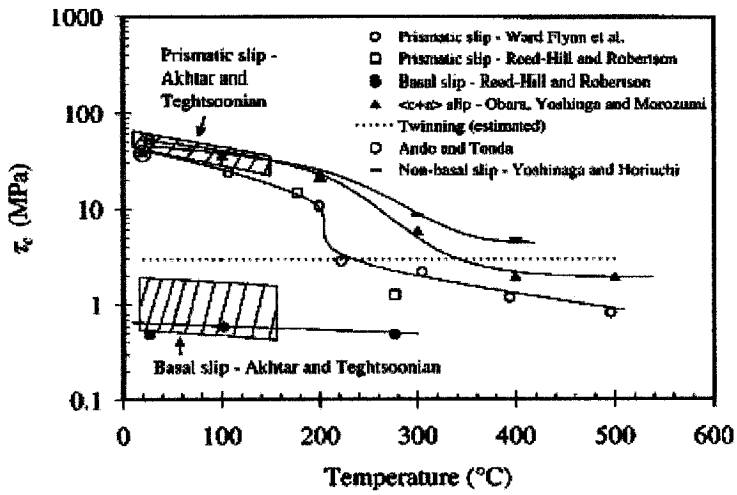

Figure 2.7: Reduction of CRSS with increasing temperature

Figure 2.8 shows cylinders of AZ31 sheet that where compressed at different temperatures. At lower temperatures, when deformed in compression, there is a lack of active slip planes that makes magnesium less ductile and therefore the material can fracture more easily. As the temperature is increased, slip systems are activated and ductility is enhanced.

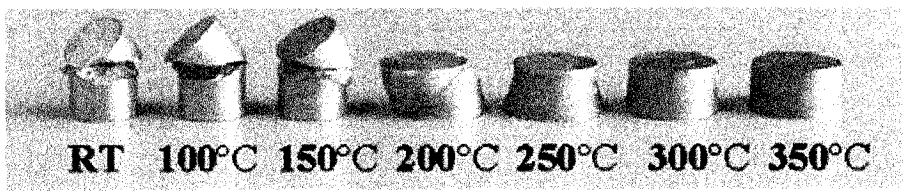

Figure 2.8: Improvement of low ductility of AZ31 sheet in compression with increasing temperature [23]

As well as improving the deformation characteristics in magnesium, the increase in temperature when working the metal has several advantages over cold working. For example, when magnesium alloy parts are extruded at elevated temperatures, there is no need to remove the piece to anneal it. Extrusions can be done in one step thus reducing the time to make the part and the elimination of additional dies for the later stages. Other advantages are low spring back, and less power consumption [5].

2.4.2 *Effect of Strain Rate*

To determine the effect strain rate on formability, E. Doege and K.Droder, performed uniaxial tensile tests at 200°C by using different velocities. It was found that when the strain rate was increased there was a considerable increase in the flow stress [14]. It was also found that by decreasing the temperature, the effect of strain rate was less significant. In addition, the tests show that if the strain rate is raised there is a decrease in elongation at any temperature. To put it briefly, it is known that magnesium alloys can be extremely ductile when they are deformed at high temperatures with a low strain rate. This behavior can be clearly seen in Figure 2.9. It is said that at high temperatures and low straining rates the material becomes superplastic.

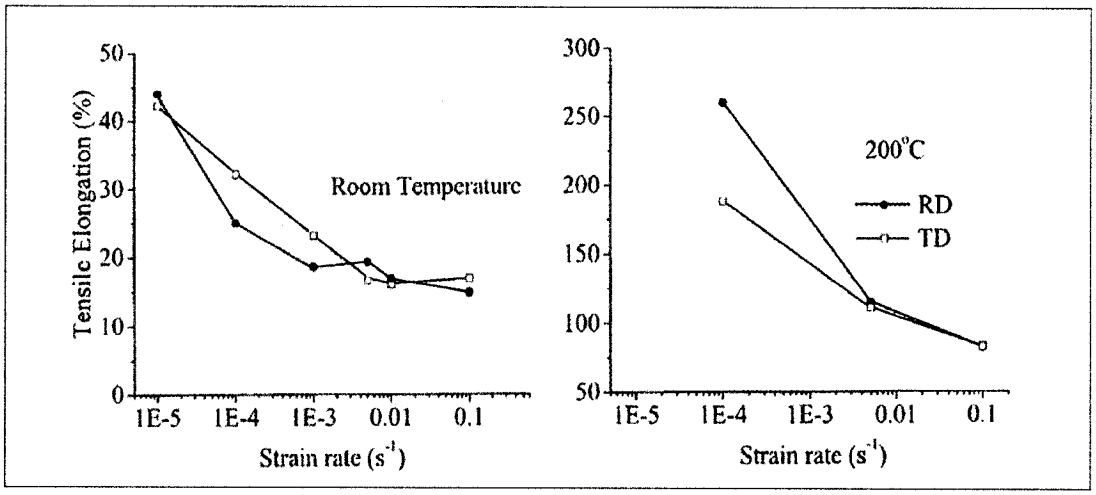

Figure 2.9: Tensile elongation (%) vs. initial strain rate at room temperature and 200°C for rolling and transverse directions [24]

2.4.3 Effect of Texture and Grain Size

The resolved shear stress of the basal plane is dependent on the orientation of the plane with respect to the stress axis. It is found to be at its maximum, when the angle between them is 45°, and it is non-existent when they are either parallel or perpendicular to each other. Therefore, deformation of magnesium at room temperature is also dependent on plastic anisotropy. When magnesium alloys are rolled at room temperature, it produces a strong preferred orientation (texture) at its surface [25]. The basal planes tend to orient parallel to the surface with its [10 $\bar{1}$0] diagonal axis in the rolling direction. The texture that is generated once the material is initially deformed will cause some strengthening, inhibiting further deformation or bending of the metal piece.

R. Agnew et al have studied the formation of double textures formed during rolling of AZ31B and they have found that the strength along the transverse direction (TD) is higher than along the rolling direction (RD) [24]. This anisotropic flow behavior can be observed in Figure 2.10, where tensile samples were tested at different temperatures. In addition, to the difference in the flow stress for both the TD and RD, it was observed that as the temperature of the tensile tests increased, the anisotropy of the flow curves decreased.

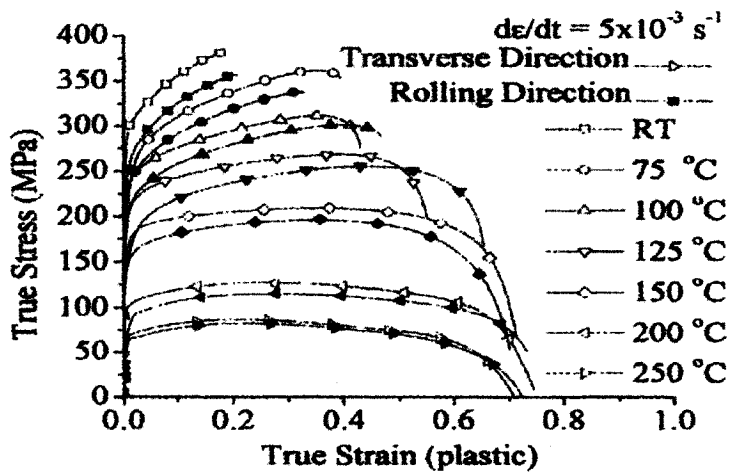

Figure 2.10: Tension flow curves for AZ31B-H24 alloy at 5x10^{-2} s^{-1} for transverse and rolling directions at different temperatures

It is evident that ductility of magnesium at room temperature is dependent on the directionality of the structure (texture). Anisotropic properties can be minimized if the random orientation of the grains is increased through grain refinement [1]. The relationship of tensile ductility with grain size is illustrated in Figure 2.11. It can be clearly seen that as the grain size decreases the ductility of magnesium increases.

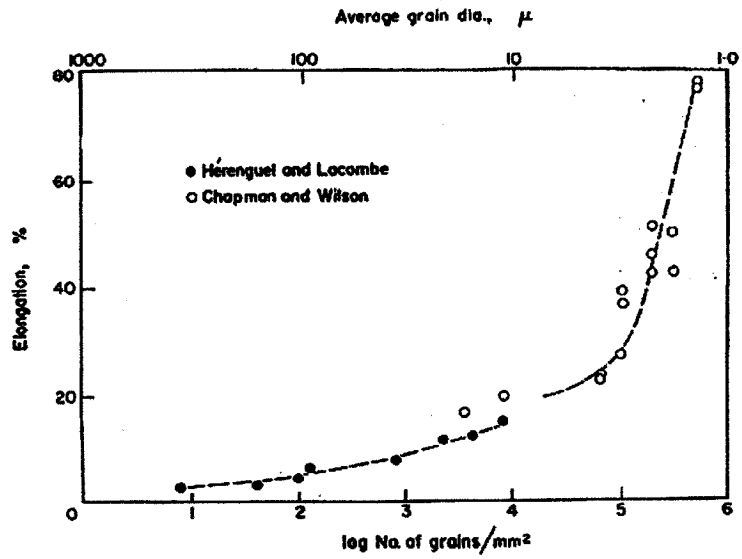

Figure 2.11: The relation between grain size and ductility for pure magnesium.

Grain size reduction has also been linked to changes in the CRSS for both twinning and slip. Meyers et al suggested that a decreasing grain size causes the CRSS for twinning to increase more rapidly than for slip [26]. Hence, a grain size reduction is analogous to an increase in deformation temperature in that there may be a transition from twinning dominated flow to slip dominated flow [27]. Very fine, uniform, grain sized (2 μm) structures have demonstrated unusual room-temperature ductility, as can be observed in Figure 2.12(a). Additionally, grain size refinement also affects the temperature-ductility curve causing it to move towards the left so that the steepening begins at lower temperatures [1]. The effect of grain size of the temperature-ductility curve is observed in Figure 2.12(b).

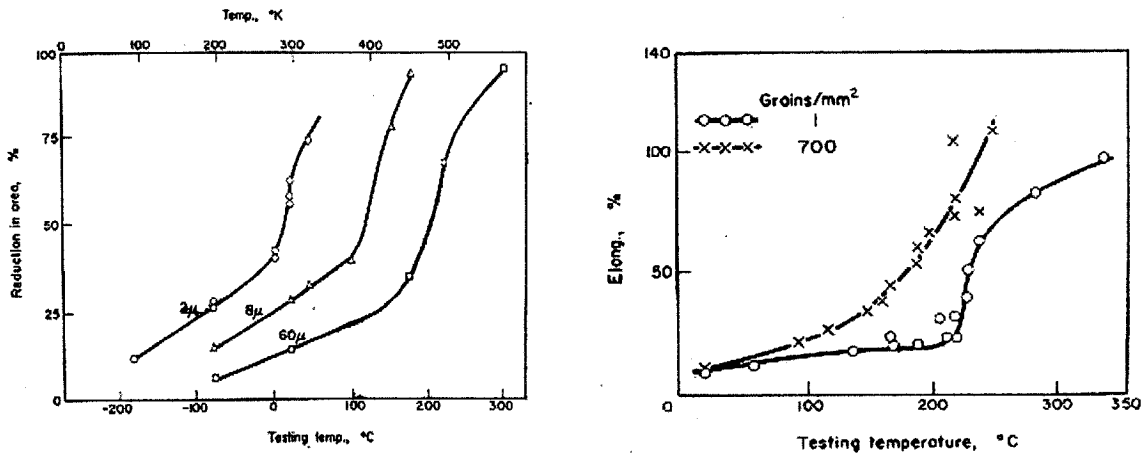

(a) (b)

Figure 2.12: Effect of grain size (a) on the temperature above which ductility increases and (b) on the shape of the ductility temperature curve for pure Mg [1]

2.4.4 Effect of Solutes

The addition of solute elements to pure Mg can improve the formability of the metal either by reducing the axial ratio (c/a) or by altering the hexagonal crystal structures to a cubic structure. Several investigations have shown that lithium is a clear example of a solute that can accomplish both of these tasks [28].

The magnesium-lithium system has been extensively studied for years. These alloys display an even lower density than that of pure magnesium and they display an increased ductility at lower temperatures [30]. From the equilibrium phase diagram (Figure 2.13) two different phases and a dual phase structure can be observed. With low concentrations of lithium in magnesium, an hcp solid solution is present up to about 5.5 wt% Li. As the lithium concentration is increased, above 11.5 wt% Li, the hcp structure completely changes bcc. Between 5.5 wt% and 11.5 wt% there is a mixture of hcp and bcc (α+β) phases in the metal.

As the concentration of lithium is increased in Mg, the ductility of the alloy is increased by reason of the change of crystal structure. The bcc phase alloys

have 3 slip planes at room temperature, thus better deformation properties. In addition, lithium additions reduce the density of the metal with only a small drop in the elastic modulus [32]. However, the disadvantages of these alloys are that they tend to corrode readily at room temperature when exposed to the atmosphere and they also have low creep resistance [28]. Additionally, sodium concentration has to be controlled since it reduces the ductility.

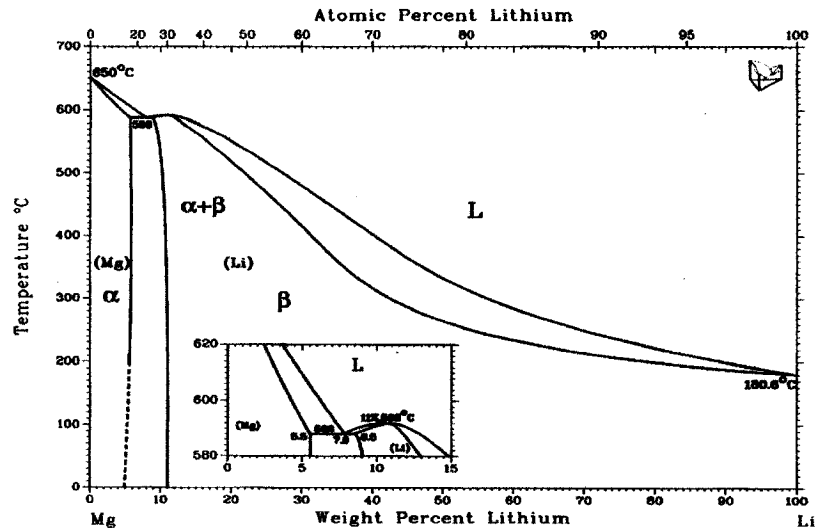

Figure 2.13: Magnesium-Lithium equilibrium phase diagram [33]

In solid solutions of Mg-Li (α - phase) it has even been found that with small additions of lithium the c/a ratio of hcp Mg reduces, consequently increasing ductility at lower temperatures [29]. Improvement of deformation upon the reduction of the c/a ratio can be attributed to the change in interplanar spacing, d, since the shear (Peierls) stress necessary to move dislocations is given by:

$$\sigma = P\exp\left(\frac{-2\pi d}{b(1-\upsilon)}\right)$$

where P is a factor that depends on the shear modulus, G, and Poisson's ratio, ν, b is the Burger's vector of the dislocation and d is the interplanar spacing. As the atomic distances are reduced through alloying there is a decrease in the

activation energy needed for the {10 $\bar{1}$0} prismatic slip [28]. As a result, there are more slip planes available for deformation at room temperature and ductility is enhanced. Hauser *et al.* also proposed that the CRSS for prismatic slip in these alloys decreased with increasing solute content and that this decrease in the CRSS was possibly a result of the decreasing c/a ratio in the hcp structure [34]. A decrease in the axial ratio of hexagonal closed packed structures can be accomplished by solid solution alloying where the solutes occupy substitutional or interstitial spaces in the crystal lattice.

2.5 Lattice Spacings of Magnesium Alloys

2.5.1 Formation of a Solid Solution

The creation of a solid solution is dependent on the solubility of the solute atom into the host atoms matrix. Solute atoms can enter into the host material either substitutionally or interstitially. Nonetheless, given that magnesium has a close-packed hexagonal structure most of the solutions formed with other elements will be substitutional. In this case, dissolution of the solute and the structure of the alloy will depend on a series of factors that were first observed by Hume-Rothery in 1934, these will be discussed in the following sections [35].

Influence of Size Factor

Atoms sizes have been seriously discussed in literature and it has been accepted that the size of an atom can never be represented by a single value [35]. Atom size can either be described as atomic, covalent, or ionic, and these are determined correspondingly by the valence electrons and by the size of the electron clouds of the ion. Considering the formation of a solid solution, it is generally assumed that the size factor is dependent on the atomic sizes of the atoms and these are found by measuring the closest distance of approach of the atoms in a crystal. In the case of magnesium the atomic diameter is found to be 3.20 Å, and it can form solid solutions with a range of elements.

It was concluded by Hume-Rothery, that the difference of the sizes between the solute and solvent atoms could never exceed 15% if an extensive solid solution is desired. Figure 2.14 illustrates the 15% difference of atomic diameters of magnesium with other elements, while Figure 2.15 shows the solubility of other elements in magnesium. It can be seen from the figures that cadmium is the only element that can form a continuous solid solution with magnesium [2][3][8]. This is attributed to the fact that cadmium has an appropriate atomic size within the 15% difference, but also to the fact that it has same crystal structure as magnesium and a similar valency. Therefore, it can be concluded that solid solution formation is not only dependent on the effect of the size factor, but on other criteria like crystal structure, valency and electronegativity.

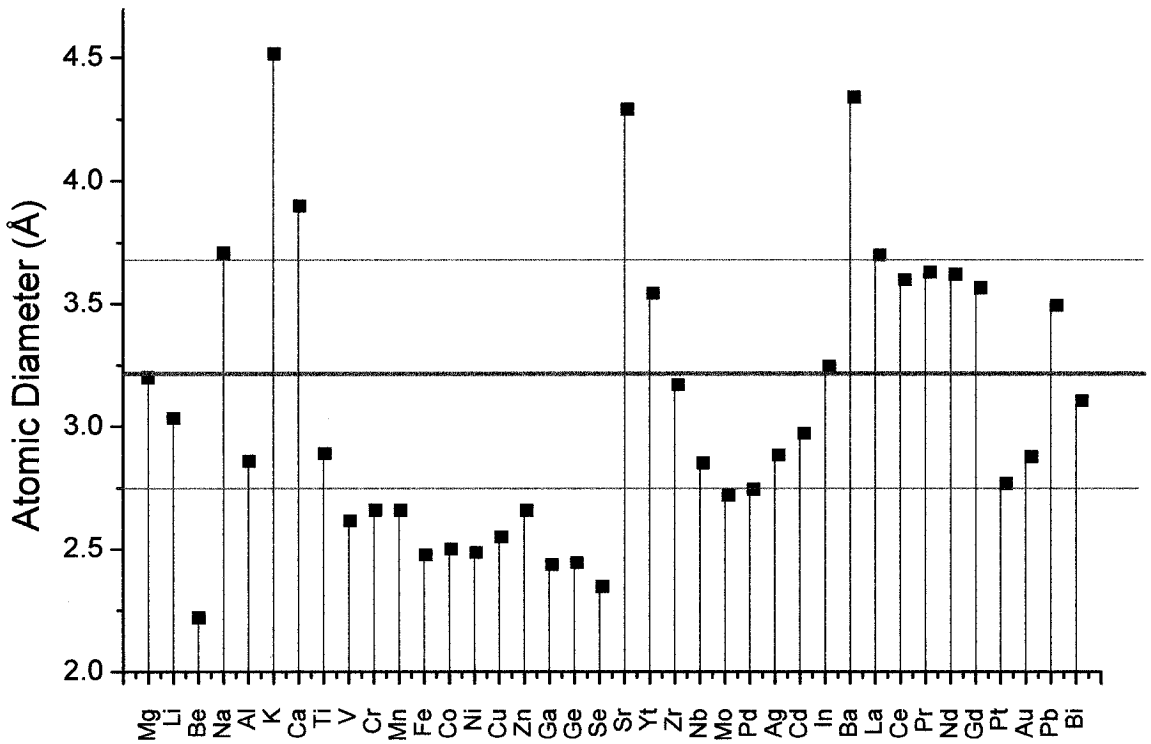

Figure 2.14: Atomic diameters of the elements, showing the 15% difference range with magnesium

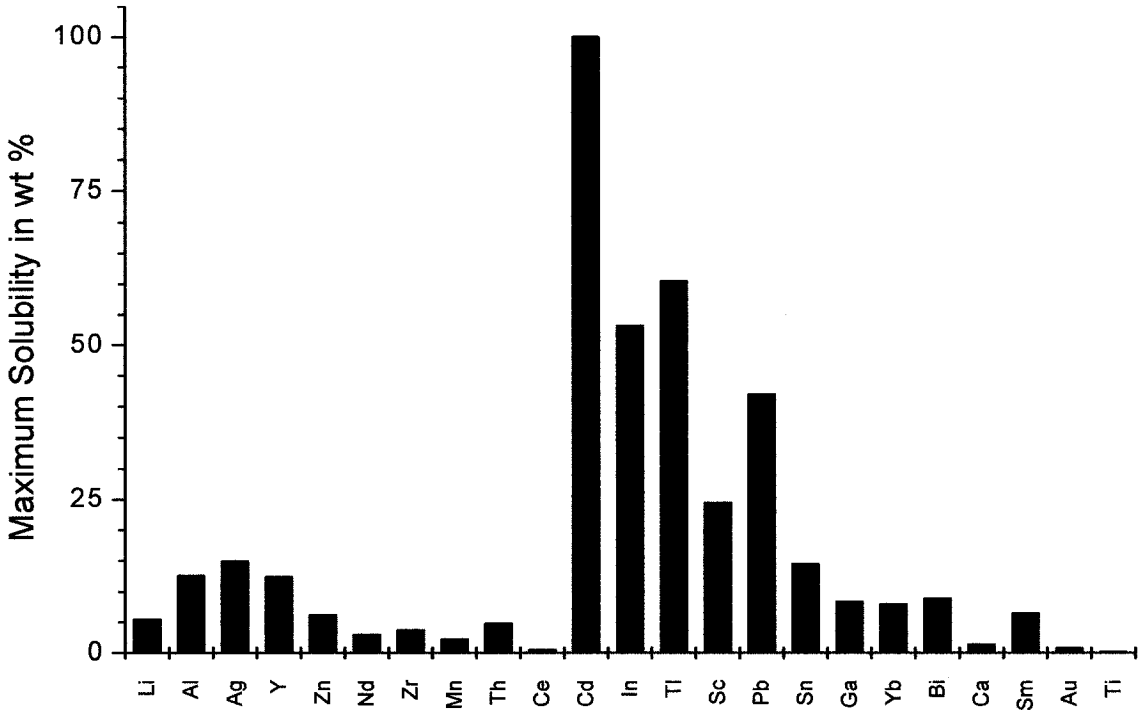

Figure 2.15: Maximum solid solubility of selected elements in magnesium

Relative Valency Effect

As concluded in the above section, dissolution of a solute into a host material is also dependent on other factors. Concerning the relative valency of an atom, it was discovered that a metal with a lower valency would tend to dissolve a solute with a higher valency rather than one with a lower valency. The concept was explained by taking into consideration that a greater number of valency electrons meant more electrons available for bond formation, hence a more stable structure [8]. Figure 2.15 shows that elements which are high valent, like indium, lead, and thallium, exhibit an extensive solid solubility with magnesium. The exception to the rule can be seen when one compares aluminum and silver solubility in magnesium. According to the relative valency effect, aluminum should dissolve more since it is 3 valent, while silver is only 1 valent. Once more, valency alone cannot be considered as the only factor to affect solid solubility.

Electronegativity

When an element with favorable size factor and relative valency still has problems dissolving into the host material; electronegativity effects are thus considered an important factor. A solute with a large difference in electronegativity with the host atom will have a tendency of forming intermetallic compounds; as a result the solubility of the solute in the host will be limited. Electropositive magnesium is inclined to form stable compounds with elements like silicon and tin, which are more electronegative [5]. In the case that neither of these factors describes the solid solubility behavior of the two elements, other factors like solute valency are taken into consideration. In this case, when the valency of a solute is increased, the extent of the primary solid solubility is decreased in a regular manner [8].

2.5.2 Changes in Lattice Spacings

As previously noted, solid solutions in magnesium are usually substitutional since the hexagonal crystal structure is close-packed and there are only few elements small enough to fit into the interstitials. In view of that, when a solute is added to magnesium, the solute will take the place of another magnesium atom and as a result affect the crystal structure. The formation of a solid solution is almost always accompanied by a lattice distortion that can be caused by the size of the solute or by its valency electrons [36]. In addition to these factors, an increase in temperature will also affect the lattice dimensions.

Vegard's Law and the Effect of Solute Size

In the development of a magnesium alloy, as soon as the solute is introduced into the matrix of the solvent metal, a substitution of atoms will take place. The solute atoms will replace some of the magnesium atoms in the crystal structure. Due to the difference in atomic size of the solute and solvent atoms, the crystal structure of solvent will become somewhat distorted and it can either expand or contract [8].

Around the 1920's, the changes in the lattice spacings of solid solutions formed between ionic compounds were related with the atomic percentage of the solute. This relationship is known as Vegard's Law, and it states that the lattice spacings of solid solutions should vary linearly in proportion to the lattice spacing of the component atoms [8]. This law was later extended to solid solutions formed between two metallic compounds. In brief, Vegard's Law can be expressed in the form of

$$d_m = nd_B + (1-n)d_A$$

where d_m is the mean interatomic distance in the solid solution composed of components A and B, with interatomic distances d_A and d_B, and n is the atomic fraction of B atoms. Nonetheless, it was later found that even if complete metallic solid solution was possible (ie Mg-Cd) there were still factors like valency differences between the components and interactions between the different types of atoms that could cause a deviation from the rule. In addition to this deviation, it was also established that to identify the size effects on the lattice distortion would be difficult since it is difficult itself to determine the true atomic diameter of the solute and solvent. However, lattice parameter changes can also be affected by the electronic structure of the solvent metal and the valence electrons of the solute atom.

Solute Valency and its Effect on Electron Concentration

In a solid solution, lattice parameter changes are also attributed to electronic concentration, which in turn depends on the valency electrons of the solute atom. This relationship can be understood in terms of the electronic structure of magnesium and its Brillouin zones. A clear representation of a Brillouin zone can be seen in Figure 2.16.

Brillouin zones are volumes that are bounded by sets of planes in k-space, (k=reciprocal space) which are equivalent to the planes of atoms in a real crystal.

These enclosed volumes are considered to have energy discontinuities at their surfaces and to contain the valence electrons of the crystal [37]. Each Brillouin zone has the same volume, but can only hold a limited amount of electrons. Therefore if an electron is located inside the first Brillouin zone then it cannot change its energy to be outside the zone unless there is an increase in energy due to an outside source. The zone theory can help explain the difference between materials that are conductors and nonconductors. In semiconductors, the energy gap between the zones is sufficiently small so that when excited, electrons can jump from one zone to the other [38]. In metals, unlike insulators, Brillouin zones overlap; as a result conduction of electrons to the second Brillouin zone is possible. It would therefore be expected that magnesium metal would have overlapping zones, which makes conduction possible.

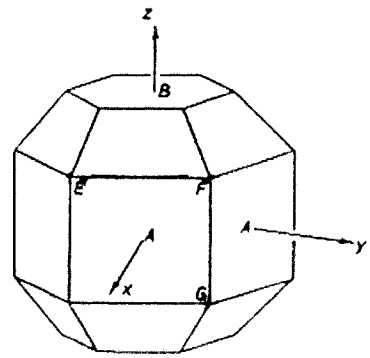

Figure 2.16: First Brillouin zone for hcp structure formed by planes {0002}, {1 $\bar{1}$ 0 0}, and {10 $\bar{1}$ 1} [8]

The first Brillouin zone for hcp metals is bounded by planes {0002}, {1 10 0}, and {10 $\bar{1}$ 1} like shown in Figure 2.16. Further study of this first zone by H. Jones, however, revealed that along certain edges like EF and FG the energy gap for electrons vanishes, and the zone looks more like the one shown in Figure 2.17 [8]. This zone is still bounded by the same three planes and it can hold up to two electrons per atom. Given that magnesium is two-valent and it is clearly a conductive metal, overlap of electrons from one zone to another is possible. Hence, if electron concentration increases, overlap of electrons from the first

zone to the second zone would be observed. The manner and sequence in which the overlap of electrons takes place is important. It can help determine the properties of magnesium and its alloys and explain the effects of electronic concentration on the lattice spacings, demonstrating the differences between magnesium and other hcp metals like Zn, Cd, which are also two valent.

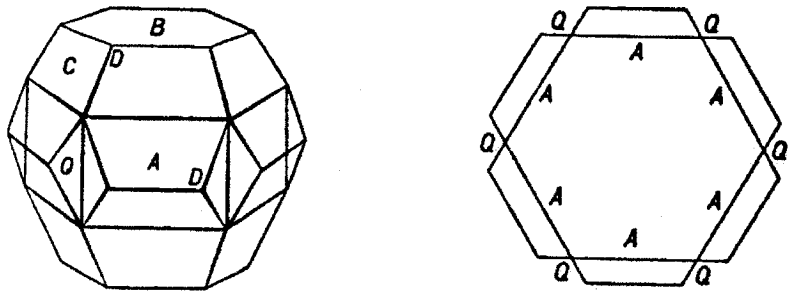

Figure 2.17: Complete and cross-section of the first Brillouin zone for hcp metals showing faces where overlap can occur [8]

Overlap of electrons in a hexagonal close-packed structure can occur either at the A faces, at the B faces or at the re-entrant Q corners. The order in which the overlap takes place is governed by the axial ratio. For instance, in hcp materials like Zn and Cd, where the c/a>1.633, the Brillouin zone is observed to be a bit more compressed along hexagonal axis. Hence the energy of the electrons at the B faces is smaller than the energy of electrons at the A faces. The opposite is true for magnesium, where the c/a< 1.633, and the overlap occurs first along the A faces. Relative energy values along the A and B faces for different hexagonal close-packed metals can be seen in Table 2.6.

Table 2.6: Relative Energy Differences Along the A and the B Faces for Different hcp Metals [8]

Element	c/a	E_A, relative energy along the A faces	E_B, relative energy along the B faces
Mg	1.624	4.88	5.55
Zn	1.861	7.13	6.17
Cd	1.890	5.67	4.77

According to the electronic structure of pure magnesium, overlap of electrons has already occurred along the A faces followed by overlap at the re-entrant corners, Q. However, with only two electrons per atom, overlap along the B faces has not taken place [8]. The N(E) curve shown in Figure 2.18 summarizes the direction and order of electron overlap in magnesium.

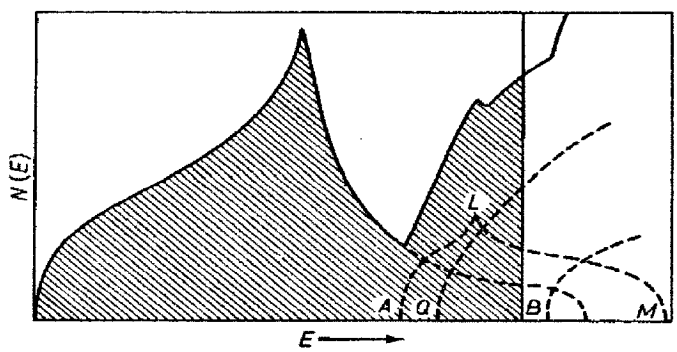

Figure 2.18: N(E) curve for magnesium, showing the A and Q overlap [8]

The changes in lattice spacing upon alloying can be clearly understood by considering the onset of overlap along the different directions. Given that pure magnesium already exhibits overlap along the A faces, an increase in electronic concentration upon alloying will also increase the number of electrons overlapping from the first Brillouin zone. For instance, when a solute of higher valency than that of magnesium is added, electron to atom ratio is expected to increase. According to Jones, when the electrons jump into the second zone, they will start producing an internal stress in the crystal, which causes a lattice distortion [8]. Electrons that overlapped along the A faces and that are outside the zone will start pushing the A faces towards the center trying to contract the first Brillouin zone. However, since this happens in reciprocal space, it is expected that the real lattice will expand along the a-spacing direction which is proportional to the A faces of the Brillouin zone. In contrast, when a solute of lower valency is added, the a-spacing will contract.

Changes in the c-spacing are however, slightly different. Given that pure magnesium does not overlap along the B faces, an overlap along this direction would only occur if enough solute is added so as to increase the electronic concentration. As the higher valent solute is added, overlap will occur first along the A faces and when a critical solute concentration is reached, overlap along the B faces take place. This will in turn expand the c-axis of the hexagonal close-packed crystal. According to Raynor, for a three valent solute like indium, overlap along the B faces occurs around a composition of 0.75 atomic% and for a four valent solute the overlap takes place around a concentration of 0.375 atomic% [8]. Recent research though, found that overlap along the B face for a three valent solute like Indium, was actually occurring at 2.3 atomic% [39]. Further investigation would have to be carried out in order to determine the real critical concentration. Figure 2.19 summarizes the effect of increasing the electron concentration on the axial value of hcp structures like Mg.

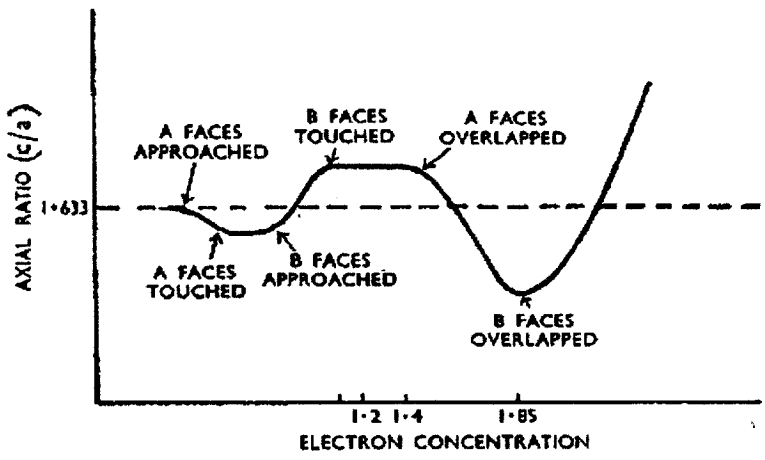

Figure 2.19: Effect of electronic concentration on axial value for hcp metals like Mg [36]

Considering that the electron concentration affects the lattice parameters of hexagonal close-packed metals, relationships between axial ratio and electron/ atom ratio have been described as follows by Busk [40].

$$c/a = 1.47298 + 0.0755\mathrm{E}' \qquad \mathrm{E}' \le 1.994$$
$$c/a = 1.62364 \qquad 1.994 \le \mathrm{E}' \le 2.005$$
$$c/a = 1.47567 + 0.0738\mathrm{E}' \qquad \mathrm{E}' \ge 2.005$$

where E' is the effective valency, which is related to electron concentration. Just as it is possible to describe the axial ratio in terms of effective valency, the a-spacing changes can also be represented by the equation:

$$a_o = a_{Mg} + (0.020014R - 0.032044)x$$

where x is the atomic% of solute and R is an empirical factor for each solute that can be found by equation:

$$R = \frac{1}{2}(a_{Mg} + 100S_a)$$

In this equation, S_a is the slope of the curve that relates the a-spacing with the concentration of the solute being considered [41]. These equations however only explain changes in lattice parameters due to electronic concentration and do not consider in any way the changes due to atom sizes. It should be noted that changes in lattice parameters are attributed to a sum of two effects: the solute size and valency of solute. In addition to changes in the lattice caused by solid solution alloying, changes in the crystal structure can also be observed upon changing the temperature.

Effect of Temperature Increase

Temperature can affect lattice changes in two ways, either by thermal expansion of the lattice or by causing electron excitation. As soon as the temperature of a metal is increased, the electrons will be thermally excited into higher energy levels and at a certain temperature it is possible that these excited electrons will overlap along the B faces of the zone [8]. Once more, this type of overlap will

cause the c-axis of the lattice to expand; as a result the c/a ratio increases. The temperature at which this overlap occurs is also dependent on the initial electron concentration in the crystal. If for example, magnesium had already been alloyed with a higher valence solute, and the temperature of the metal is increased, the onset of the B overlap will occur at a lower temperature than if it was alloyed with a solute of a lower valency.

2.6 Synopsis

Overall, lattice parameter changes in magnesium can be affected by several parameters. It would be difficult to determine which parameter has more effect than the others, but an overall effect on the c/a ratio could be observed by conducting XRD experiments at both room temperature and elevated temperatures. In general, when considering the valence electrons effect, it can be stated that when alloying with an element that has more valence electrons than magnesium, the electron/atom ratio will increase and in the long run there will be an increase in the axial ratio. In the other hand, if the alloying is done with a solute of lower valence than magnesium, the electron concentration decreases and as an effect the lattice contracts, therefore decreasing the c/a. Take in mind, that these conclusions do not take into account the size effect of the solute, which can in turn diminish or augment the effect of the electron concentration. General trends based on the studies conducted by Busk [40] and other researchers are summarized in Table 2.7.

Table 2.7: Effect of Certain Solute Elements on the a-spacing and Axial Ratio of Magnesium [8][40][41]

Effect	Elements
Decrease a-spacing	Ag, Al, Au, In, Mn, Rh, Zn, Zr
Increase a-spacing	As, Ba, Ce, La, Ni, Pd
Decrease c/a	Ag, Au, Ce, Pd, Li, Zn
Increase c/a	Al, Ba, In, Ir, Pt, Rh, Ti, Zr
No measurable effect on a or c/a	Ca, Cu, Sb, Si, Te, W

Thus, if the interest is to improve deformation characteristics of magnesium, a lower valency solute would be preferred since it would decrease the c/a ratio. As stated earlier, this decrease in the c/a ratio will change the interplanar spacing, which in turn reduces the critical resolved shear stress to activate other slip planes. If this is the case, the activation of the prismatic and pyramidal planes in magnesium could be achieved at lower temperatures. In addition to improving deformation properties, the interaction of solutes with pure magnesium could help in the development of much needed new magnesium wrought alloys. In any case, further studies have to be conducted in order to determine the effects of a combination of solute elements in magnesium. The development of new alloys requires an understanding of how well the solutes interact with each other and how they improve the properties of the solvent metal.

CHAPTER 3 - EXPERIMENTAL PROCEDURE

3.1 Raw Materials

The effect of solutes on the lattice parameters of magnesium was studied by alloying pure magnesium with four different elements. The effect of solute size was investigated by adding solutes like Ce and Zn, which have the same number of valence electrons as Mg, but which differ in atomic size. On the other hand, Li and In were added to investigate the effect of electronic concentration (e/a) since they have a valency of 1 and 3, respectively.

Magnesium based alloys were prepared from pure metals. Pure magnesium ingots (99.98%) were supplied by Timminco Metals with the main impurities being aluminum, iron, silicon, and zinc, always below 0.004 wt%. Pure cerium (99.91%) was supplied by Hefa Rare Earth Canada Co. Ltd. Pure lithium rods (99.98%), pure zinc in the form of shots (99.99%) and pure indium (99.999%) was supplied by Alfa Aesar. Cerium and lithium were received packaged under vacuum to avoid reaction with oxygen.

3.2 Alloying and Casting

Binary Alloys

A number of binary Mg-Ce, Mg-In, Mg-Li and Mg-Zn alloys were initially prepared. Pure Mg ingots were sectioned into smaller pieces using a Lenox RX M-442 blade with 4 to 6 teeth per inch. Use of the correct blade makes lubrication unnecessary, and the fine flammable magnesium powder was collected to avoid any ignition. Compositions of the alloys in atomic and weight percent can be found in Table 3.1.

Table 3.1: Binary Alloy Compositions

Alloy Target Compositions	Composition	
Mg-Ce Binaries	**At%**	**Wt %**
Mg-0.003Ce	0.003	0.018
Mg-0.01Ce	0.005	0.027
Mg-0.06Ce	0.062	0.357
Mg-0.13Ce	0.125	0.716
Mg-In Binaries	**At%**	**Wt %**
Mg-0.1In	0.108	0.509
Mg-0.2In	0.206	0.967
Mg-0.8In	0.839	3.842
Mg-2.2In	2.205	9.627
Mg-2.8In	2.817	12.045
Mg-3.3In	3.279	13.804
Mg-Li Binaries	**At%**	**Wt %**
Mg-2.3Li	2.249	0.653
Mg-6.4Li	6.405	1.917
Mg-13Li	12.638	3.967
Mg-16Li	16.216	5.238
Mg-Zn Binaries	**At%**	**Wt %**
Mg-0.2Zn	0.190	0.511
Mg-0.3Zn	0.325	0.869
Mg-0.7Zn	0.701	1.865

The alloys were prepared by melting pure magnesium and the pure elements in a mild steel crucible inside a Lindberg Blue M electrical resistance furnace set around a temperature range of 700-720 °C. The melt temperature was monitored with a chromel-alumel (type K) thermocouple. In order to avoid oxidation and burning, melt surfaces were continuously flushed with premixed CO_2 + 0.5% SF_6 protective gas at a flow rate range of 1 – 2 L/min. Lithium containing alloys were alloyed under argon to avoid the reaction of Li with the CO_2. Alloying additions were made around 680°C followed by stirring and casting in a temperature range of 720-760°C. Laboratory setup can be seen in Figure 3.1.

Mg-Ce binary alloys were prepared by first making a Mg-Ce master alloy and then diluting it. The rest of the binary alloys were prepared by adding the solid pieces into a pure magnesium melt.

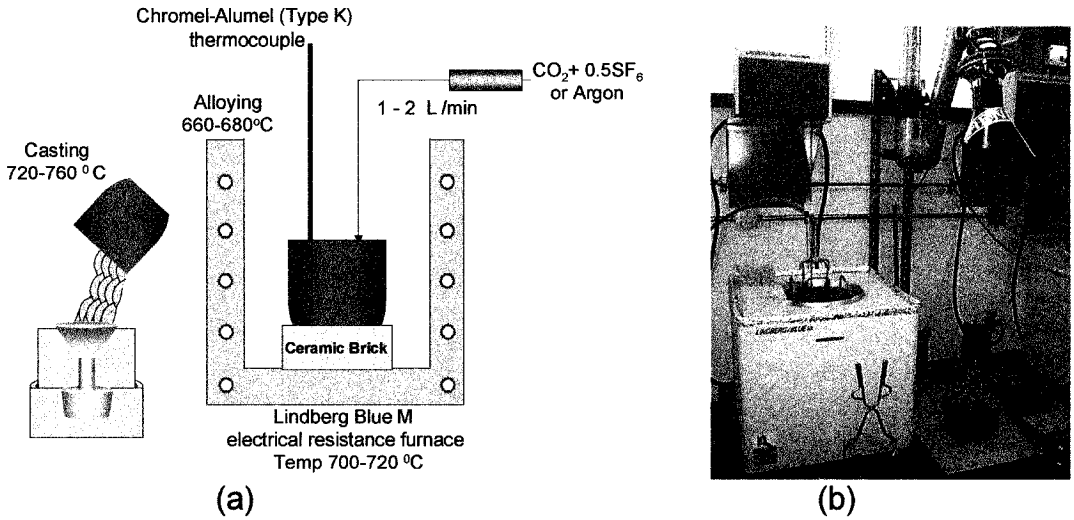

Figure 3.1: (a) Schematic representation of the experimental set-up and (b) Lindberg Blue M electrical resistance furnace.

Multicomponent Alloys

Multicomponent alloys were prepared by adding different combinations of the four chosen elements into the Mg melt. Zinc and indium additions were always made first because they stabilized the melt. Lithium, on the other hand, was added just before casting due to its reactivity and the fact that the protective atmosphere had to be changed to argon. Compositions for the multicomponent atoms can be found in Table 3.2.

Table 3.2: Compositions of Multicomponent Alloys

Alloy	Alloy Target Compositions	Composition (at%)				Composition (wt%)			
		Ce	In	Zn	Li	Ce	In	Zn	Li
1	Mg-0.3Ce-2Li	0.05			7.51	0.28			2.26
2	Mg-0.3Ce-1In	0.04	0.21			0.25	0.96		
3	Mg-0.3Ce-1Zn	0.05		0.35		0.30		0.94	
4	Mg-1In-2Li		0.23		7.77		1.13		2.33
5	Mg-1In-1Zn		0.21	0.35			0.98	0.93	
6	Mg-1Zn-2Li			0.34	6.19			0.95	1.84
7	Mg-0.3Ce-1In-1Zn	0.05	0.21	0.36		0.31	0.96	0.94	
8	Mg-0.3Ce-1In-2Li	0.05	0.19		7.40	0.29	0.96		2.21
9	Mg-0.3Ce-1Zn-2Li	0.04		0.34	7.24	0.25		0.97	2.16
10	Mg-1Zn-1In- 2Li		0.20	0.36	6.23		0.96	0.99	1.84
11	Mg-0.3Ce-1Zn-1In-2Li	0.05	0.20	0.35	7.61	0.29	0.96	0.97	2.26

Casting

The alloys were cast into two different moulds. Samples for subsequent x-ray diffraction analysis were cast into copper moulds with heated risers producing Ø40mm x 20 mm coupons. A schematic representation and a picture of the mould and the riser can be observed in Figure 3.2.

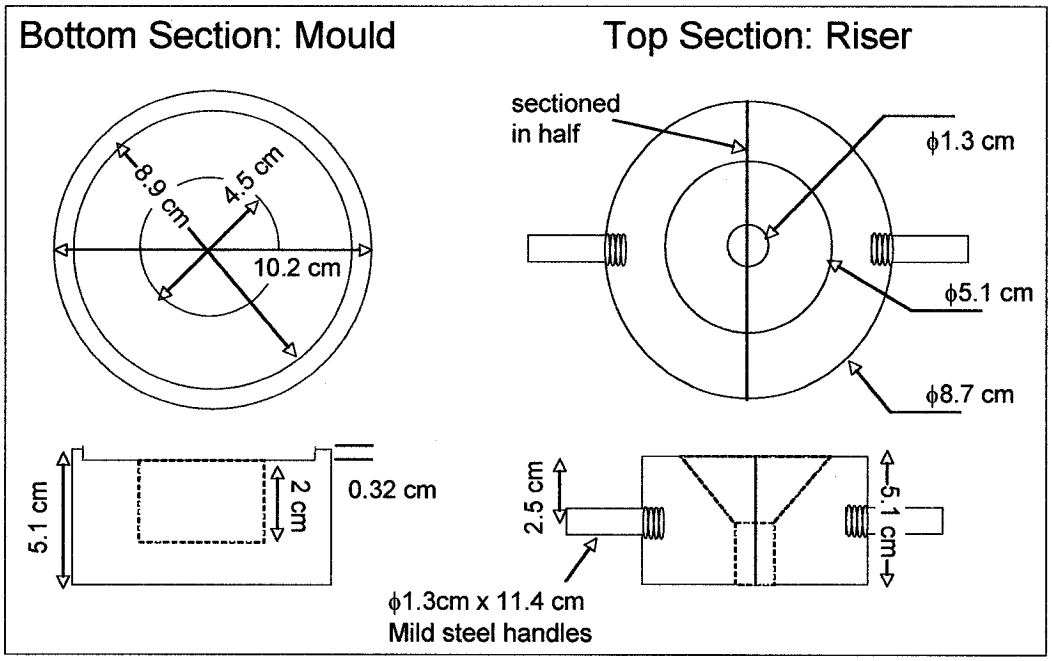

(a)

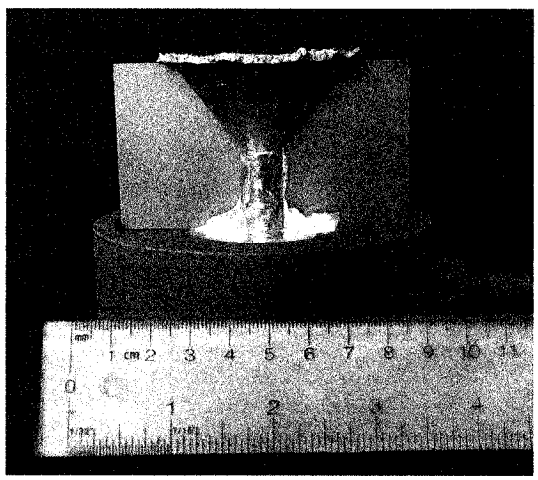

(b)

Figure 3.2: (a) Schematic of copper mould and riser with dimensions (b) photo of actual copper mould with heated riser and coupon sample

Samples to be used for deformation tests were cast into a permanent steel mould to produce 12.7 x 10.2 x 2.5 cm plates. The internal surface of the mould was sprayed with a boron nitride slurry supplied by Pyrotech. The mould was heated leaving a boron nitride coating needed in order to avoid the cast pieces from adhering to the mould. To avoid solidification during casting, the permanent mould was preheated to 425°C. A schematic representation and a picture of the permanent mould are presented in Figure 3.3.

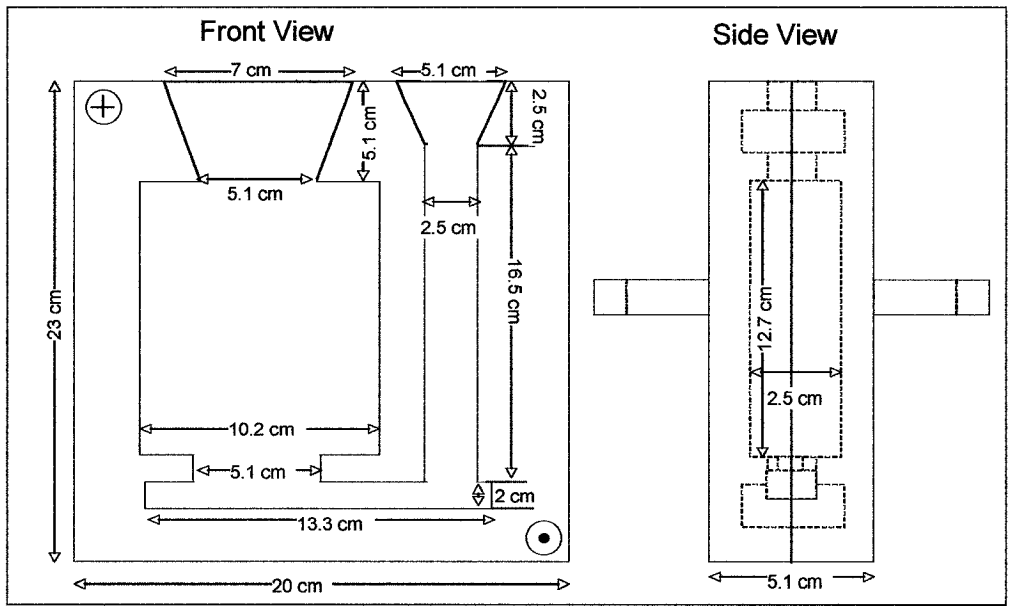

(a)

(b)

Figure 3.3: (a) Schematic of permanent steel mould showing dimensions (b) permanence mould with boron nitride coating and a cast plate.

Three alloys having a high, low and non-changing c/a with respect to pure Mg were cast with the permanent steel mould. The cast samples were used to machine compression and rolling specimens which were then used to assess the effect of lattice parameter changes on the deformation behavior of magnesium alloys. Compositions of the cast plates in atomic and weight percent can be found in Table 3.3.

Table 3.3: Compositions of Cast Plate Samples

Alloy Target Composition	Composition (at%)				Composition (wt%)			
	Al	In	Zn	Li	Al	In	Zn	Li
Mg-1Zn-2Li			0.34	6.19			0.95	1.84
Mg-1In-1Zn		0.19	0.35			0.88	0.93	
Mg-3Al-1Zn	2.43		0.34		2.68		0.89	

3.3 Heat Treatment

Cast samples were heat treated at 400°C to reduce solute micro-segregation using an inert gas electrical resistance furnace. Argon was continuously flushed inside the furnace between 10 - 20 standard cubic feet per hour (scfh) to protect the samples from oxidation. Soaking of the coupons was carried out for 8 hrs, whereas the plates were soaked for 16 hours. After homogenization, samples were quenched in cold water.

3.4 Chemical Analysis

Sample drillings were taken from the homogenized specimens. To avoid contamination, the oxide on the surface was removed with grinding paper. Drillings were then sent to Genitest Inc. where chemical analysis was performed using Inductively Coupled Plasma Atomic Emission Spectroscopy (ICP-AES).

3.5 Microstructural Investigation

3.5.1 Sample Preparation and Etching

Samples for characterization and grain size measurement were taken from the bottom portion of the coupon. In order to minimize the formation of deformation twins during the sectioning, a low speed cutter with a diamond blade and oil lubricant was used. Samples were then cold mounted in epoxy, ground from 120 to 1200 grit with SiC paper, and polished with diamond paste up to 0.25 μm. In some cases, a chemical polish was carried out by dipping the samples in a solution of 10% Nital for 30 sec.

Etching to reveal grain boundaries was carried out with a variety of chemicals. Alloys containing indium had to be etched with 5% Nital solution for a short time because a white film usually developed after prolonged exposure to the etchant. Samples containing Zn were etched with a solution of 4.2 g picric acid, 10 ml acetic acid, 10 ml distilled water, and 70 ml of ethanol (85%). Alloys with the Ce and Li, were etched with either of the solutions mentioned above.

3.5.2 Optical Microscopy and Grain Size Measurements.

Macro- and micro-structural examination of the samples was carried out using an Olympus SZ 40 stereoscope and an Epiphot 200 Nikon optical microscope. Optical images were then used to estimate the grain size with a mean linear intercept (MLI) method to average around 200 grains.

3.5.3 Scanning Electron Microscopy

The presence of second phases and their morphology was examined using a JEOL JSM 840A scanning electron microscope (SEM). An electron probe microanalyzer (EPMA) was used for elemental mapping and second phase observation.

3.6 X-ray Diffraction

Two types of XRD instruments were utilized to optimization the X-ray diffraction method: (i) Philips PW 1710 powder diffractometer and (ii) Rigaku X-ray diffractometer. Both solid and powder samples were used and compared. These helped to determine the type of sample needed for accurate lattice parameter determination.

X-ray diffraction results can be affected by a number of factors: grain size, residual stress, sample positioning, etc. Section 3.6.1 gives an overview of the optimization process with additional results found in Appendix A.

3.6.1 X-ray Diffraction Optimization

X-ray Diffraction Instruments

A pure magnesium sample was analyzed using the two x-ray diffraction instruments, mentioned above. The results obtained where then compared to a Siemens D5000 powder diffractometer with parallel beam optics in order to determine which machine was more accurate. All of the machines had a Cukα radiation source. It was observed that the pattern obtained with the Philips PW 1710 was more accurate than the one obtained with the Rigaku x-ray diffractometer, given that the pattern obtained with this machine had extra peaks. Figure 3.4 compares the three different patterns, showing the extra peaks present in the pattern obtained with the Rigaku Diffractometer.

The Phillips PW 1710 powder diffractometer was selected for this investigation given that it produced better quality data for accurate lattice parameter measurements as well as the possibility of testing both solid and powder samples.

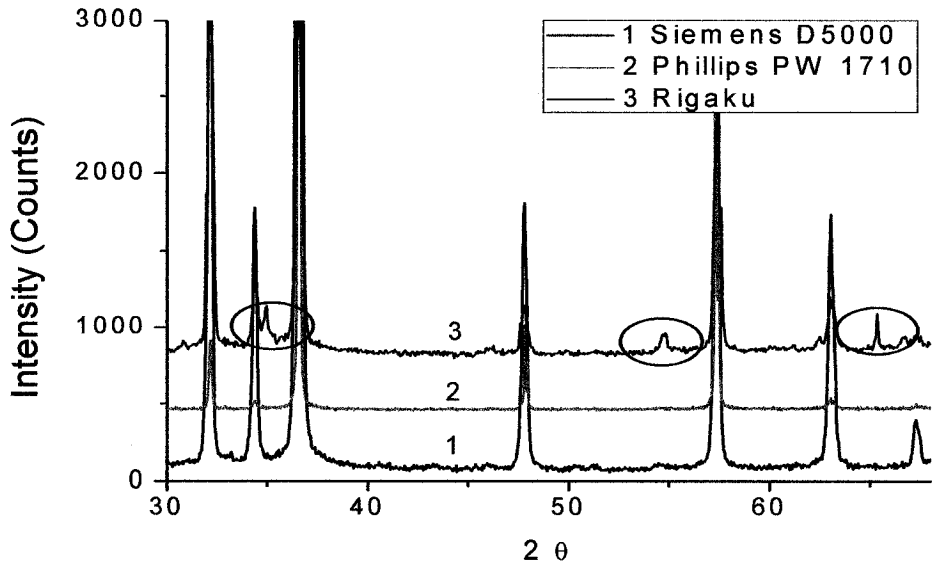

Figure 3.4: Zoomed section of the X-ray spectra obtained for a pure solid Mg sample testes with three instruments

Solid Samples

Preliminary X-ray diffraction (XRD) tests were carried out on solid samples with dimensions of 1.5 x 2 cm. Thickness was around 1 – 4 mm to minimize sample transparency error, where if the sample is too thick there will be excessive beam absorption and if it is really thin then there is an insufficient volume for diffraction [42].

Grain Size

Samples were cut from the bottom portion, which had finer grain size. Specimens with a large grain size will have preferred orientation and the x-ray beam will not cover a large area/volume relative to the size of the grains. Since only certain grains will be covered with the x-ray beam only a given number of planes will satisfy the Bragg Law. Consequently, results obtained from large grained samples are statistically less reliable.

Tests carried out on two Mg-Li samples with different grain sizes revealed that as grain size decreased from 611 μm (Figure 3.5a) to 321 μm (Figure 3.5b) preferred orientation was minimized. Nevertheless, it is also to be noted that since lattice parameters are measured using the location (2θ values) of the peaks instead of the intensity, residual stress and sample positioning are actually more important. These affect the location of the peaks and consequently the resulting lattice parameters.

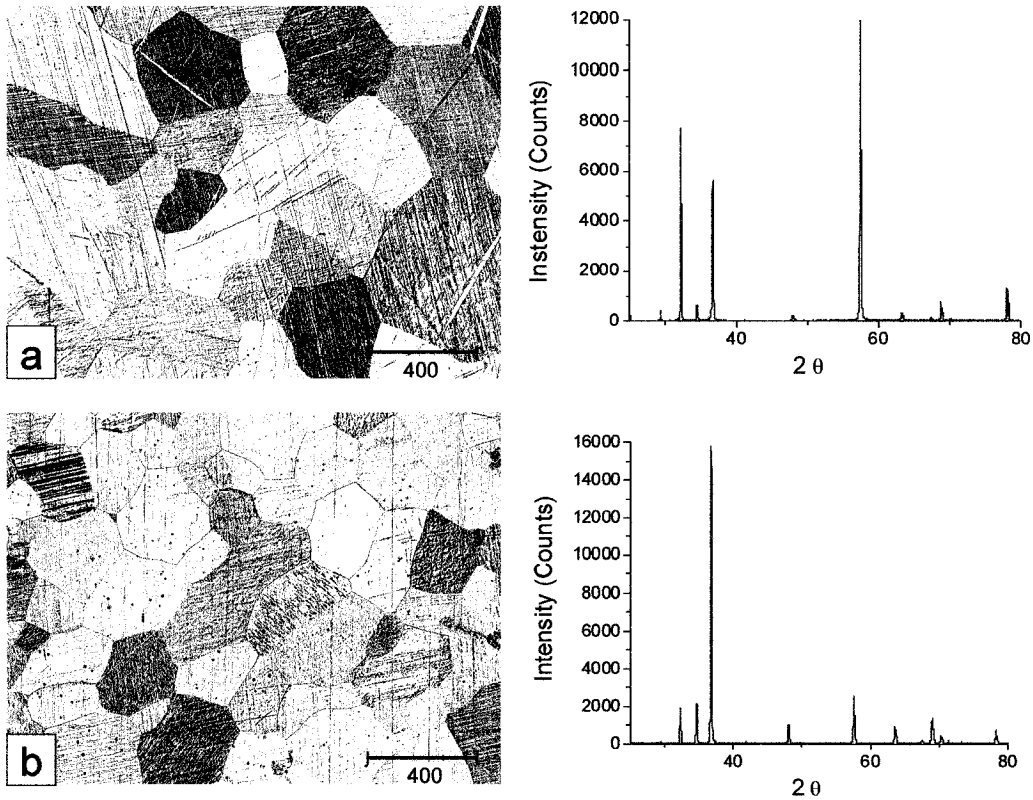

Figure 3.5: Comparison of spectra obtained for Mg-Li samples with (a) 611 μm and (b) 321 μm grain sizes

Residual Stress

Internal stress (residual stress) can cause peak broadening or peak shift in XRD analysis. If the residual stress in the sample is uniform a peak shift is observed. On the other hand, if the specimen has a non-uniform residual stress, the

resulting peak is broader with a much lower intensity [42]. Tests carried out on a pure Mg sample with two surface finishes (600 and 1200 grit) showed that there is less peak broadening when the stress is minimized (1200 grit which removes the deformed surface shell). Evidence of the effect of residual stress on the broadening of the peaks can be observed in Figure 3.6.

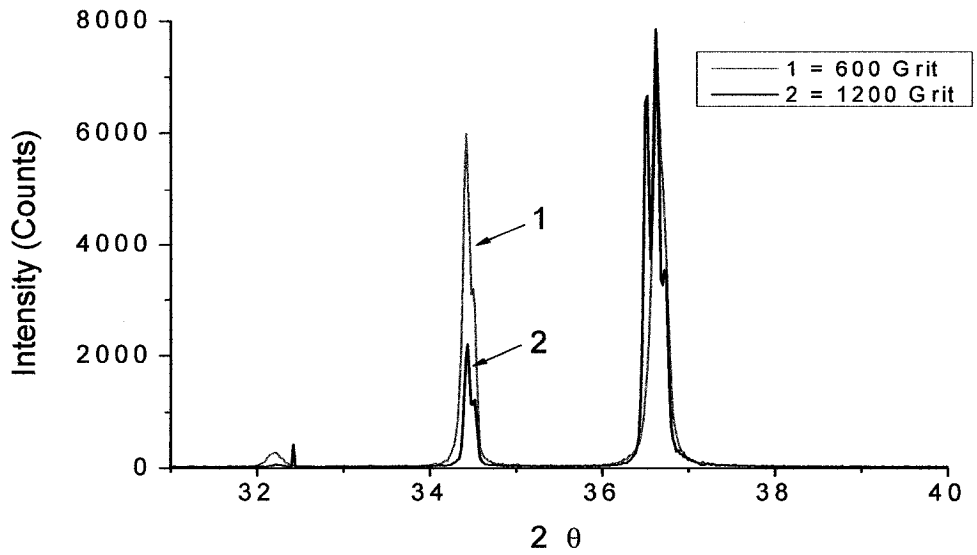

Figure 3.6: Comparison of spectra for pure Mg sample with different surface finish (black: 1200 grit finish, red: 600 grit finish)

Sample Displacement

The displacement of the specimen from the diffractometer axis is usually the largest single source error when measuring lattice parameters. The placement of the sample relative to the difractometer axis dictates the location of the peaks. Hence, if the specimen surface is not strictly perpendicular to the diffractometer axis, the Bragg angles will change and so will the location of the peaks. Consequently, lattice parameters will also change since they are calculated using the 2θ values of the peaks. To see how the sample placement affects the location of the peaks, two XRD tests were carried out on pure Mg samples. The first test was performed on a sample that was already mounted in epoxy. This made the adjustment of the sample surface with respect to the diffractometer axis difficult

and in turn changed the 2θ values of the peaks. In comparison, the other sample was simply placed inside the XRD specimen holder making it easier to level the surface of the specimen with the diffraction axis. X-ray diffraction spectra for both samples can be seen in Figure 3.7.

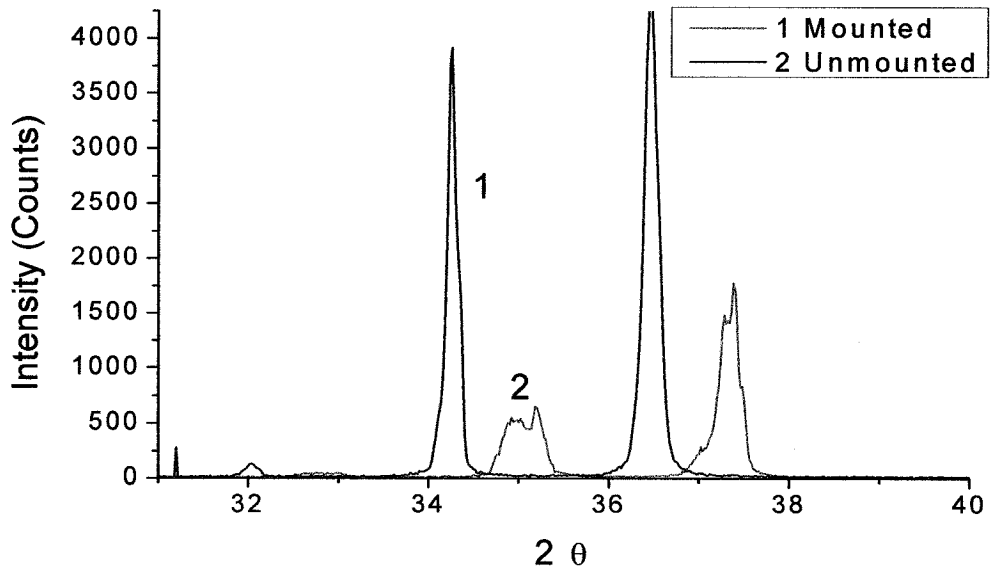

Figure 3.7: Diffraction spectra for mounted and unmounted pure Mg samples showing the peak shift due to sample positioning

The 2θ values for the peaks observed in Figure 3.7 are listed in Table 3.4. The experimental values for both samples were compared to the pure Mg standard values found in literature [43]. From the difference it was observed that the sample which was not mounted in the epoxy, but which was mounted on the XRD holder had 2θ values closer to the standard.

Table 3.4: Peak 2θ Values for Mounted and Unmounted Pure Mg Samples.

Peak HKL	Mg Standard 2θ values [43]	Mg Mounted 2θ values	Difference * Mounted	Mg Unmounted 2θ values	Difference* Unmounted
100	32.17 °	32.79 °	0.62	32.08 °	0.09
002	34.39 °	35.10 °	0.72	34.26 °	0.13
101	36.60 °	37.38 °	0.78	36.45 °	0.14

* Difference between experimental result and Mg standard

Powder Samples

From preliminary tests carried out on solid samples it was determined that powder samples could be an alternative. Powder samples would minimize preferred orientation and when annealed would also minimize residual stress. Furthermore, powders can be mixed with a standard like pure Si in order to correct the sample displacement error.

Preliminary XRD tests on pure Mg powder were conducted to determine differences in the results obtained with a coarse (65 mesh) and a fine (150 mesh) powder. Lattice parameters were calculated with the spectra obtained from the coarse and fine powder samples. These were then compared to the lattice parameters obtained with the solid pure Mg sample and the Mg standard. Table 3.5 lists the lattice parameters obtained with each of these samples

Table 3.5: Lattice Parameters for Pure Mg Solid and Powder Samples.

Samples	a-spacing (Å)	c-spacing (Å)	Axial Ratio (c/a)	% Diff +
Solid	3.2089	5.2036	1.6216	0.200
Coarse	3.2035	5.2056	1.6250	0.130
Fine	3.2086	5.2109	1.6240	0.040

+ Percent difference with c/a ratio for pure Mg standard (1.6237)

From the results obtained it was determined that fine powder samples would be the best type of samples for accurate lattice parameter measurements. Fine powders would be more random than the coarse powder and they would also be easier to anneal.

3.6.2 X-ray Diffraction Analysis

After the optimization exercise, the XRD technique adopted comprised the use of the Phillips PW 1710 powder diffractometer with annealed fine powder samples. Sample preparation and XRD techniques used in the project are explained below.

Sample Preparation

Fine powder samples for X-ray diffraction were prepared by filing the alloy coupons with a steel blade. Before filing, the coupon surface was cleaned with grinding paper and then sectioned. Filings were taken from various sections with the intention of preparing a representative sample. Filing was carried out inside a glove bag with argon and also without a glove bag. XRD tests performed on samples filed outside of the glove bag did not show any oxide presence. Therefore, filing was carried out without the use of a glove bag given that it would be easier to manipulate the solid pieces and produce a greater quantity of powder. A picture of the glove bag can be seen in Figure 3.8.

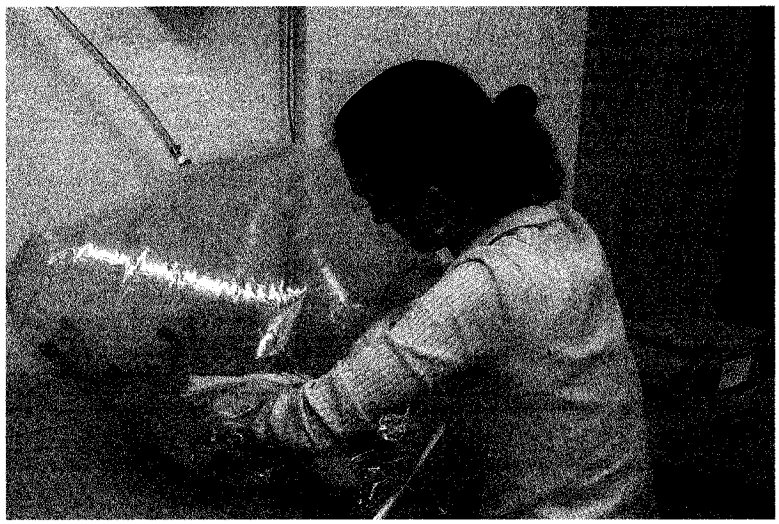

Figure 3.8: Preparation of Mg powder inside a globe bag with argon

In order to reduce any residual stress that has been introduced during filing, the filings were encapsulated in a quartz tube, sealed under argon, annealed for 16 hours at 275°C, and then rapidly cooled in air. Alloy filings were subsequently mixed with pure Si and mounted onto a microscope slide using petroleum jelly as the binder. Pictures of the encapsulated powder and the powder XRD samples can be found in Figure 3.9.

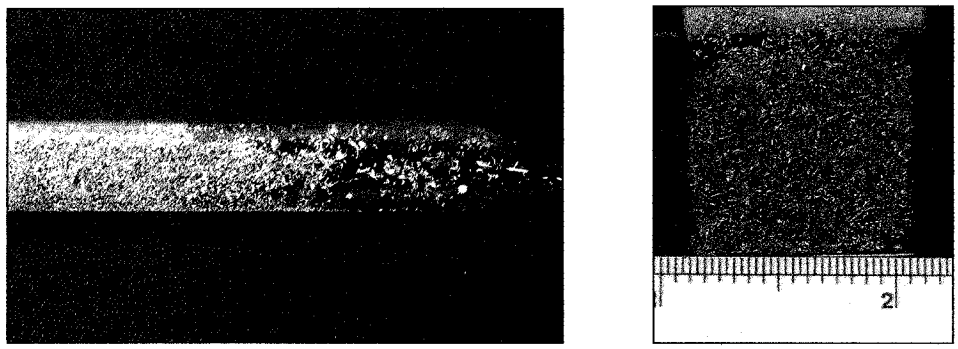

(a) (b)

Figure 3.9: (a) Encapsulated powder for annealing and (b) fine powder mounted on a microscope slide.

XRD analysis

X-ray diffraction tests were carried out using a Philips PW 1710 powder diffractometer with Cu-α radiation (Kα1 = 1.540598 Å, Kα2= 1.544426 Å). Specimens were placed inside the x-ray diffraction chamber carefully keeping the microscopes slides perpendicular to the diffraction axis so as to avoid displacement of the resulting peaks. Pictures of the diffractometer and the sample inside the x-ray diffraction chamber can be seen in Figure 3.10.

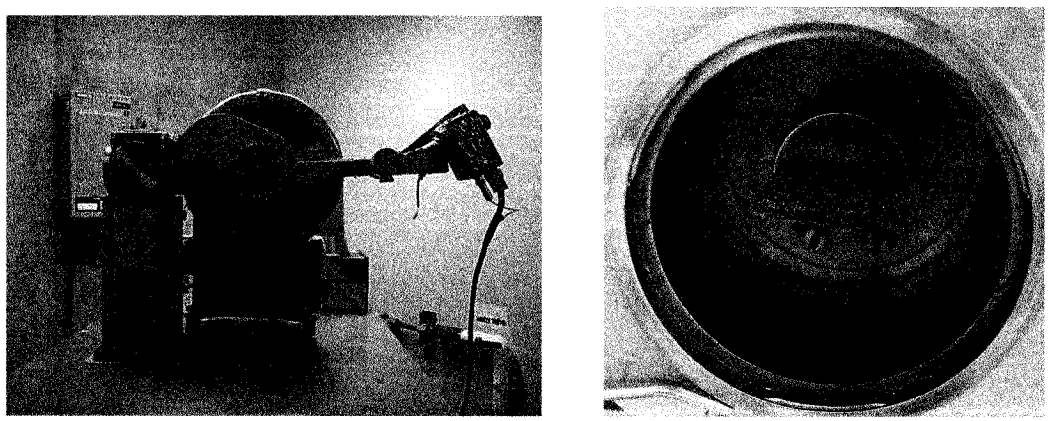

(a) (b)

Figure 3.10: (a) Philips PW 1710 powder diffractometer and (b) powder sample inside x-ray diffraction chamber.

X-ray diffraction tests were run using an accelerating voltage of 40 kV, a beam current of 20 mA, and a scan rate of 0.025 °/ s. Samples were scanned over a 2θ range of 25 to 120 degrees. Four x-ray measurements were made for each alloy to determine. As a control, x-ray measurements were also carried out on pure Mg samples in order to acquire experimental lattice parameters.

Lattice Parameter Measurements

XRD data obtained was refined and analyzed using the GSAS™ software. This software uses the Rietveld method where the experimental x-ray pattern is modeled using least squares approximation and existing crystallographic data [44]. The method comprises several parameters that should be refined, some of which include: lattice parameters, background, atom positions, thermal movement, etc.

Sample displacement was corrected by aligning the peaks of pure Si in all of the samples. This was accomplished by keeping the unit cell parameters of Si constant, whereas the Mg unit cell was continuously being refined in order to fit the experimental results. To improve the fit of the theoretical results with respect to the experimental results, the spectra were refined starting at a 2θ angle of 45°. Since the first three low angle peaks of Mg are highly asymmetrical they tend to upset the fit for the spectra causing the measurements to be less accurate. Hence, precise lattice parameters measurements are usually carried out with the higher angle peaks in order to reduce the error of the sine function found in the following equation:

$$\sin^2\theta = \frac{\lambda^2}{4}\left[\frac{4}{3}\frac{h^2+hk+k^2}{a^2}+\frac{l^2}{c^2}\right]$$

This equation is a combination of the Bragg Law and the plane-spacing equation and it was used to calculate both the a and the c parameters.

3.7 Formability Assessment

3.7.1 Sample Preparation

Rolling

Rolling samples were prepared from the homogenized thick plates produced in the lab (Table 3.3). Specimens having 6 x 25 x 25 mm dimensions were machined from the block as shown in Figure 3.11. After sectioning, the samples were ground to 1200 grit in order to clean the surfaces before rolling.

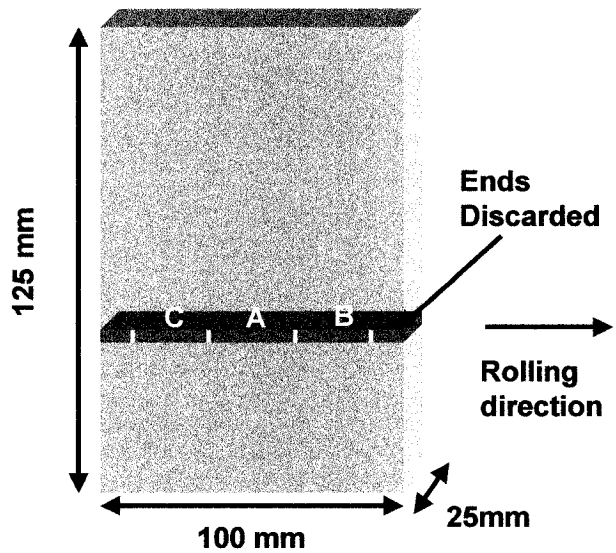

Figure 3.11: Schematic representation of the thick plat showing the location and dimensions of the rolling specimens

Compression

Compression samples measuring Ø 8 mm x 12 mm were machined from the bottom edge portion of the block illustrated in Figure 3.11. Specimen geometry was selected where the height/radius ratio was kept at 1.5 so as to avoid sample buckling [45].

3.7.2 Rolling Tests

Alloy specimens were rolled at 150°C using a Stanat rolling machine with cold rolls and an oil lubricant (Figure 3.12a). Samples were placed inside a Lindberg Blue-M electrical resistance furnace where they were pre-heated for 15 minutes prior to rolling. Specimens were re-heated for 5 minutes after every pass due to the loss of heat from the cold rolls making rolling difficult. Specimen A as indicated from Figure 3.11 was rolled in 15 passes to an engineering strain of 0.55. Sample B was rolled in 7 passes up to an engineering strain of 0.3. Rolling of the samples was always carried out in the same direction and quenched in cold water after the final pass. Figure 3.12 shows pictures of the rolling equipment and a rolled pure magnesium sample.

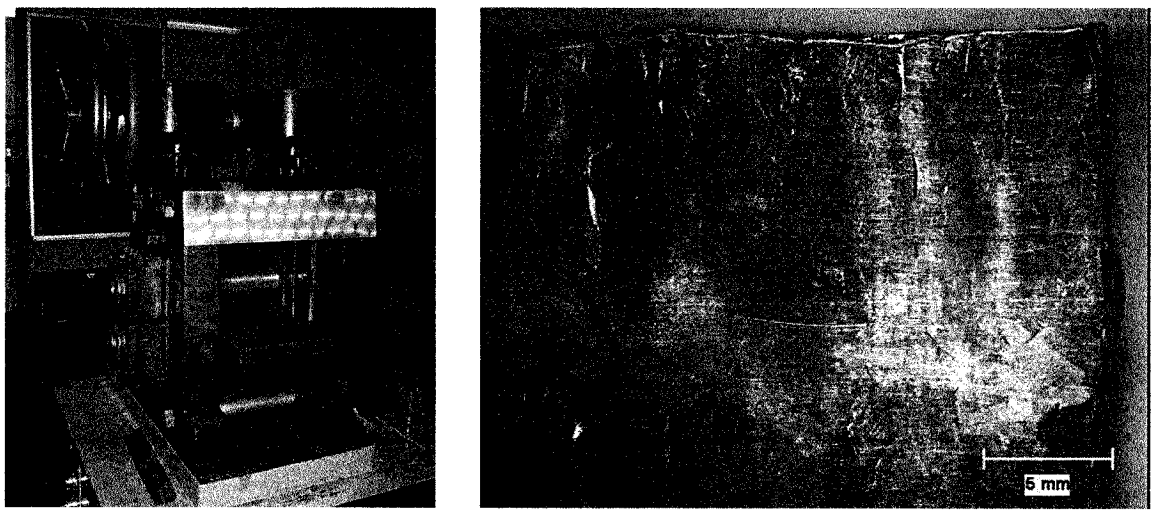

(a) (b)

Figure 3.12: (a) Stanat rolling machine and (b) magnesium sheet

3.7.3 Compression Tests

Alloy specimens were compressed at true strain rate of 10^{-3} s^{-1} at room temperature (RT) and at 150°C using a Model 510 MTS machine. Specimens were compressed to failure and to a true strain of 0.2 at both temperatures. For elevated temperature testing, samples were heated at a rate of 50°C/min to a test

temperature of 150°C, soaked for 10 min to achieve temperature homogeneity, compressed to failure or a strain of 0.2, and then quenched in water. To reduce friction, specimens were coated with boron nitride and a mica sheet was placed between the specimen and the compression anvil. Temperature was constantly monitored with a K-type thermocouple, which was placed in contact with the sample inside the furnace. To minimize oxidation, the sample was compressed in a sealed quartz chamber under a protective argon atmosphere. Three samples were compressed for each alloy in order to observe the repeatability of the results. A schematic diagram of the compression setup is shown in Figure 3.13.

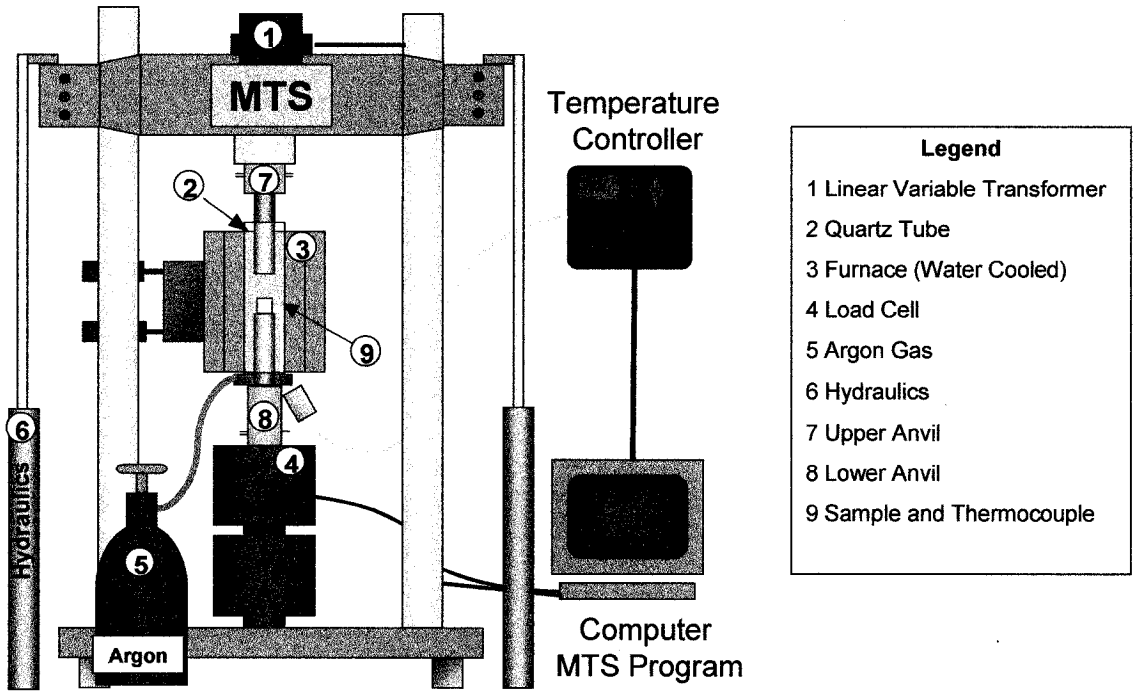

Figure 3.13: Schematic compression of the Model 510 MTS machine.

CHAPTER 4 - RESULTS

The results have been divided into two main sections: Lattice Parameter Measurements and Formability Assessment. It is important to mention that grain sizes and lattice parameter results refer to samples taken from homogenized coupons. While, rolling and compression tests were carried out on samples machined from the thick block.

4.1 Lattice Parameter Measurements

Hume Rothery, G.V Raynor and R. S. Busk are by far the most important contributors to the subject of magnesium lattice parameters [35][40][41]. Their investigations focused on measuring the lattice parameters for several magnesium binary solid solutions and they found that both solute size and solute valency affect the lattice spacings causing either an expansion or contraction of the unit cell. Temperature and stress were also identified as producing a change on the dimensions of the unit cell; however their effect was not investigated in the present project.

Four different solutes were investigated, two of which differ in atomic size and the other two differ in number of valence electrons with respect to magnesium. In order to understand the effect of each solute on the pure Mg crystal structure, each binary system was studied individually. Lattice parameters for alloys made with combination of the four chosen solutes was also investigated.

4.1.1 Pure Magnesium

The microstructure of the cast pure magnesium coupons was found to contain both columnar and equiaxed grains as can be observed in Figure 4.1.

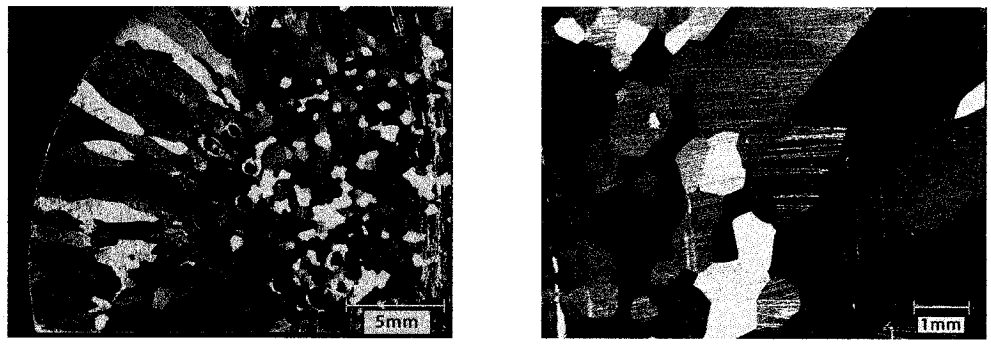

Figure 4.1: Macrographs for pure Mg showing both columnar and equiaxed grain structure.

Grain sizes for both columnar and equiaxed grains were found to be 5.3 mm and 647 ± 65 μm, respectively. Columnar grains were measured using the length of the column instead of the thickness.

In order to generate lattice parameters to be used as a control for the other alloys, x-ray diffraction tests were carried out on pure Mg powder filed from the coupons. Representative XRD spectra for pure Mg can be found in Figure 4.2.

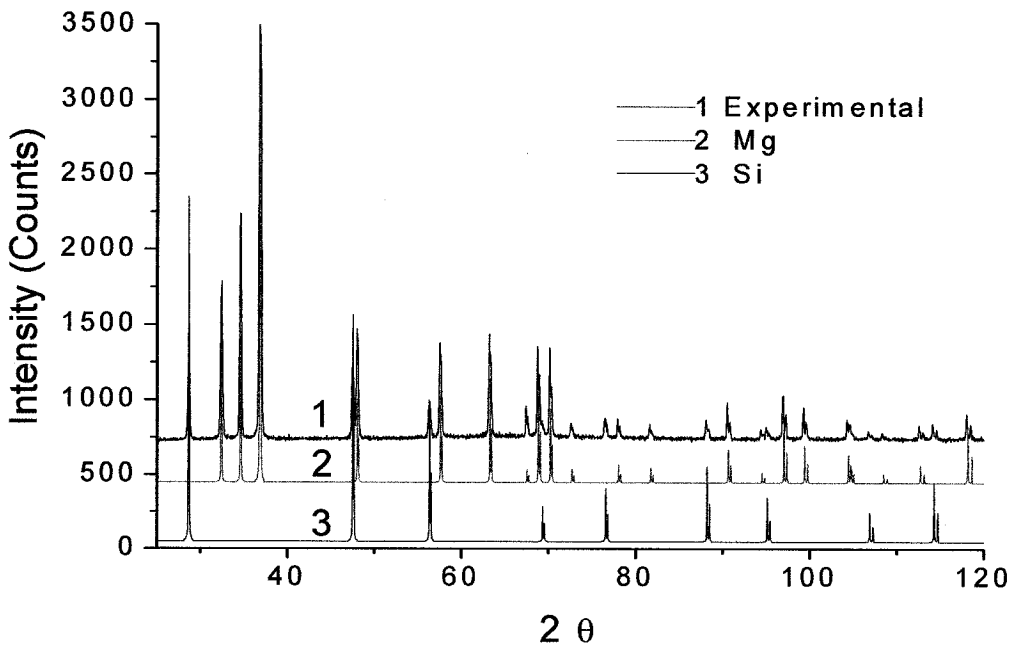

Figure 4.2: X-ray diffraction spectra for pure magnesium.

All of the diffraction patterns obtained were found to contain only the peaks for metallic Mg with no detectable presence of oxidation products possibly created during the production of the powder. Lattice parameters, c/a ratio, and volume of the unit cell for three different pure Mg annealed powder samples are listed in Table 4.1.

Table 4.1: Volume and Lattice Parameters of the Pure Mg Unit Cell

Test	a-spacing (Å)	c-spacing (Å)	c/a ratio	Volume of Cell ($Å^3$)
1	3.2086	5.2111	1.6241	46.46
2	3.2088	5.2107	1.6239	46.46
3	3.2089	5.2116	1.6241	46.48
Average	**3.2088**	**5.2111**	**1.6240**	**46.47**
StDev	**0.0002**	**0.0004**	**0.0001**	**0.01**

Three different lattice parameters measurements obtained for commercially pure Mg determined the a-spacing and c-spacing to be 3.2088 Å and 5.2111 Å, respectively. The three XRD tests were necessary in order to account for the systematic errors of the machine and confirm the repeatability of the results.

The observed results were found to be somewhat different from the previously published values found in Table 4.2. Given that early research was carried out in the mid 20^{th} century, the purity of magnesium metal was fairly lower and the resulting lattice parameters were affected by any present impurities. Additionally, x-ray diffraction and analysis techniques have also improved throughout the years making analysis easier with the use of computer software.

Table 4.2: Published Lattice Parameters for Pure Mg.

a-spacing (Å)	c-spacing (Å)	axial ratio (c/a)	Year	REF
3.2025	5.1999	1.6237	1940	41
3.2023	5.1994	1.6236	1950	40
3.2095	5.2107	1.6235	1957	39
3.2088	5.2111	1.6240	2006	THIS STUDY

It was observed that the most recent study [39] gave lattice parameters that were closer to the ones obtained in this study, which will be used as a control when discussing the lattice parameters of the other magnesium alloys

Using the calculated lattice parameters, interplanar spacings (d) for the slip planes found in hexagonal close-packed crystal structures were determined. However, only the d-spacing values for the {0002} basal, $\{10\bar{1}0\}$ prismatic, and $\{11\bar{2}2\}$ pyramidal slip planes were monitored, given that the activation of the slip systems containing these planes will potentially improve formability of Mg. Inteplanar spacings for the basal, prismatic, and pyramidal planes of pure Mg are recorded in Table 4.3.

Table 4.3: Interplanar Spacings for {0002}, $\{10\bar{1}0\}$ *and* $\{11\bar{2}2\}$ *Slip Planes*

Plane (HKiL)	Interplanar Spacing (Å)
{0002}	2.6056
$\{10\bar{1}0\}$	2.4520
$\{11\bar{2}1\}$	1.3662

4.1.2 Binary Solid Solutions

The lattice parameters and microstructures of binary alloys of magnesium with Li, In, Ce, or Zn are presented below. It was determined that both the solute size and the valency of the solute affected the dimensions of the unit cell.

Explaining lattice parameter changes due to the effect of atom size difference is a difficult task in view of the fact that atom sizes are dependent on the type of bonding found in the alloy (either metallic or covalent). For the purpose of this investigation, the atomic sizes chosen for the analysis were those proposed by Teatum and his co-workers, where the atomic sizes are based on the interactomic distances in metals (metallic bond) [46]. Atom size, atomic size

difference with respect to Mg, and number of valence electrons, for the solutes can be found in Table 4.4.

Table 4.4: Atom Size, Atomic Size Difference, and Valency of the Solutes.

Element	A.S * (Å)	A.S Difference**	Valency
Mg	1.62	0	2
Ce	1.72	0.07	2 or more
In	1.66	0.04	3
Li	1.56	-0.03	1
Zn	1.39	-0.13	2

*A.S: Atomic Sizes

** A.S Difference : $\frac{A.S._{sol} - A.S._{Mg}}{A.S._{Mg}}$

Of the investigated elements, Zn and Ce have the largest atomic size difference with respect to Mg as can be seen in Table 4.4. Yet, given that Ce could have a number of valence electrons of 2 or more; Zn would be the only solute where the lattice parameter changes would be exclusively associated with an atomic size difference. Alternatively, solutes such as In and Li show a small size difference with respect to Mg, but most importantly they contain a different number of valence electrons than Mg. Consequently, both of these solutes have the potential of changing the electronic concentration of the Mg unit cell, therefore causing Brillouin zone overlap, which in turn causes lattice parameter changes.

Mg-Li System

Changes to the lattice parameters as well as the microstructure of pure Mg were observed upon the addition of four Li concentrations. The compositions of the four Mg-Li alloys can be found in Table 3.1. Sample images of the alloys can be observed in Figure 4.3 - Figure 4.6.

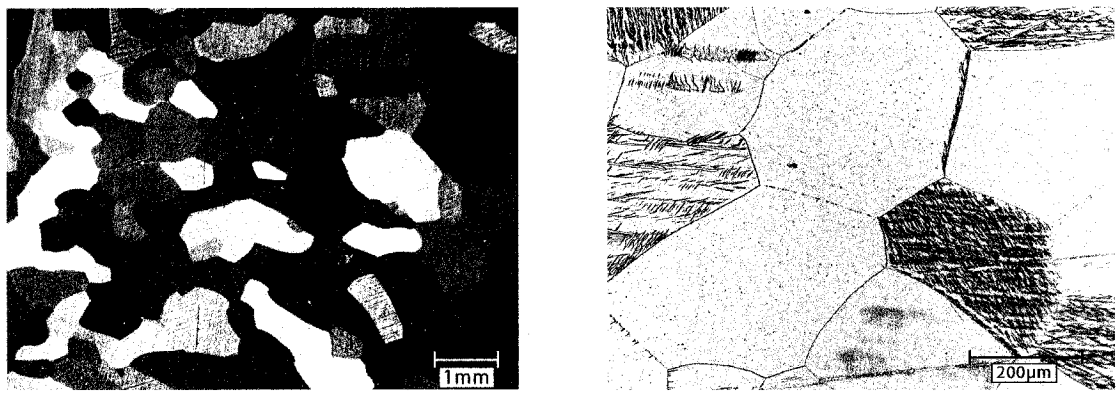

(a) (b)

Figure 4.3: Mg-2.3Li alloy sample images taken at (a) lower magnification and (b) intermediate magnification. Grain Size = 251 ± 23 µm.

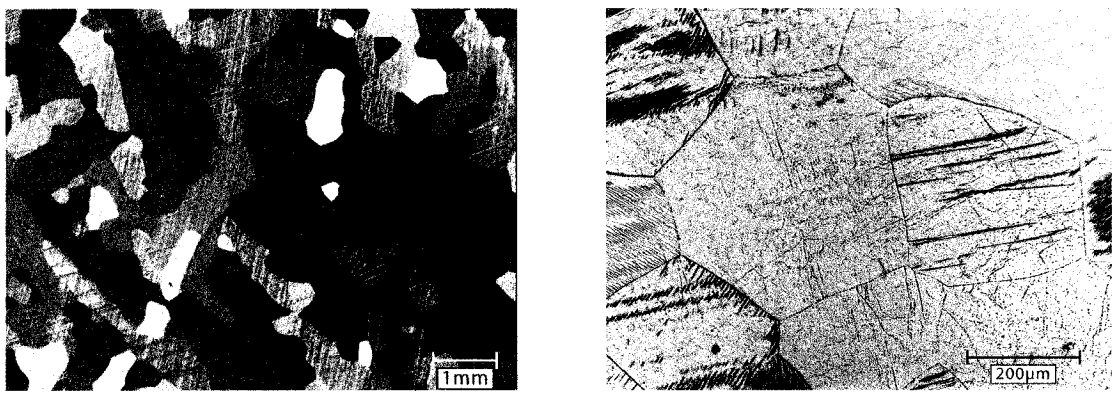

(a) (b)

Figure 4.4: Mg-6.4Li alloy sample images taken at (a) lower magnification and (b) intermediate magnification. Grain Size = 225 ± 23 µm.

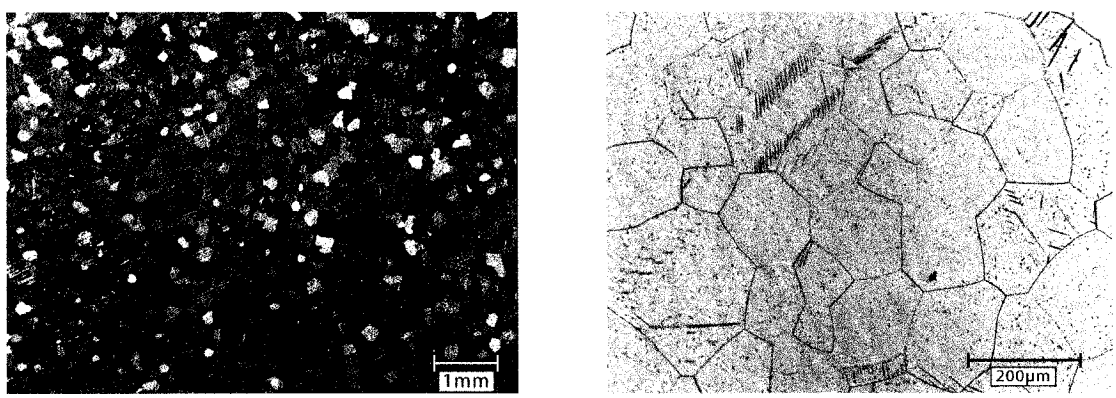

(a) (b)

Figure 4.5: Mg-13Li alloy sample images taken at (a) lower magnification and (b) intermediate magnification. Grain Size = 156 ± 7 µm.

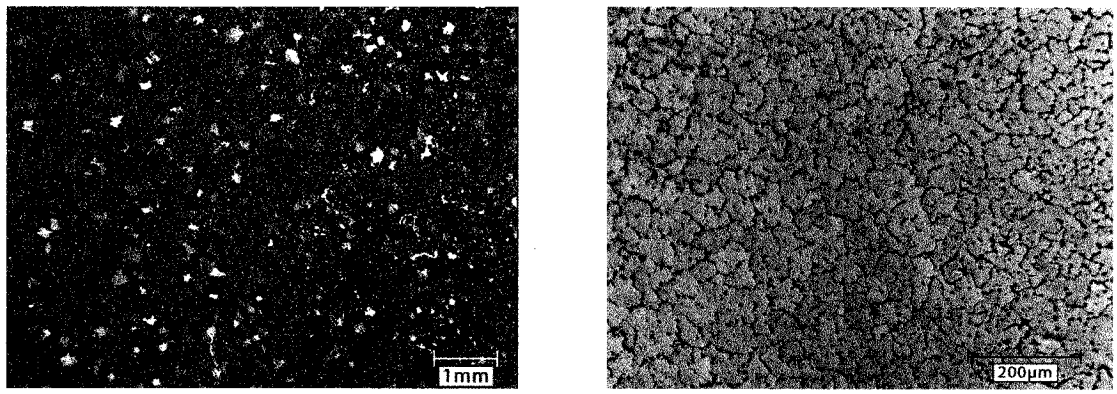

(a) (b)

Figure 4.6: Mg-16Li alloy sample images taken at (a) lower magnification and (b) intermediate magnification. Grain Size < 100 µm.

Microstructural examination revealed that grain sizes reduced from 251 µm to less than 100 µm with increasing solute concentration Second phases were also present in the alloy with higher Li content (Figure 4.6b).

X-ray diffraction spectra obtained for the four Mg-Li binary alloys were compared to observe the shift of the peaks with increasing Li concentration, these can be seen in Figure 4.7.

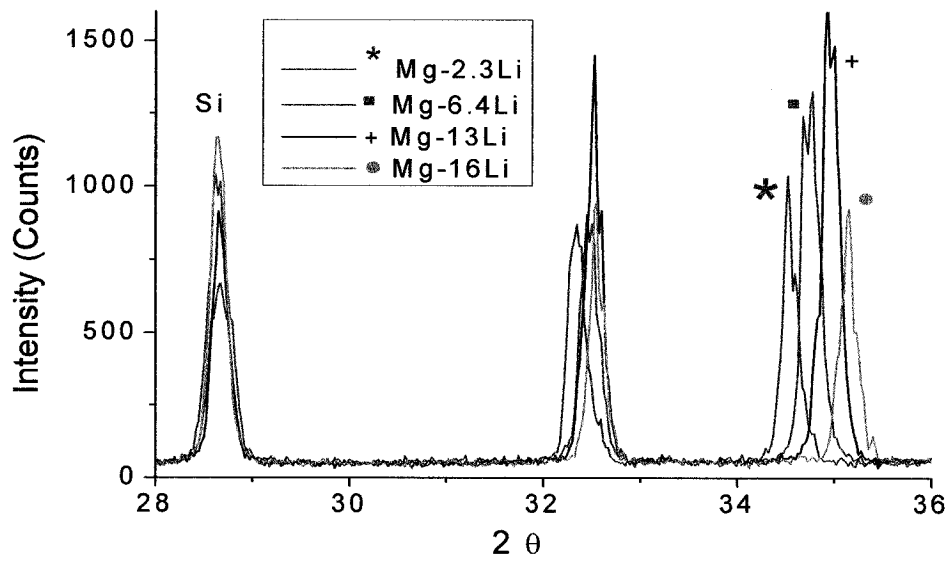

Figure 4.7: X-ray diffraction results for Mg-Li binary alloys showing shift of the Mg solid solution peaks.

Once sample displacement error was corrected by aligning the pure Si peaks of all the spectra, the Mg solid solution peaks appear to be shifting to the right with increasing Li concentration. The change in peak location is therefore related to a change in lattice parameters.

Table 4.5 summarizes the results obtained from the Mg-Li alloy spectra and compares them with results obtained for pure Mg. Standard deviations were found using the results of three tests and they were always below 0.0006 for the a- and c-spacings, 0.0002 for the c/a, and 0.02 for the volume of the unit cell.

Table 4.5: Results Obtained from XRD Data of Mg-Li Alloys

Alloy Target Compositions	At % Li	Wt% Li	e/a	a-spacing (Å)	c-spacing (Å)	c/a	Volume ($Å^3$)
Mg	0.00	0.00	2.000	3.2088	5.2111	1.6240	46.47
Mg - 2.3Li	2.25	0.65	1.978	3.2076	5.2051	1.6227	46.38
Mg - 6.4Li	6.41	1.92	1.936	3.2034	5.1895	1.6200	46.12
Mg - 13Li	12.64	3.97	1.874	3.1964	5.1556	1.6129	45.62
Mg - 16Li	16.22	5.24	1.838	3.1930	5.1305	1.6068	45.30

Lithium being a one-valent solute with a smaller atomic size than Mg was observed to decrease the electronic concentration of the Mg unit cell. Consequently, a contraction of both lattice parameters occurred as can be seen from Figure 4.8. However, the observed reduction for the c-spacing was quite more dramatic than the reduction observed for the a-spacing and as a consequence the axial ratio reduced from 1.6240 to 1.6068 (Figure 4.9a).

Given that the contraction of the c-spacing was greater than the contraction of the a-spacing, it is believed that dimensions of the c-spacing are affected by a decrease in electronic concentration as well as a solute size difference between the Li and Mg solutes. Conversely, changes to the a-spacing were not as sensitive to the electronic concentration modification and the observed decrease was probably mostly caused by an atomic size difference. These results support that changes of the axial ratio depend mainly on changes made to the electronic

concentration of the unit cell. Changes to the volume of the unit cell follow the same trend as those observed for the axial ratio (Figure 4.9).

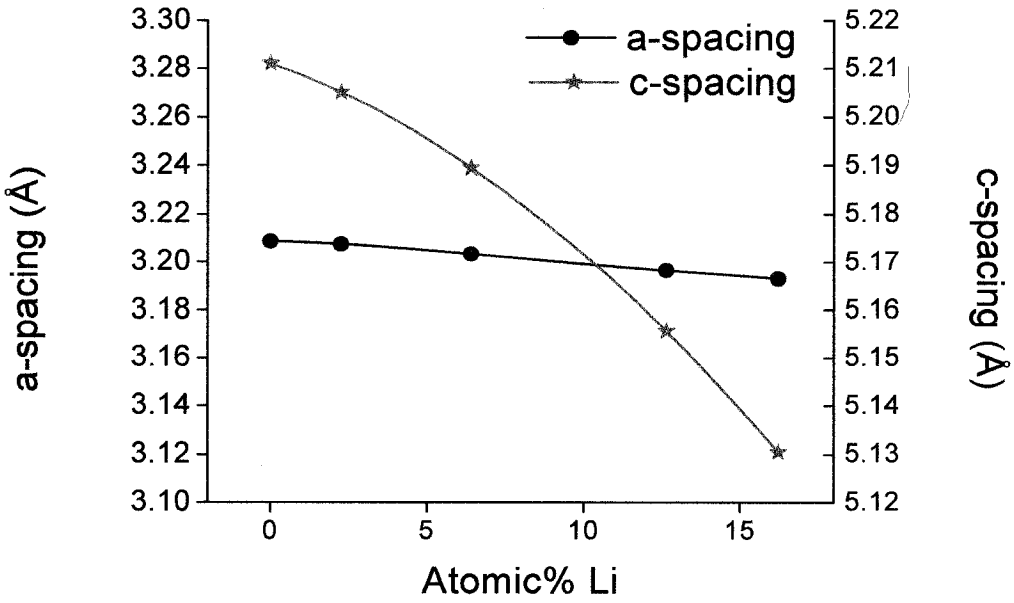

Figure 4.8: Lattice parameter changes with increasing Li concentration

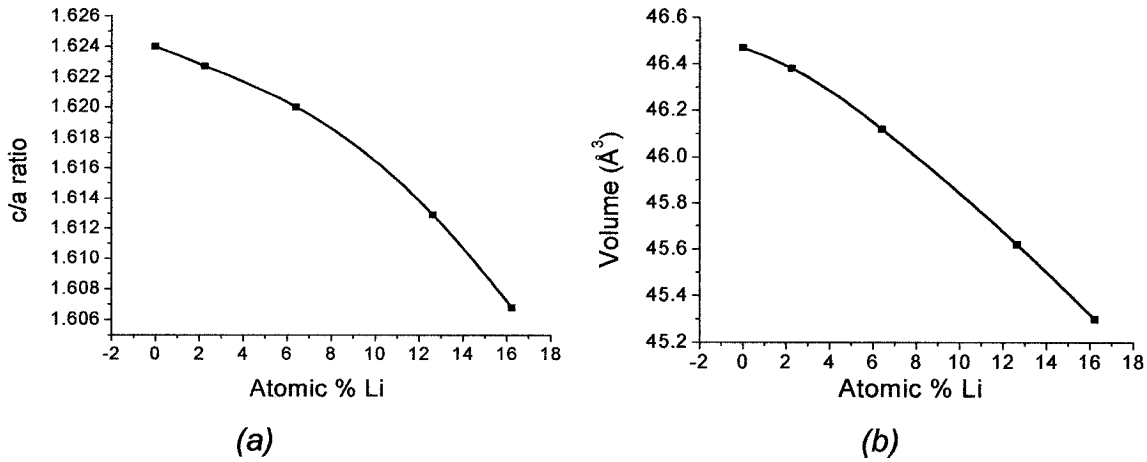

Figure 4.9: Changes to the (a) axial ratio (c/a)and (b) volume of the unit cell with increasing In concentration

Once lattice parameters were measured, the resulting interplanar spacings for the planes of interest were calculated and recorded in Table 4.6. An overall decrease of the interplanar spacings (d) was observed for all the planes. However, d-spacing of the basal planes {0002} was reduced by 0.0403 whereas for the prismatic $\{10\bar{1}0\}$ and pyramidal $\{11\bar{2}2\}$ planes, a reduction of respectively 0.0137 and 0.0107 was observed.

Table 4.6: Changes in Interplanar Spacings of Mg-Li Binary Alloys

Alloy	Interplanar Spacings (Å)		
	{0002}	$\{10\bar{1}0\}$	$\{11\bar{2}2\}$
Mg	2.6056	2.7789	1.3662
Mg - 2.3Li	2.6026	2.7779	1.3654
Mg - 6.4Li	2.5948	2.7742	1.3629
Mg - 13Li	2.5778	2.7682	1.3583
Mg - 16Li	2.5653	2.7652	1.3554

Mg-In System

Addition of a higher valent solute like indium was carried out to observe an increase in the electronic concentration of the unit cell. Six different indium concentrations were added decreasing the grain size of the most dilute alloys from 521 μm to 173 μm at the highest concentration. Sample images of the six different Mg-In alloys at lower and intermediate magnifications can be observed in Figure 4.10 - Figure 4.15. The appearance of a white film was more obvious with increasing In concentrations, hence etching to reveal grain boundaries was a challenge for alloys with higher In concentration.

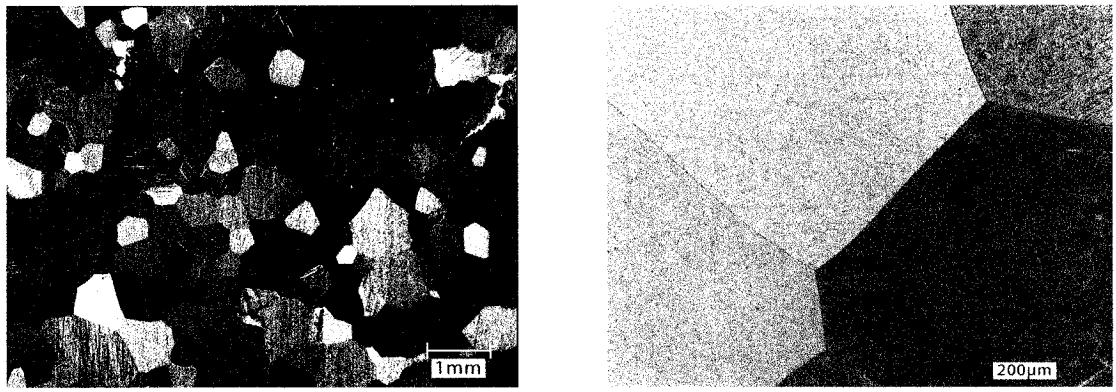

(a) (b)

Figure 4.10: Mg-0.1In alloy images taken at (a) lower magnification and (b) intermediate magnification. Grain size = 521 ± 57 µm.

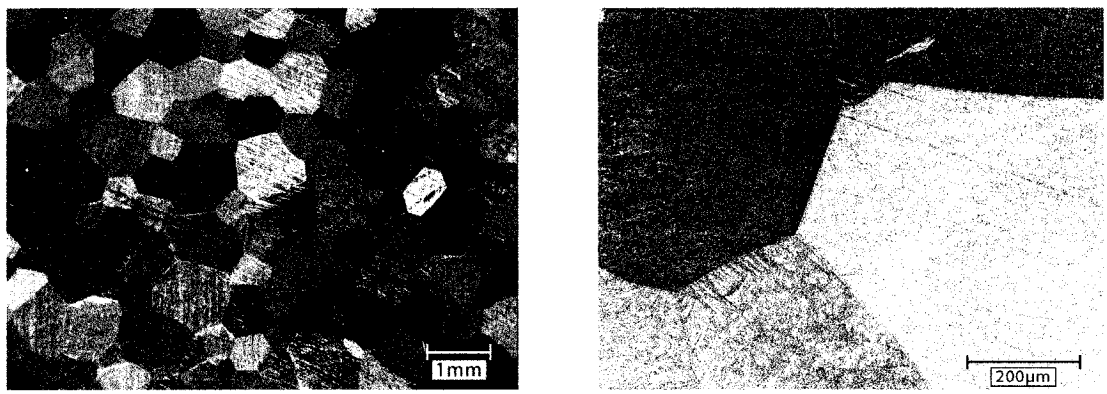

(a) (b)

Figure 4.11: Mg-0.2In alloy images taken at (a) lower magnification and (b) intermediate magnification. Grain size = 501 ± 66 µm

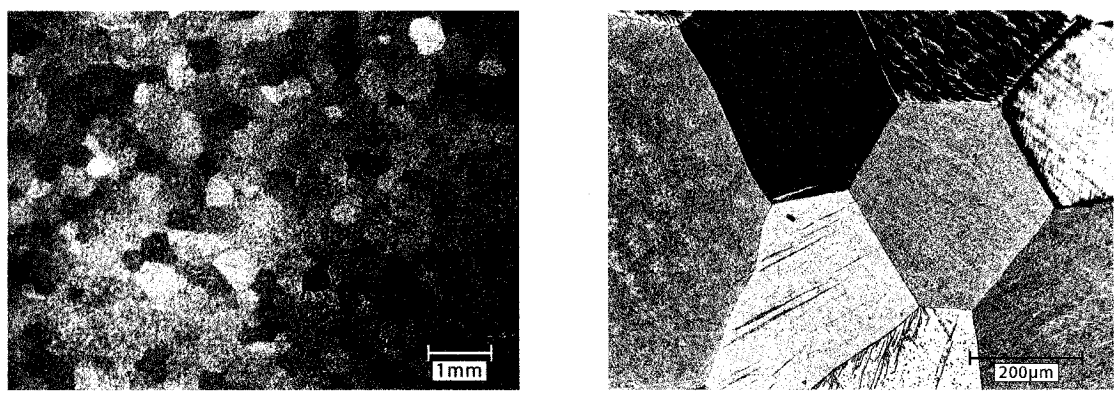

(a) (b)

Figure 4.12: Mg-0.8In alloy images taken at (a) lower magnification and (b) intermediate magnification. Grain size = 350 ± 20 µm.

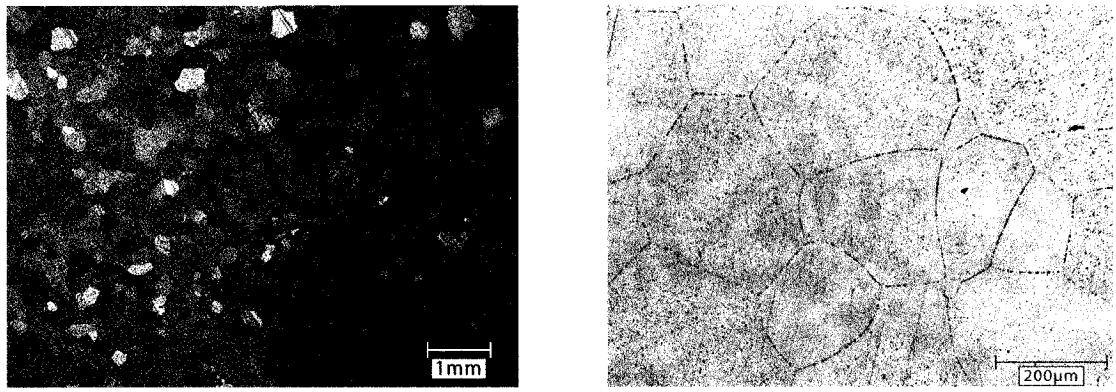

(a) (b)

Figure 4.13: Mg-2.2In alloy images taken at (a) lower magnification and (b) intermediate magnification. Grain size = 244 ± 48 µm.

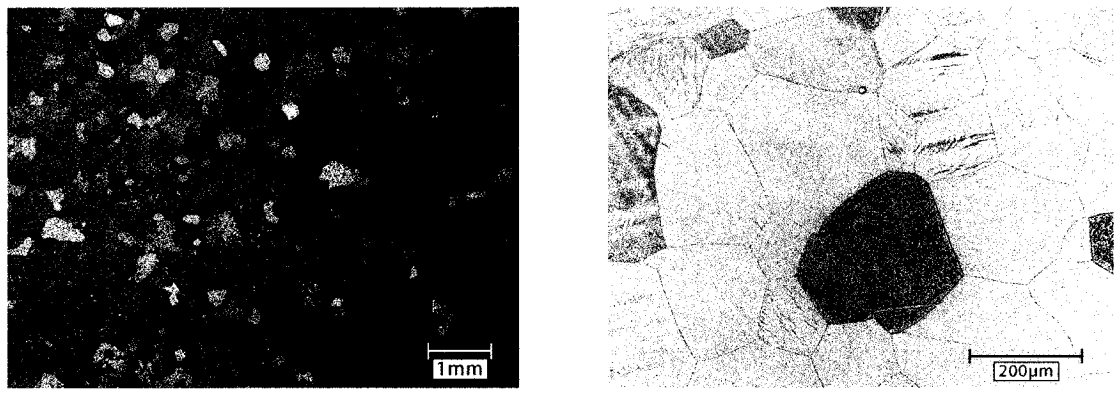

(a) (b)

Figure 4.14: Mg-2.8In alloy images taken at (a) lower magnification and (b) intermediate magnification. Grain size 188 ± 23µm

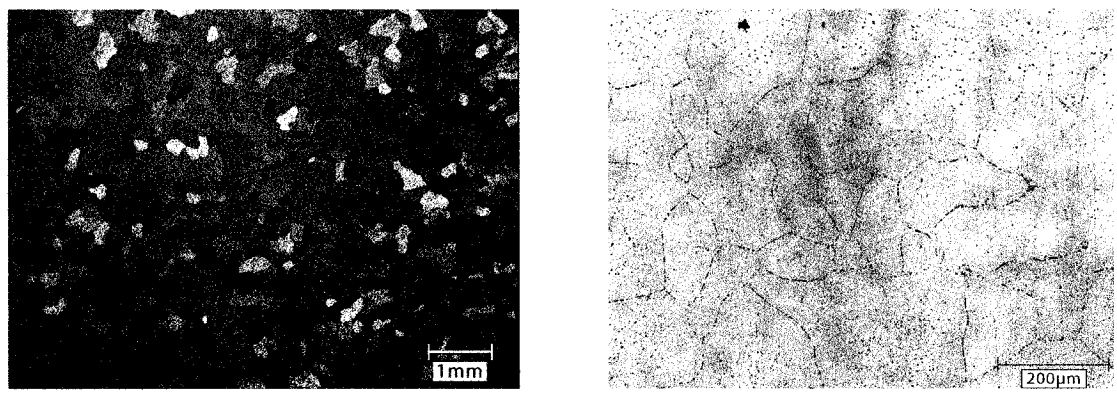

(a) (b)

Figure 4.15: Mg-3.3In alloy images taken at (a) lower magnification and (b) intermediate magnification. Grain size = 173 ± 21 µm.

X-ray diffraction results obtained for the Mg-In alloys did not show a pronounced shift of the Mg solid solution peaks given that changes to the lattice parameters were too small. Results for the six Mg-In binary alloys can be found in Table 4.7. Standard deviations were found to be always below 0.0003 for the a- spacing, 0.0004 for the c-spacing, 0.0002 for the c/a, and 0.01 for the volume of the unit cell.

Table 4.7: Results Obtained from XRD Data of Mg-In Alloys

Alloy Target Compositions	At % In	Wt% In	e/a	a-spacing (Å)	c-spacing (Å)	c/a	Volume ($Å^3$)
Mg	0.00	0.00	2.000	3.2088	5.2111	1.6240	46.47
Mg - 0.1 In	0.11	0.51	2.001	3.2095	5.2123	1.6240	46.50
Mg - 0.2 In	0.21	0.97	2.002	3.2094	5.2123	1.6240	46.50
Mg - 0.8 In	0.84	3.84	2.008	3.2084	5.2117	1.6244	46.46
Mg - 2.2 In	2.21	9.63	2.022	3.2062	5.2103	1.6251	46.39
Mg - 2.8 In	2.82	12.05	2.028	3.2054	5.2110	1.6257	46.37
Mg - 3.3 In	3.28	13.80	2.033	3.2049	5.2113	1.6261	46.35

Analysis of the results found in Table 4.7 reveal that the effect of In on the unit cell of pure Mg is much more complicated than initially expected. At lower In concentrations (below 0.5 at% In) the observed lattice parameter expansion can be attributed to In having a higher atomic size than Mg. No axial ratio changes were observed for these dilute alloys and it is believed that at this stage, the electronic concentration has not changed sufficiently so as to affect the lattice parameters through electron overlap.

More interestingly, when the In concentration increases above 0.25 at %, both lattice parameters contracted as can be distinguished from Figure 4.16. Contraction of the a-spacing with increasing concentration of a higher valent solute contradicts the theoretical explanation of the Brillouin zone overlap, where the a-spacing should expand with increasing solute. Previous work performed on Mg-In alloys with high In concentrations states that the lattice parameters are contracting slightly owing to the smaller atomic size of In [8]. Based on this fact, it is presumed that as the In concentration increases in Mg, the type of bonds may

change from metallic to covalent and the atomic size of In decreases so as to cause a contraction of the parameters. Raynor found that superimposed on the solute size effect, the increasing electronic concentration causes the a-spacing to contract much less than when Cd is added to Mg, where no electronic size effect is observed [8].

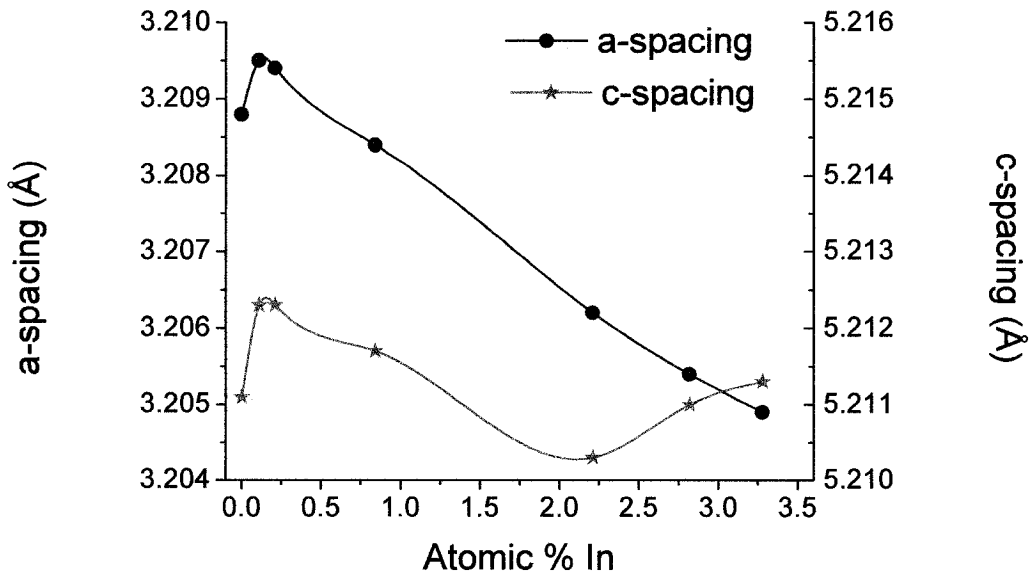

Figure 4.16: Lattice parameter changes with increasing In concentration

Evidence of this increasing electronic concentration with addition of In to Mg is observed as soon as the c-spacing expands at around 2.2 at% In (Figure 4.16). At this concentration, the electronic concentration is such that overlap of the electrons from the first Brillouin zone to the second occurs in another direction so as to expand the c-spacing. The observed critical In concentration where the c-spacing starts to expand agrees with the work carried out by F.W. von Batchelder et al in 1957 and contradicts the results found by Raynor in 1940 [39][41]. An overall increase in the axial ratio (Figure 4.17a) was observed based on the rising electronic concentration of the unit cell with the addition of In. Contraction of the unit cell volume was also observed and it seemed to follow the same trend as the one observed for the a-spacing (Figure 4.17b).

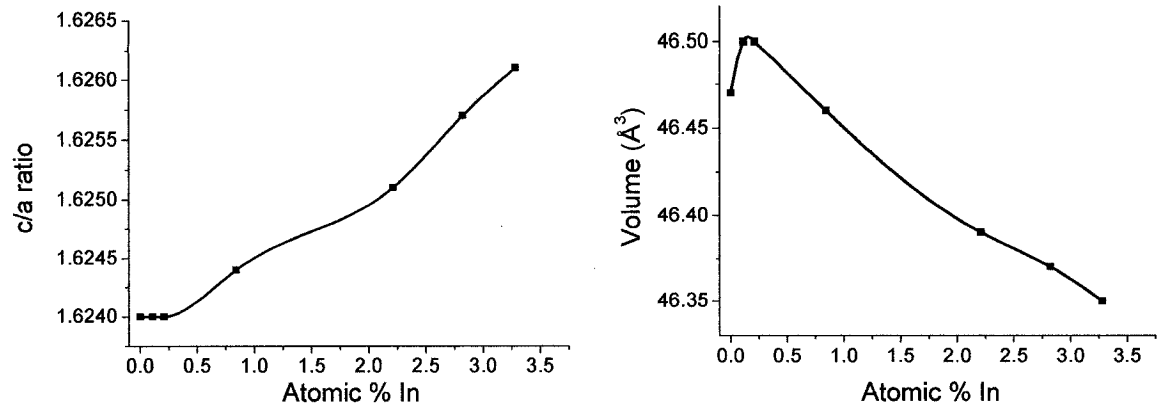

Figure 4.17: Changes to the (a) axial ratio (c/a)and (b) volume of the unit cell with increasing In concentration.

Changes in interplanar spacing for the basal, prismatic, and pyramidal planes of the different Mg-In binary alloys can be found in Table 4.8. It was observed that the addition of In affected the interplanar spacings for each plane differently. The d-spacing for the basal plane {0002} was seen to initially increase, then decrease and finally increase again. On the other hand, the interplanar spacings of the prismatic $\{10\bar{1}0\}$ and pyramidal $\{11\bar{2}2\}$ planes were seen to decrease by 0.0034 and 0.0012, respectively.

Table 4.8: Changes in Interplanar Spacings of Mg-In Binary Alloys.

Alloy	Interplanar Spacings (Å)		
	{0002}	$\{10\bar{1}0\}$	$\{11\bar{2}2\}$
Mg	2.6056	2.7789	1.3662
Mg - 0.1 In	2.6062	2.7795	1.3665
Mg - 0.2 In	2.6062	2.7794	1.3664
Mg - 0.8 In	2.6059	2.7786	1.3661
Mg - 2.2 In	2.6052	2.7767	1.3653
Mg - 2.8 In	2.6055	2.7760	1.3651
Mg - 3.3 In	2.6056	2.7755	1.3650

Mg-Zn System

Addition of Zn to pure Mg was carried out to observe the changes of lattice parameters caused by a smaller sized solute. With increased addition of Zn it was observed that grain size decreased from 210 μm to 80 μm as illustrated in Figure 4.18 - Figure 4.20.

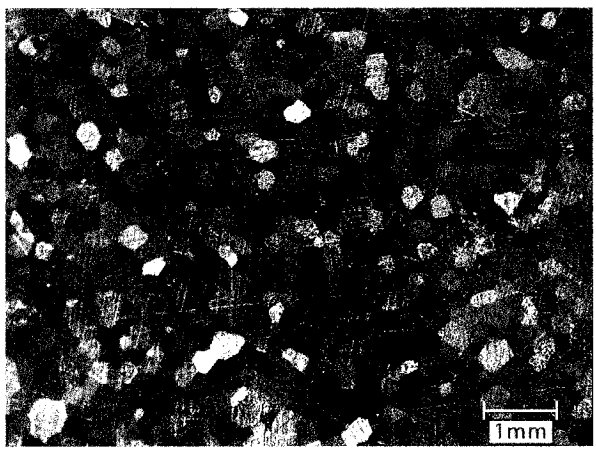

Figure 4.18: Mg-0.2Zn alloy image showing grains at lower magnification. Grain size = 210 ± 14 μm.

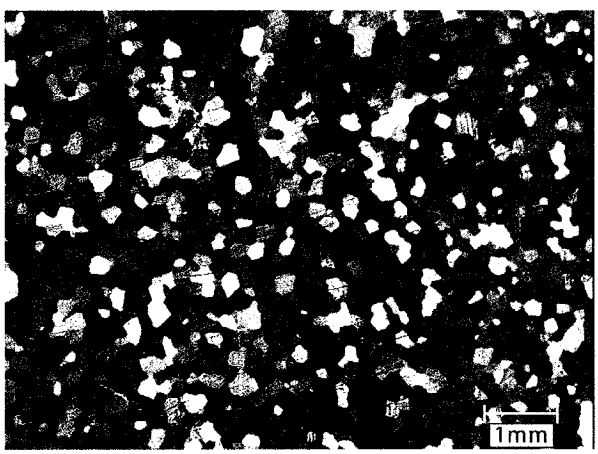

Figure 4.19: Mg-0.3Zn alloy image showing grains at lower magnification. Grain size = 160 ± 7 μm.

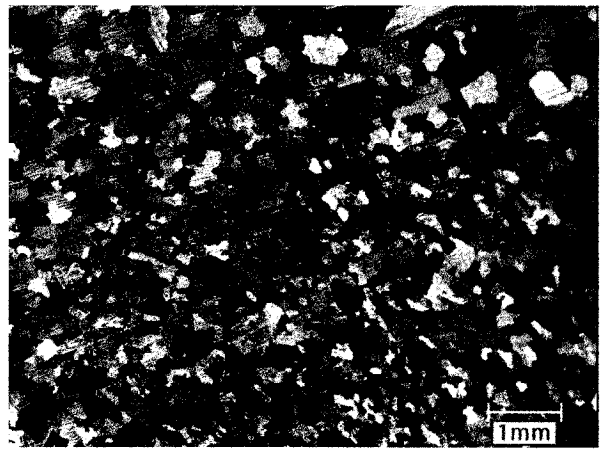

Figure 4.20: Mg-0.7Zn alloy image showing grains at lower magnification. Grain size = 126 ± 4 μm.

EPMA analysis carried out on Mg-Zn binary alloys found that in all the samples Zn was in solid solution with Mg. However, elemental mapping of Zn revealed that the alloys with a higher Zn content contained compositional inhomogeneities. Figure 4.21 shows images for Mg-0.2Zn and Mg-0.7Zn, where solute micro-segregation is readily observed on the alloy with a higher Zn concentration (Figure 4.21b). For lattice parameter measurements, powder samples were taken from different regions of the coupon and annealed so as to minimize these compositional inhomogeneities.

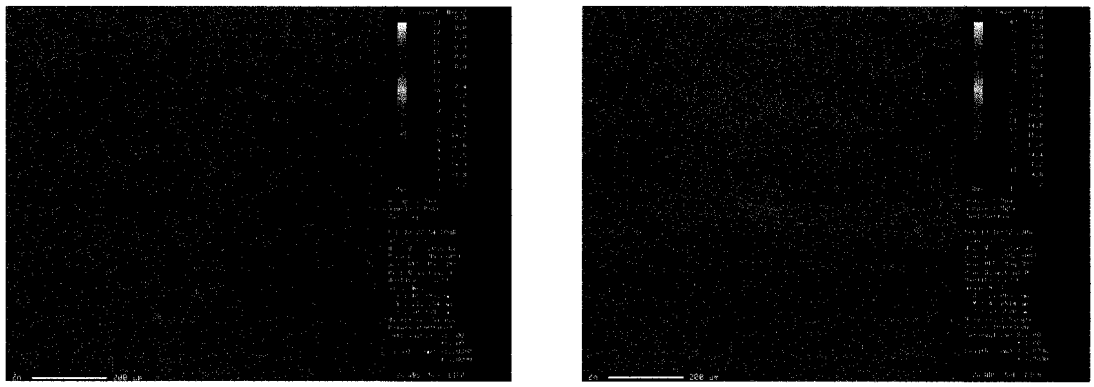

(a) *(b)*

Figure 4.21: Images showing elemental mapping of Zn on (a) Mg-0.2Zn and (b) Mg-0.7Zn samples.

Zinc with the smallest atomic size of the studied solute elements did in fact contract the lattice in both directions as can be observed from Table 4.9. Standard deviations for lattice parameter measurements were found to be always below 0.0005 for the a- and c-spacings, 0.0003 for the c/a ratio, and 0.01 for the volume of the unit cell.

Table 4.9: Results Obtained from XRD Data of Mg-Zn Alloys

Alloy Target Compositions	At % Zn	Wt% Zn	e/a	a-spacing (Å)	c-spacing (Å)	c/a	Volume ($Å^3$)
Mg	0.00	0.00	2.000	3.2088	5.2111	1.6240	46.47
Mg - 0.2Zn	0.19	0.51	2.000	3.2084	5.2107	1.6241	46.45
Mg - 0.3Zn	0.32	0.87	2.000	3.2076	5.2091	1.6240	46.41
Mg - 0.7Zn	0.70	1.86	2.000	3.2054	5.2049	1.6238	46.31

Changes to both lattice parameters of Mg with addition of Zn are illustrated in Figure 4.22. It can be observed that the contraction of the a-spacing and the c-spacing is occurring in the same degree, meaning that the addition of Zn to pure Mg has no apparent effect on the c/a ratio. Contraction of the volume of the unit cell was also observed and can be distinguished in Figure 4.23.

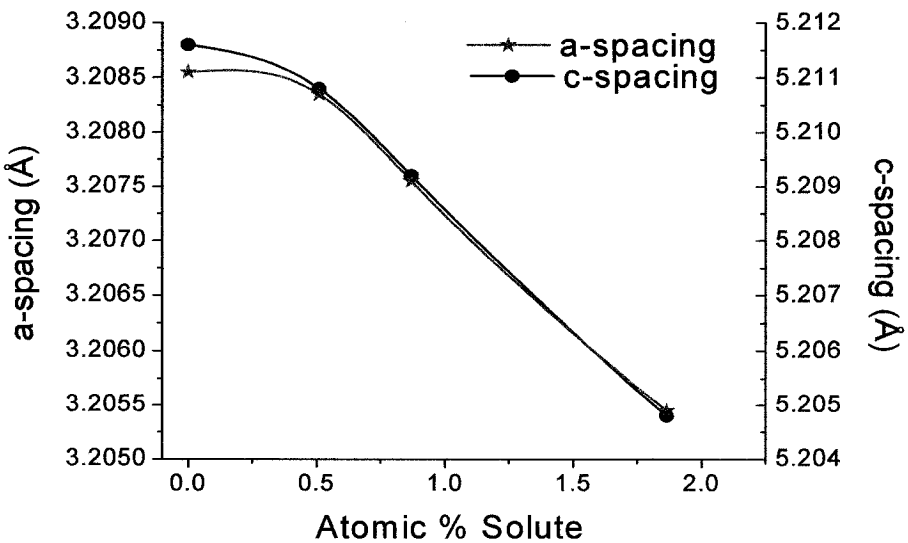

Figure 4.22: Lattice parameter changes with increasing Zn concentration.

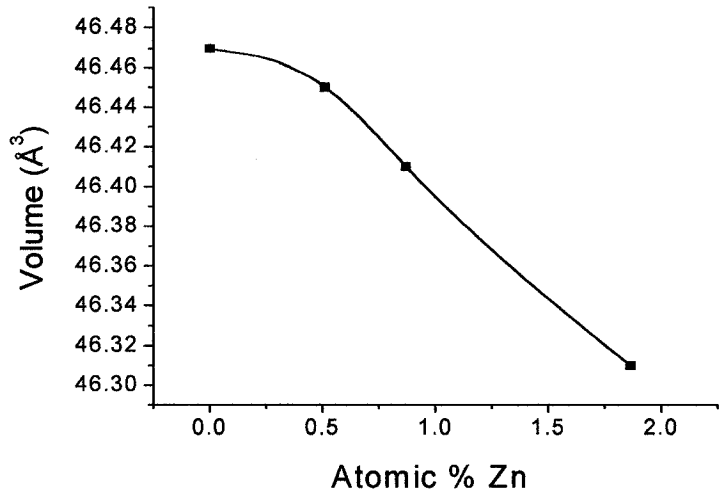

Figure 4.23: Changes to the volume of the unit cell with increasing Zn concentration.

Upon examination of the results obtained by Busk in the 1950's, it was observed that his investigation focused on Mg-Zn alloys with solute concentrations starting at 0.742 at% Zn [40]. In the present case, due to the observed appearance of solute inhomogenities with increasing Zn concentration (Figure 4.21), more dilute alloys were studied.

Calculated interplanar spacings for the Mg-Zn alloys are found in Table 4.9. With the contraction of both lattice parameters in all the Mg-Zn alloys, d-spacing of all the planes were seen to decrease as well. It was also noted that the interplanar spacing of the basal plane decreased by 0.0031, while the prismatic and pyramidal planes had a d-spacing decrease of 0.0029 and 0.0015, respectively.

Table 4.10: Interplanar Spacings for the Mg-Zn Binary Alloys

Alloy	Interplanar Spacings (Å)		
	{0002}	{1010}	{1122}
Mg	2.60555	2.7789	1.36617
Mg - 0.2Zn	2.60535	2.77856	1.36602
Mg - 0.3Zn	2.60455	2.77786	1.36566
Mg - 0.7Zn	2.60245	2.77596	1.36467

Mg-Ce System

Ce has very low solid solubility in Mg and second phase precipitates form even at very low solute levels. Presence of second phases refine the microstructure decreasing the grain size from 286 μm, at very low Ce levels, to 53 μm. Optical and scanning electron microscopy images for four Mg-Ce binary alloys can be found in Figure 4.24 - Figure 4.25. Cerium-rich particles were found in all of the binary alloys, precipitating along the grain boundaries as well as inside the grains.

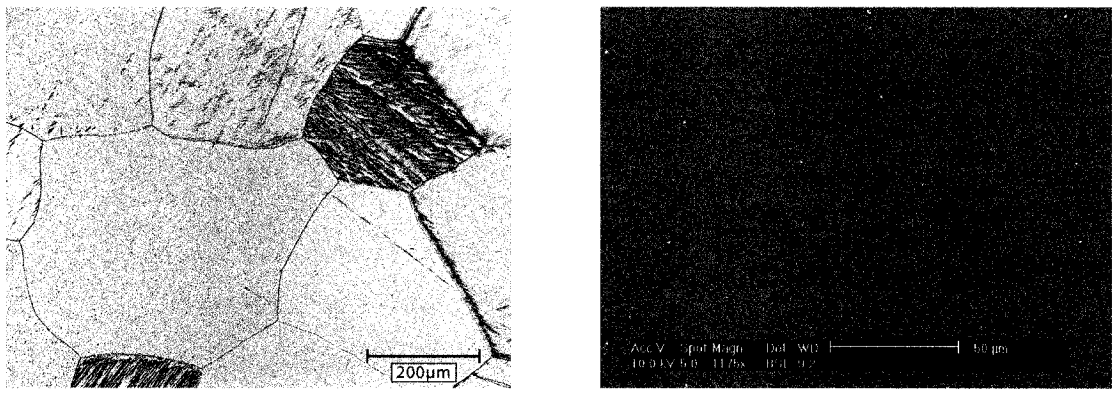

(a) (b)

Figure 4.24: Mg-0.003Ce alloy images at (a) lower magnification and at (b) high magnification. Grain sizes = 286 ± 30 μm.

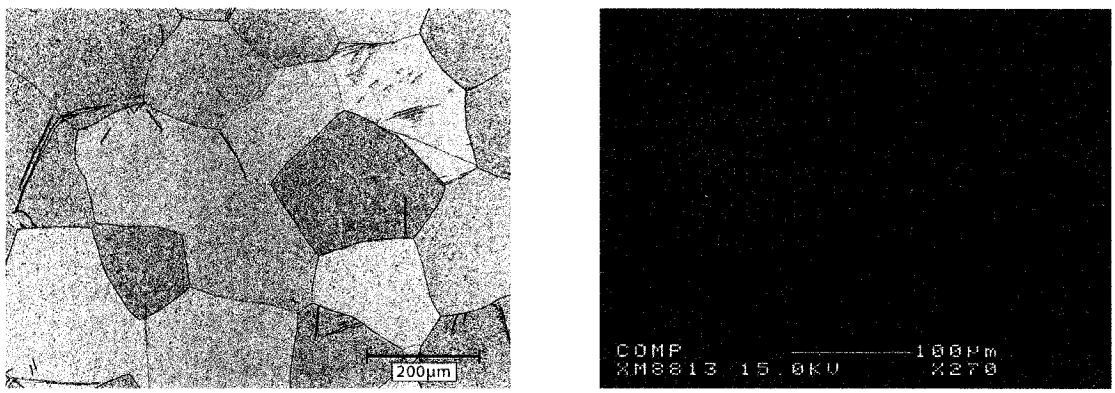

(a) (b)

Figure 4.25: Mg-0.01Ce alloy images at (a) lower magnification and at (b) high magnification. Grain sizes = 196 ± 19 μm.

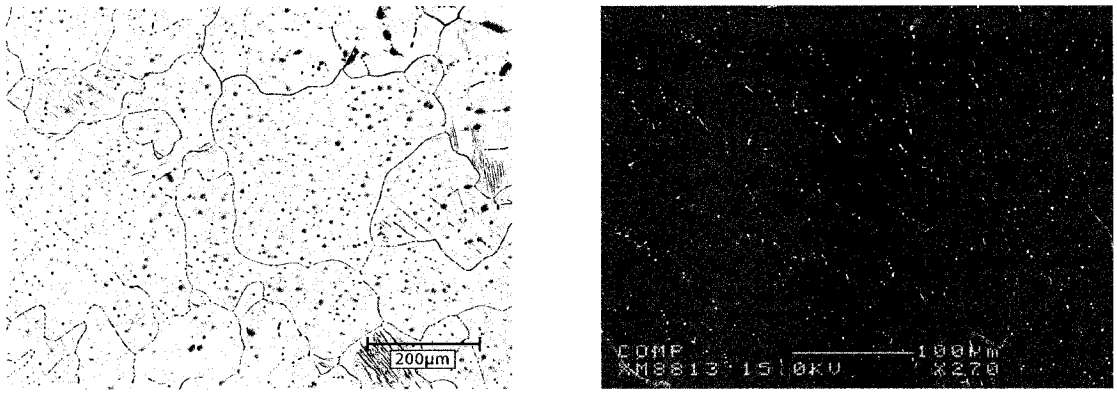

(a) (b)

Figure 4.26: Mg-0.06Ce alloy images at (a) lower magnification and at (b) high magnification. Grain sizes = 100 ± 10 µm.

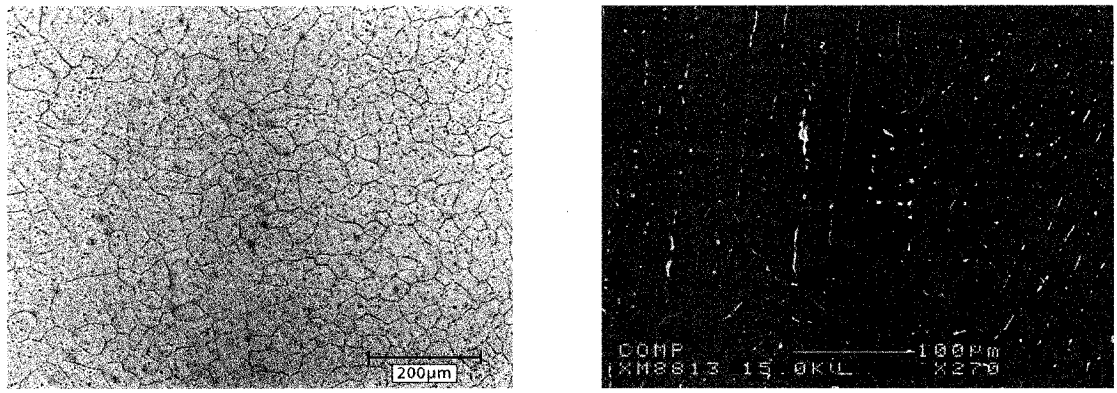

(a) (b)

Figure 4.27: Mg-0.13Ce alloy images at (a) lower magnification and at (b) high magnification. Grain sizes = 53 ± 2 µm

To determine if any Ce was in solid solution with Mg, EPMA spot analysis was carried out on the Mg-0.003Ce sample. Analysis revealed the amount of Ce dissolved in the Mg matrix varied from 0.0011 at% (0.006 wt%) to 0.0082 at% (0.047 wt%). Given the presence of Ce-rich precipitates in the sample bulk, determination of an accurate Ce concentration in the Mg matrix is almost impossible. However, the lattice parameter changes measured using x-ray diffraction reveal that there is in fact some amount of Ce in the Mg matrix. Lattice parameter results found for the Mg-Ce binary alloys can be found in Table 4.11.

Table 4.11: Results Obtained from XRD Data of Mg-Ce Alloys.

Alloy Target Compositions	At % Ce	Wt% Ce	e/a	a-spacing (Å)	c-spacing (Å)	c/a	Volume (Å^3)
Mg	0.00	0.00	2.000	3.2088	5.2111	1.6240	46.47
Mg - 0.003Ce	0.003	0.018	2.000	3.2086	5.2106	1.6240	46.47
Mg - 0.01Ce	0.01	0.03	2.000	3.2088	5.2110	1.6240	46.47
Mg - 0.06Ce	0.06	0.36	2.000	3.2093	5.2119	1.6240	46.49
Mg - 0.13Ce	0.13	0.72	2.000	3.2085	5.2110	1.6241	46.46

Measurement of the lattice parameters for this binary system was particularly difficult owing to the fact that the concentrations of the prepared alloys were too dilute and too similar to each other. Consequently, some of the observed lattice parameter changes were within the standard deviation. Only the observed lattice parameter expansion of the Mg-0.06Ce alloy was real and not within the standard deviation.

Additionally, it was observed that there was no axial ratio change in any of the Mg-Ce alloys contradicting the observed reduction of 0.00069 found by Busk [40]. Previous work does not give any indication of the quantity of Ce going into solid solution, thus the large reduction could be due to lower resolution of instruments or to a higher quantity of Ce in the solid solution. Due to the fact that only one Mg-Ce binary alloy gave reliable results, a relationship between the atomic% Ce and the lattice parameters could not be found.

Interplanar spacings calculated using the measured lattice parameters for the Mg-Ce binary alloys can be found in Table 4.12. The d-spacing increase or decrease with respect to Mg seems to follow changes associated to the lattice parameters. In the case of the Mg-0.06Ce alloy, which showed the expected lattice parameter change, an increase in d-spacing of all the planes was observed. However, an interplanar spacing increase of 0.0004 was observed for the basal and the prismatic planes while the pyramidal planes increased only by 0.0002.

Table 4.12: Interplanar Spacings for Mg-Ce Binary Alloys

Alloy	Interplanar Spacings (Å)		
	{0002}	{1010}	{1122}
Mg	2.60555	2.7789	1.36617
Mg - 0.003Ce	2.6053	2.77873	1.36607
Mg - 0.01Ce	2.6055	2.7789	1.36616
Mg - 0.06Ce	2.60595	2.77934	1.36638
Mg - 0.13Ce	2.6055	2.77864	1.36607

4.1.3 Multicomponent Alloys

After studying the individual solute effects on lattice parameters, a number of alloys with combinations of the four solutes were prepared. A concentration inside the solid solution region for binary phase diagram was chosen for all of the solutes, with the exception of Ce, which forms second phases even at low solute levels. A concentration of 1 wt% was chosen for both Zn and In, 2 wt% was selected for Li, and 0.3 wt% was chosen for Ce. Compositions of the prepared alloys can be found in Table 3.2. Calculated lattice parameters and the axial ratios of the multicomponent alloys are found in Table 4.13.

Table 4.13: Results Obtained from XRD Data of Multicomponent Alloys

Alloy	Target Compositions	e/a	a-spacing (Å)	c-spacing (Å)	c/a
0	**Mg**	2.000	3.2088	5.2111	1.6240
1	**Mg-0.3Ce-2Li**	1.925	3.2000	5.1763	1.6176
2	**Mg-0.3Ce-1In**	2.002	3.2089	5.2114	1.6240
3	**Mg-0.3Ce-1Zn**	2.000	3.2076	5.2090	1.6240
4	**Mg-1In-2Li**	1.925	3.1999	5.1763	1.6177
5	**Mg-1In-1Zn**	2.002	3.2072	5.2086	1.6240
6	**Mg-1Zn-2Li**	1.938	3.2006	5.1811	1.6188
7	**Mg-0.3Ce-1In-1Zn**	2.002	3.2078	5.2095	1.6240
8	**Mg-0.3Ce-1In-2Li**	1.928	3.2006	5.1780	1.6178
9	**Mg-0.3Ce-1Zn-2Li**	1.928	3.1990	5.1748	1.6176
10	**Mg-1Zn-1In- 2Li**	1.940	3.1991	5.1794	1.6190
11	**Mg-0.3Ce-1Zn-1In-2Li**	1.926	3.1986	5.1737	1.6175

Standard deviations were found to be always below 0.0006 for the a-spacing, 0.0007 for the c-spacings, 0.0005 for the c/a ratio, and 0.02 for the volume of the unit cell. Lattice parameters changes were observed in all of the alloys, but axial ratio changes were only observed on Li-containing alloys. It needs to be noted that the electronic concentrations were calculated assuming that all of the solutes go into solid solution with Mg, which is not true when solutes are mixed. Therefore, these electronic concentrations are just an approximation.

Interplanar spacings were also determined for these alloys and they can be found in Table 4.14. The greatest change in d-spacing was for the basal planes, more specifically for those alloys containing Li.

Table 4.14: Interplanar Spacings for Multicomponent Alloys

Alloy	Target Compositions	Interplanar Spacings (Å)		
		{0002}	{10$\bar{1}$0}	{11$\bar{2}$2}
0	Mg	2.6056	2.7789	1.3662
1	Mg-0.3Ce-2Li	2.5882	2.7713	1.3609
2	Mg-0.3Ce-1In	2.6057	2.7790	1.3662
3	Mg-0.3Ce-1Zn	2.6045	2.7779	1.3657
4	Mg-1In-2Li	2.5882	2.7712	1.3609
5	Mg-1In-1Zn	2.6043	2.7775	1.3655
6	Mg-1Zn-2Li	2.5906	2.7718	1.3615
7	Mg-0.3Ce-1In-1Zn	2.6048	2.7780	1.3658
8	Mg-0.3Ce-1In-2Li	2.5890	2.7718	1.3613
9	Mg-0.3Ce-1Zn-2Li	2.5874	2.7704	1.3605
10	Mg-1Zn-1In-2Li	2.5897	2.7705	1.3609
11	Mg-0.3Ce-1Zn-1In-2Li	2.5809	2.7701	1.3603

4.2 Formability Assessment

Rolling and compression tests were carried out on pure Mg and three alloys to see the effect of the axial ratio on formability. Due to time constraints, only three alloys were assessed and they were selected since they had a low, high, and non-changing axial ratio with respect to Mg. Lattice parameters and axial ratios of the alloys used for rolling and compression tests are found in Table 4.15.

Table 4.15: Lattice Parameters and Axial Ratios of Alloys Used to Assess Formability.

Nominal Compositions	a-spacing (Å)	c-spacing (Å)	c/a	Volume ($Å^3$)
Mg-1Zn-2Li	3.2009	5.1823	1.6190	45.98
Mg	3.2088	5.2111	1.6240	46.47
Mg-1Zn-1In	3.2069	5.2084	1.6241	46.39
Mg-3Al-1Zn	3.1993	5.1976	1.6246	46.07

4.2.1 Grain Structures of Alloys

Macrographs of the alloys investigated are presented in Figure 4.28. As expected the grain structure of pure Mg (Figure 4.28a) consists mainly of columnar grains because it is a pure metal. A homogeneous, fine-grained structure is observed for Mg-3Al-1Zn (Figure 4.28b), while Mg-1Zn-2Li (Figure 4.28c), and Mg-1Zn-1In (Figure 4.28d) contain a grain structure with a mixture of both columnar and equiaxed grains.

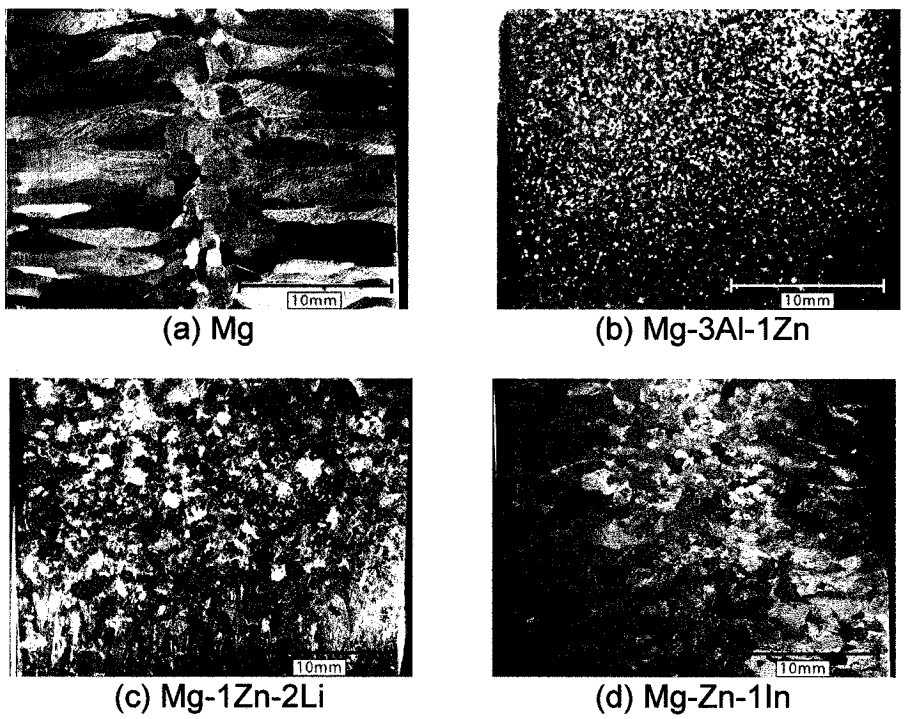

(a) Mg (b) Mg-3Al-1Zn

(c) Mg-1Zn-2Li (d) Mg-Zn-1In

Figure 4.28: Grain structures of thick plate cast Mg-based alloys.

4.2.2 Rolling Tests

Photos of the rolled specimens can be found in Figure 4.29 where the sample on the left was rolled for 7 passes (ε = 0.3) and the one on the right after 15 passes (ε = 0.55). Qualitative analysis of the specimens revealed that the Mg-1Zn-2Li and Mg-1Zn-1In samples had small cracks on the surface, while larger cracks along the edges were observed on the pure Mg sample. The Mg-3Al-1Zn sample had no visible cracking.

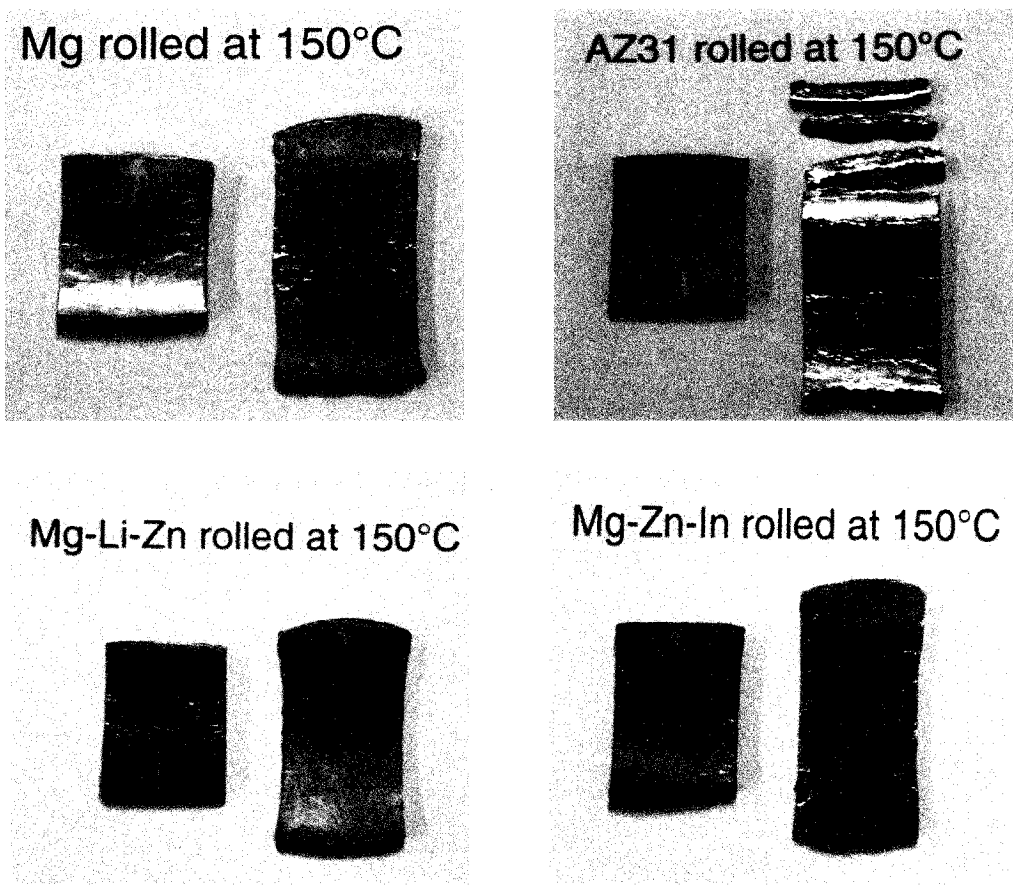

Figure 4.29: Photos of alloy specimens rolled at 150°C. In each photo the sample on the left is after 7 passes (ε = 0.3) and the on the right after 15 passes (ε = 0.55).

4.2.3 Compression Tests

Deformation characteristics of the Mg based alloys were also studied using compression tests which involve deformation mechanisms different from those seen in rolling. Flow curves were obtained for the alloy specimens deformed both at room temperature and 150°C. Stress-strain results obtained from the samples compressed to failure were graphed in order to observe the flow behavior and repeatability of results for the different alloys at RT and 150°C. Specimen surface following compression to a strain of 0.2 was compared, as well. Stress-strain curves along with photos of the compressed samples can be found in Figure 4.30 and Figure 4.31.

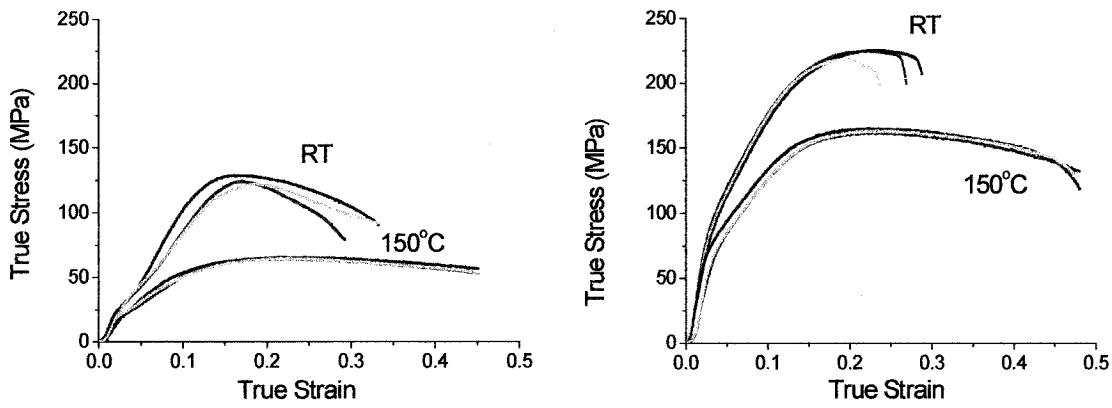

(a) Pure Mg (b) Mg-3Al-1Zn

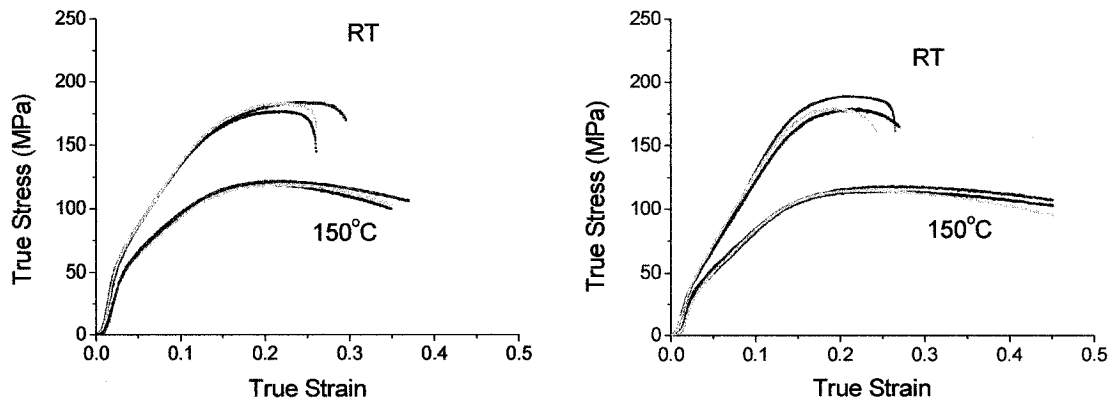

(a) Mg-2Li-1Zn (b) Mg-1In-1Zn

Figure 4.30: Stress-strain curves for alloy specimens compressed to failure at RT and 150°C

It was observed that as temperature increased the shape of the curve changed, UTS decreased, and the repeatability of the results increased. An increase in temperature meant better deformation behavior and easier flow. Figure 4.30 shows that the compression tests carried out at 150°C have more consistent flow behavior, while the samples tested at room temperature exhibited different flow curve shapes.

It was difficult to obtain quantitative data from the compression curves, given that the onset of shearing is unknown. Comparison of the stress-strain curves show that results are more consistent when the testing temperature is increased. Figure 4.31a shows that pure Mg specimens tested at RT did not show repeatability, while those tested at 150°C do. Nevertheless, Mg-3Al-1Zn and Mg-2Li-1Zn gave more or less consistent results at both temperatures. Furthermore, it was observed that the Mg-3Al-1Zn alloy had the highest strength.

(a) Compressed specimens at room temperature

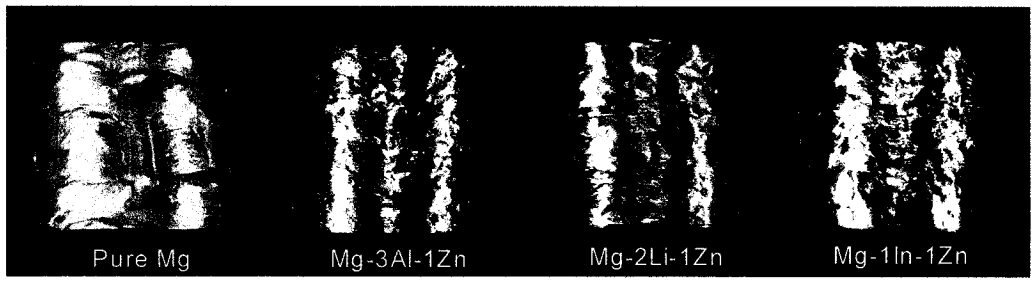

(b) Compressed specimens at 150°C

Figure 4.31: Photos of specimens compressed at (a) room temperature and (b) 150°C to a strain of 0.2 with strain rate of 10^3 s^{-1}

Qualitative analysis of the specimens compressed to a strain of 0.2 was carried out to determine condition of the surface following deformation and to determine if any failure occurred. The compressed specimens were compared and ranked accordingly, the results can be found in Table 4.16.

Table 4.16: Ranking of Compression Specimens

Alloy	***Surface Condition***	***Ranking***
Mg	*Failure, shears*	*Poor*
Mg-3Al-1Zn	*Smooth*	*Very Good*
Mg-2Li-1Zn	*Dimpled*	*Good*
Mg-1In-1Zn	*Dimpled*	*Medium*

CHAPTER 5 - DISCUSSION

This section will discuss the significance of the acquired results, comparing them against theories and previous research carried out in the mid 1900's. Addition of the four different solutes was originally carried out to only study their effect on the lattice parameters and the axial ratio of pure Mg. However, while performing characterization of the binary alloys it was observed that each solute had a different effect on the grain size as well. Due to the large quantity of prepared alloys, Microstructural characterization was only carried out on the binary solid solution alloys. Nevertheless, lattice parameters measurements were performed on all of the alloys so as to study the individual solute and combined effects of solutes on the lattice parameters. Moreover, rolling and compression tests were carried out to compare the deformation behavior of some alloys to pure Mg.

5.1 Comparison of Binary Systems

Lattice parameters, axial ratio, and volume of the unit cell comparisons can be found in Figure 5.1 through Figure 5.4. Linear equations were obtained for the Mg-Zn, Mg-In, and Mg-Li binary alloy systems. Given the low solubility of Ce in Mg, it was impossible to get a relationship for this system. Equations of the following form were obtained:

$$a_o = a_{Mg} + m_a x$$
$$c_o = c_{Mg} + m_c x$$
$$c/a = c/a_{Mg} + m_{c/a} x$$

Where x is the atomic percent solute added.

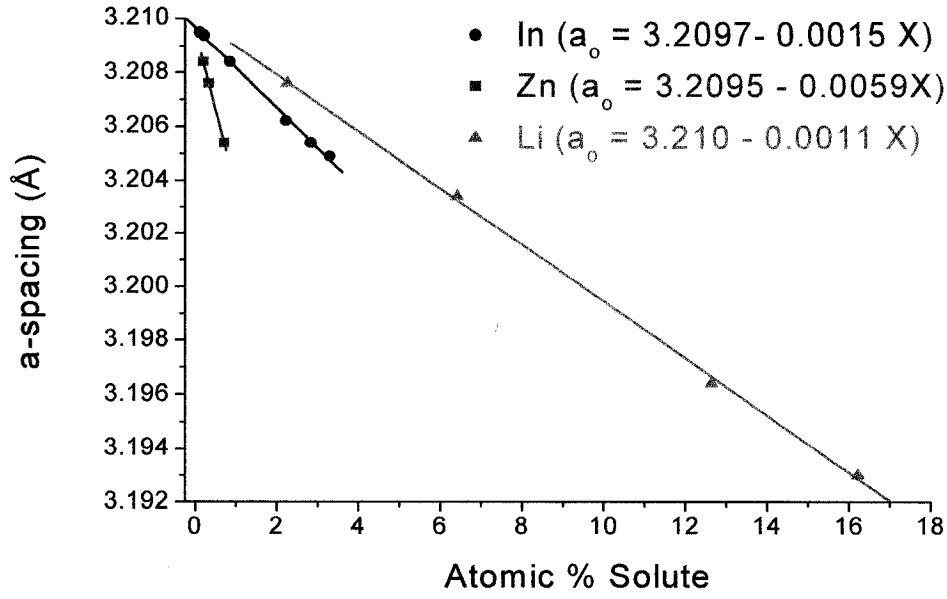

Figure 5.1: Lattice parameter a_o of binary solid solutions of In, Li, and Zn in Mg vs atomic percent solute.

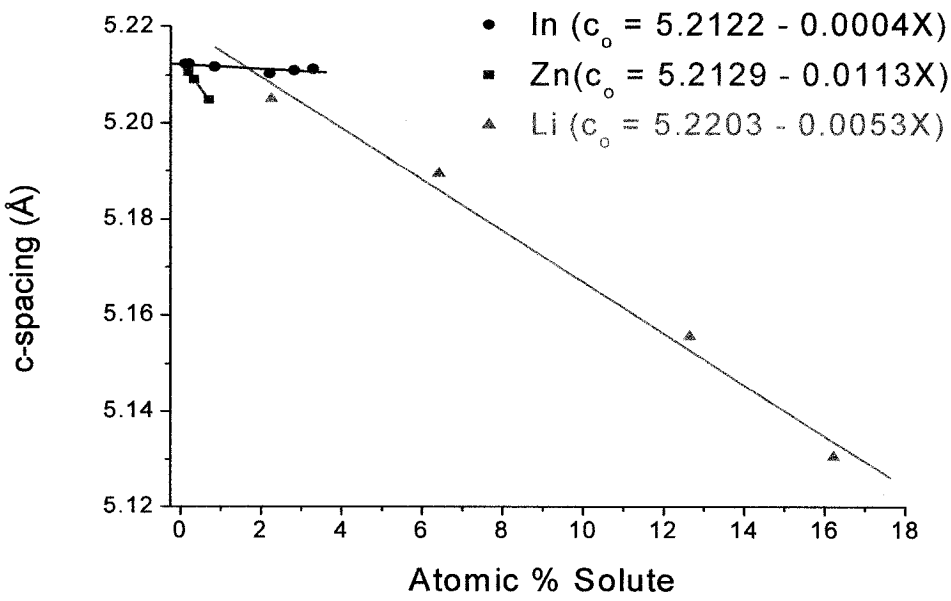

Figure 5.2: Lattice parameter c_o of binary solid solutions of In, Li, and Zn in Mg vs atomic percent solute.

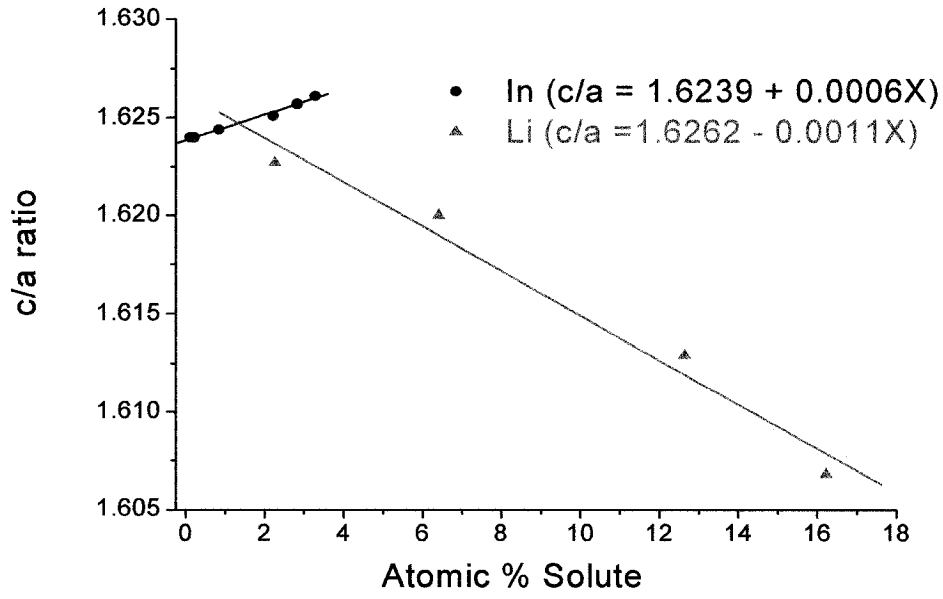

Figure 5.3: Axial ratio (c/a) of binary solid solutions of In, and Li in Mg vs atomic percent solute

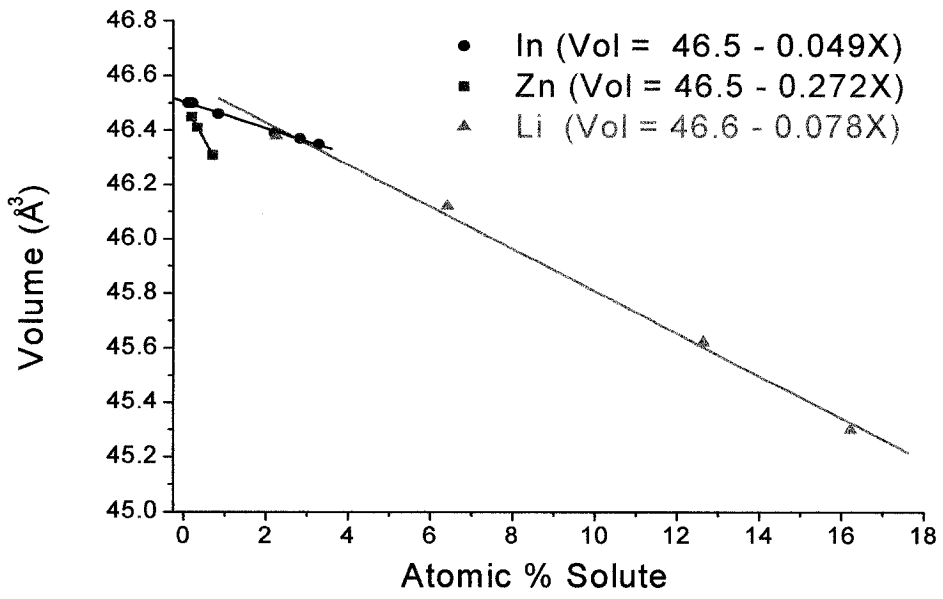

Figure 5.4: Unit cell volume of binary solid solutions of In, Li, and Zn in Mg vs atomic percent solute

A summary of the data obtained from the plots can be found in Table 5.1, along with the data for pure Mg.

Table 5.1: Summary of Parameter and Volume Data Obtained from the Plots.

Elements	a_o (Å)		c_o (Å)		c/a		Vol (Å^3)	
	a_{Mg}	m_a	c_{Mg}	m_c	c/a_{Mg}	$m_{c/a}$	Vol_{Mg}	m_{vol}
Magnesium	3.2088		5.2111		1.6240		46.5	
Indium	3.2097	-0.0015	5.2122	-0.0004	1.6239	0.0006	46.5	-0.05
Lithium	3.2100	-0.0011	5.2203	-0.0053	1.6262	-0.0011	46.5	-0.08
Zinc	3.2095	-0.0059	5.2129	-0.0113	1.6240	0	45.5	-0.27

It was observed that the lattice parameters of pure Mg obtained with the linear functions of the Mg-In and Mg-Zn alloys are really similar to each other and to the results of the pure Mg sample. In contrast, the constants obtained with the Mg-Li linear function are higher, especially for the axial ratio. This difference could be caused by the fact that changes to the lattice parameters with the addition of Li are greater than with addition of In or Zn, therefore the standard deviations are also higher. The same trend was observed by Busk in 1950 [40]. Comparison of the linear functions obtained in this study with the data obtained in his work show that the slope of the lines are dependent on the individual effect that the solute (solute size, valence or both) has over the parameters. While the intercept is proportional to the purity of the starting pure Mg used to make the alloys.

5.2 c/a and e/a relationship

Using the results obtained for Mg-In and Mg-Li alloys, an empirical relationship, between the axial ratio (c/a) and the electronic concentration (e/a) was determined where $\mathbf{c/a = -0.34(e/a)^2 + 1.38(e/a) + 0.20}$, as can be observed in Figure 5.5. The equation can be used to determine the required electronic concentration that an alloy would need to get a specific axial ratio. It should be noted that this relation is valid only for hcp magnesium alloys. It would be interesting to obtain similar relationships for other hcp metals such as Zn and Ti.

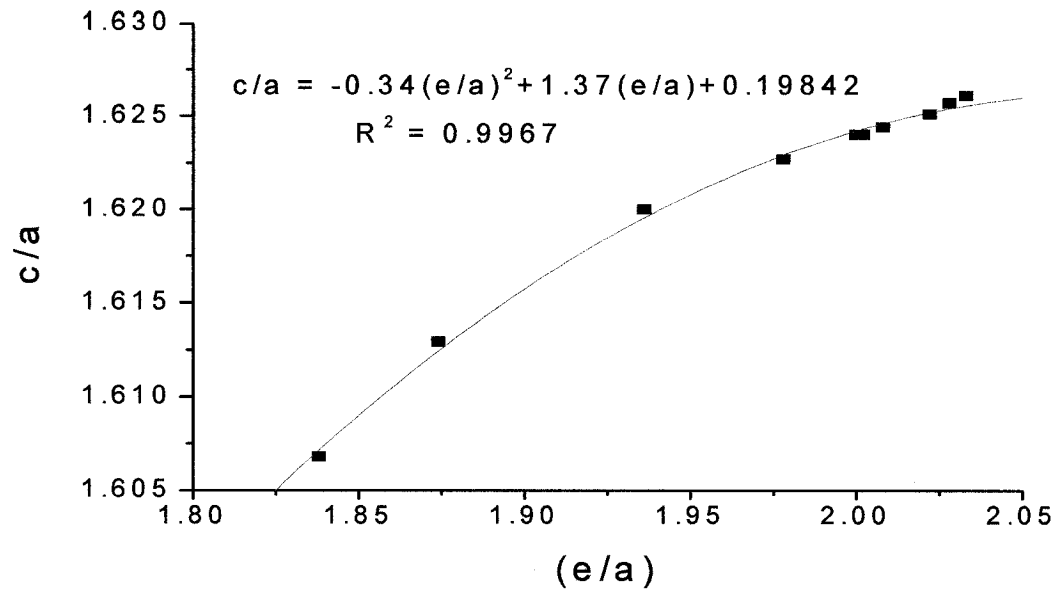

Figure 5.5: Relationship of axial ratio and electronic concentration

5.3 Multicomponent Alloys

Analysis of the lattice parameters and chemical compositions of the multicomponent atoms reinforce the observations made with the binary alloys. Of the prepared alloys, the ones listed in Table 5.2 show no change in axial ratio when compared to pure Mg and they also have a higher or the same electronic concentration. Alloys are listed according to their lattice parameter values, from highest to lowest.

Table 5.2: Lattice parameters of multicomponent alloys with a constant axial ratio

Alloy	Target Compositions	e/a *	a-spacing (Å)	c-spacing (Å)	c/a
0	**Mg**	2.0000	3.2088	5.2111	1.6240
2	**Mg-0.3Ce-1In**	2.0021	3.2089	5.2114	1.6240
7	**Mg-0.3Ce-1In-1Zn**	2.0021	3.2078	5.2095	1.6240
3	**Mg-0.3Ce-1Zn**	2.0000	3.2076	5.2090	1.6240
5	**Mg-1In-1Zn**	2.0021	3.2072	5.2086	1.6240

* *Alloying elements are not always in solid solution*

It was observed that with the addition of just 1wt% In, the electronic concentration of the alloys increased slightly, but not enough to cause an axial ratio increase. At this concentration, any changes caused by the indium atom would likely be due to its higher metallic atomic size with respect to Mg. Any additional amounts of In added to any of these alloys (if in solid solution) would increase their electronic concentration consequently increasing the axial ratio. Yet, lattice parameters will contract given that at higher concentrations of In in Mg, metallic bonds change to covalent and the atomic size of In with respect to Mg decreases. Therefore, alloy 2 in Table 5.2 has larger lattice parameters than pure Mg mainly because of the atomic size effect of larger atoms Ce and In. The instant Zn is added, as can be observed from alloys 3, 5, and 7, the electronic concentration stays the same, but the individual lattice parameters decrease owing the smaller size of Zn.

The rest of the prepared multicomponent atoms did exhibit and electronic concentration and axial ratio decrease. These alloys are can be found in Table 5.3 and they are organized from high to low axial ratio.

Table 5.3: Lattice Parameters of Multicomponent Alloys with Electronic Concentration and Axial Ratio.

Alloy	Target Compositions	e/a *	a-spacing (Å)	c-spacing (Å)	c/a
0	Mg	2.0000	3.2088	5.2111	1.6240
10	Mg-1Zn-1In- 2Li	1.9396	3.1991	5.1794	1.6190
6	Mg-1Zn-2Li	1.9381	3.2006	5.1811	1.6188
8	Mg-0.3Ce-1In-2Li	1.9279	3.2006	5.1780	1.6178
4	Mg-1In-2Li	1.9246	3.1999	5.1763	1.6177
9	Mg-0.3Ce-1Zn-2Li	1.9276	3.1990	5.1748	1.6176
1	Mg-0.3Ce-2Li	1.9249	3.2000	5.1763	1.6176
11	Mg-0.3Ce-1Zn-1In-2Li	1.9259	3.1986	5.1737	1.6175

** Alloying elements are not always in solid solution*

Close inspection of all these alloys reveal that all of them contain Li and this is the main reason why their electronic concentration and axial ratio decreases so much. The results reveal that alloys with a higher Li concentration were usually

the ones with the lowest axial ratio. Alloys 10 and 6 had a Li content of about 6.12 at% and this is why their c/a ratios are much larger than the rest of the alloys which have a Li content of 7.2 at% and above. It was also observed that some alloys have lower electronic concentration, but not always the lowest axial ratio. This usually happened to alloys containing In, where the electronic concentration increased slightly and where the axial ratio was only a result of the Li additions. Other atoms like Zn and Ce only had atomic size effects and they affected only the lattice parameters as they did with the binary alloys.

5.4 Interplanar spacing

It is known that at low temperatures deformation of Mg is limited to primary slip on the basal {0002} planes. Given that there is only a set of these planes, the formability at low temperatures is not exceptional. However, if the CRSS for non-basal planes such as the prismatic $\{10\bar{1}0\}$ and pyramidal $\{11\bar{2}2\}$ planes could somehow be lowered, then there is a slight chance that the deformation characteristics of Mg can be improved. For this reason, changes to the interplanar spacing (d) as a result of variations to the lattice parameters of pure Mg with addition of solute were monitored.

Interplanar spacings for each alloy were calculated with the obtained lattice parameters. The contraction of the lattice parameters observed with the addition of Li resulted in a large decrease of the interplanar spacing value. A decrease of the interplanar spacing value was also observed with other solutes such as In an Zn, but to a much lower extent. Interplanar spacing variations are directly related to variations of the lattice parameters and not to the variation of the axial ratio.

A decrease in the d-spacing of the basal plane occurred with addition of the different solutes as can be distinguished in Figure 5.6. On closer inspection of the results obtained with the Mg-In binary alloys (signaled by arrow), it can be seen that the interplanar spacings of the basal plane follow the same trend as that

observed for the c-spacing. Comparison of the d-spacing for the basal plane and the c-spacing of Mg-In alloys can be observed in Figure 5.7.

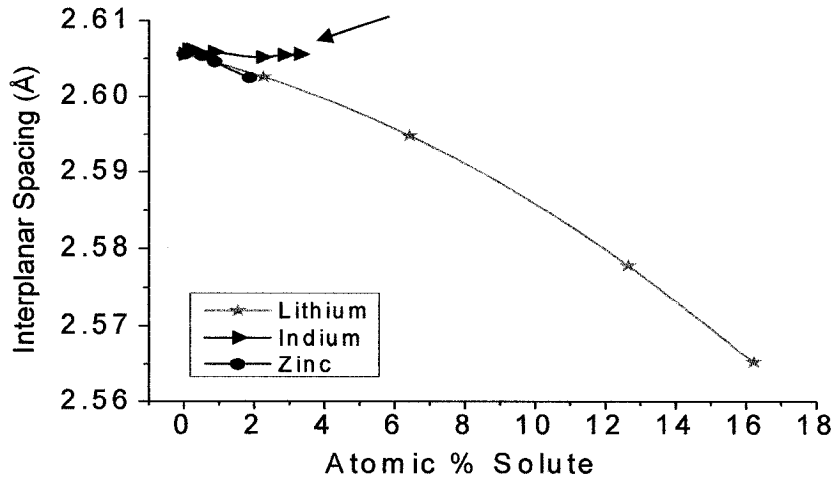

Figure 5.6: Changes of the interplanar spacing of the Basal planes with increasing solute content.

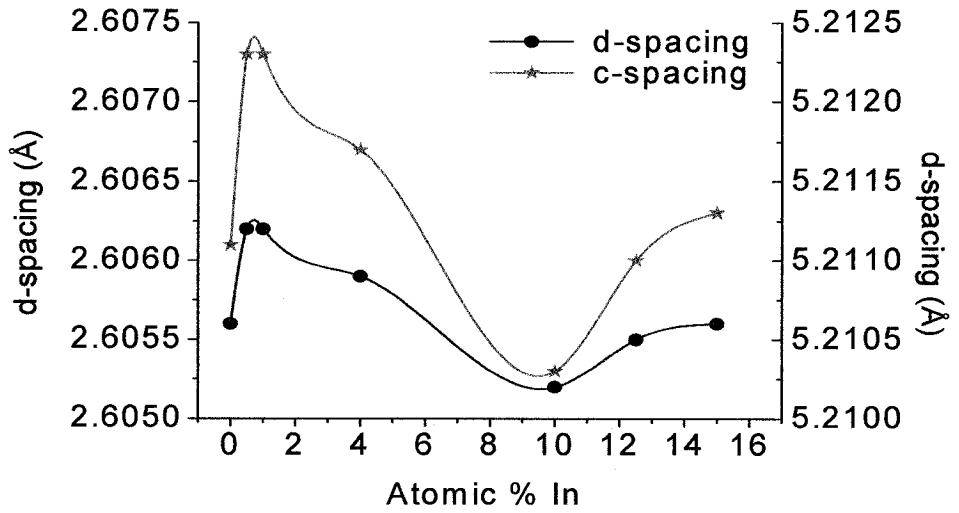

Figure 5.7: Comparison of the interplanar spacing changes for the basal {0002} plane and the c-spacings changes for Mg-In binary alloys.

It was determined that changes to the d-spacing are always half the changes of the c-spacing. Thus, if a solute happens to change the c-spacing much more than the a-spacing, then a larger d-spacing reduction will occur for the basal planes

than for the prismatic and pyramidal planes. This was certainly true for Li, where a larger d-spacing decrease was noticed for the basal plane.

The variations of the d-spacings for the $\{10\bar{1}0\}$ prismatic and the $\{11\bar{2}2\}$ pyramidal planes were also monitored. Figure 5.8 and Figure 5.9 compare the variations of the interplanar spacings for the prismatic and pyramidal planes with addition of the different solutes. The figures zoom into the Mg-In and Mg-Zn systems given that their changes were small when compared to those of Mg-Li.

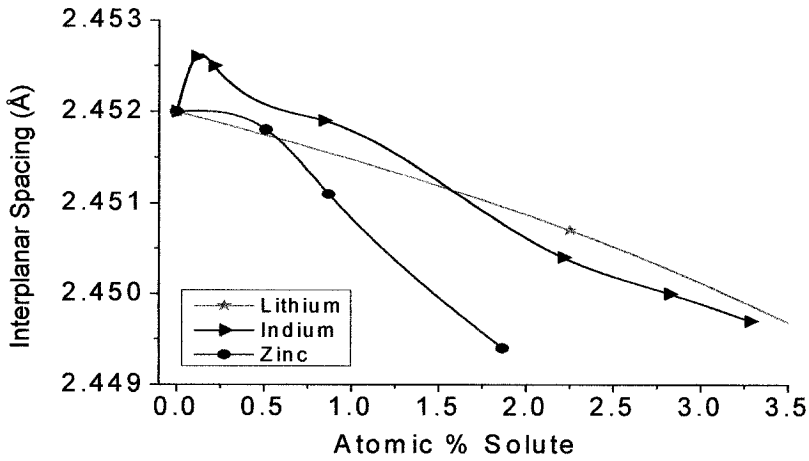

Figure 5.8: Zoomed portion showing changes of the interplanar spacings for the Prismatic plane with increasing solute content

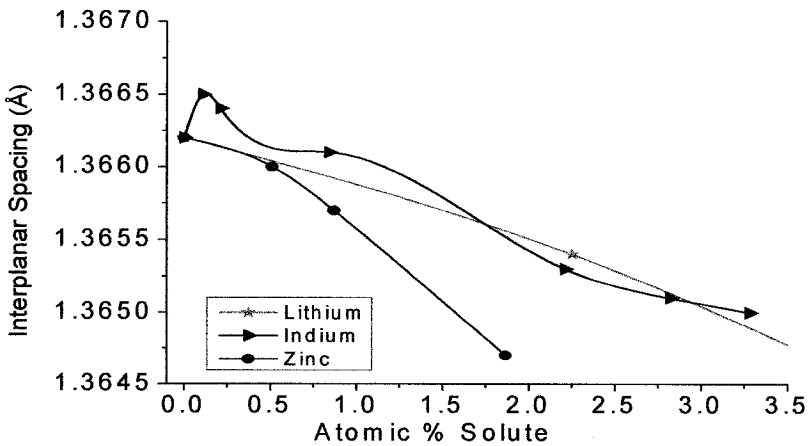

Figure 5.9: Zoomed portion showing changes of the interplanar spacings for the Pyramidal plane with increasing solute content

Interplanar spacing for the prismatic and pyramidal planes seem to be affected by both the a and the c-spacing. A consistent relationship between a specific lattice parameter and the d-spacing of either the prismatic or pyramidal plane was not found. However, it was observed that in every solute system the interplanar spacings of the prismatic plane reduced much more than the d-spacings of the pyramidal plane.

An increase of the interplanar spacings for non-basal planes would potentially decrease their critical resolved shear stress (CRSS). As a result, activation of non-basal slip would be easier therefore increasing the amount of available slip systems for deformation. The greater number of available slip systems would potentially improve the deformation characteristics of Mg wrought alloys. Hence, from the studied alloys it can be stated that there is a small window of opportunity for increase of non-basal slip.

Activation of non-basal slip could occur if the CRSS for non-basal planes decreases (d-spacing increase) or if the CRSS of the basal plane increases (d-spacing decrease). Figure 5.7 shows that in Mg-In alloys there is potential of diminishing the onset of basal slip by increasing its CRSS in Mg based alloys with an indium concentration that lies between 2 at% and 10 at% In. The fact that the basal plane d-spacing decreases may change the balance of deformation mechanisms, making the texture of rolled sheet more random. Since the d-spacing for prismatic and pyramidal planes increase for indium up to 0.25 at% this range seems to be worth investigating on its own. However, CRSS also depends on the burgers vector and shear modulus (G) which can sometimes be affected by alloying. TEM analysis should be considered in order to determine unknown variables and study the slip mechanisms with respect to different alloying additions.

5.5 Effect of Solute on Grain Size

Characterization of the binary alloys revealed that each solute can affect the grain structure of Mg quite differently. Grain size was observed to vary with the

type and the amount of solute present in the pure Mg. Overall, decreasing grain size with increasing solute content was observed in all of the binary alloys. The increased amount of solute in Mg generated constitutional undercooling in a diffusion layer ahead of the advancing solid/liquid interface [47]. Grain growth was therefore restricted given that the diffusion of the solute occurred slowly and the rate of crystal growth decreased. Additional nucleation probably occurred in the constitutionally undercooled zone given that the existing nucleants had a better chance of surviving and acting as nucleating sites.

The individual effect of solute elements on grain refinement can be better explained using the growth restriction factor (GRF), Q. This factor can be calculated using the binary phase diagrams and is defined as $Q = m_L C_o (k - 1)$, where m_L is the slope of the liquidus line, k is the distribution coefficient (C_s/C_L), and C_o is the solute content. This equation is only applicable for solutes present in dilute concentration levels and it helps explain the grain size differences observed in the solid solution alloys, Mg-Li, Mg-In and Mg-Zn.

Of all the solutes, it was observed that Zn decreased the grain size of Mg even at low solute levels, while the Li and the In solute content had to be increased in order to achieve the same degree of grain refinement found in the Mg-Zn alloys. Grain structures for Mg-In and Mg-Zn alloys with a similar solute content are found in Figure 5.10.

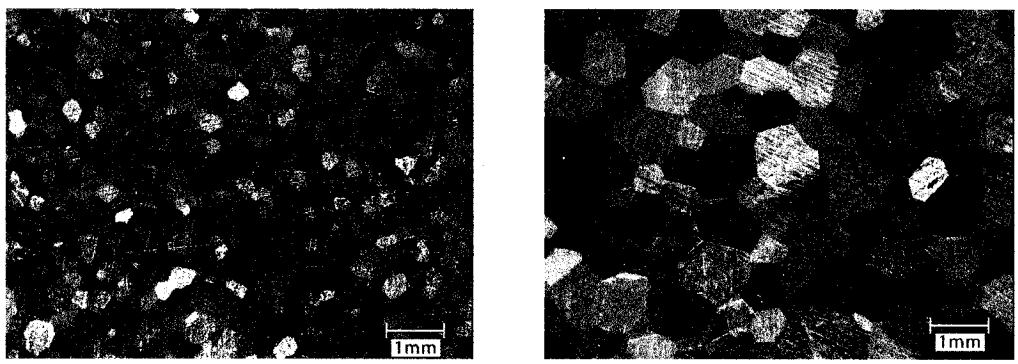

Figure 5.10: Comparison of grain structures of (a) Mg-0.2Zn (0.190 at% Zn) and (b) Mg- 0.2 In (0.206 at% In). Alloys contain different solutes, but similar solute content

The Mg-In alloy (Figure 5.10b) with solute content of 0.206 at% In has a grain size of 501 μm, while the Mg-Zn alloy (Figure 5.10a) with lower solute content of 0.190 at% Zn has a much smaller grain size of 210 μm. The reason why Zn grain refines the microstructure of Mg alloys much better than In is because it has a higher GRF value, hence it restricts growth much better than elements with low GRF values such as In. Determination of GRF values using binary phase diagrams for various solutes in Mg has been carried out in previous research and can be found in Table 5.4.

Table 5.4: Slope of liquidus line (m), distribution coefficient (k), and growth restriction factor m (k – 1) for various alloying elements in Mg [44]

Element	m	k	m (k – 1)
Zr	6.90	6.55	38.29
Ca	- 12.67	0.06	11.94
Si	- 9.25	≈ 0.00	9.25
Ni	- 6.13	≈ 0.00	6.13
Zn	- 6.04	0.12	5.31
Cu	- 5.37	0.02	5.28
Ge	- 4.41	≈ 0.00	4.41
Al	- 6.87	0.37	4.32
Sc	4.02	1.99	3.96
Sr	- 3.53	0.006	3.51
Ce	- 2.86	0.04	2.74
Yb	- 3.07	0.17	2.53
Y	- 3.40	0.50	1.70
Sn	- 2.41	0.39	1.47
Pb	- 2.75	0.62	1.03

From the table it can be seen that Zr, Ca, and Si have the largest GRF values. This is indicative of better growth restriction and more effective grain refinement even when these elements are added at low solute levels [47]. Of all the elements the highest GRF value corresponds to Zr, demonstrating that this solute has an amazing grain refining ability and explaining why this element is often used as grain refiner in Mg based alloys.

Growth restriction factors for Zn and Ce are found in Table 5.4 and since Zn has a larger GRF than Ce, this alloying element is more effective restricting growth and refining the microstructure of Mg. Nevertheless, given the low solubility of Ce in Mg, second phases are formed which contribute to grain refinement. Growth restriction factors for Li and In are not found in the table, however from looking at the shape of the freezing range and the slope of liquidus line in their binary phase diagrams it is estimated that their GRF values would below those of Zn and Al. Hence, in order for these elements to achieve a similar grain size reduction to that achieved with Zn additions, the Li and In additions have to be significantly larger.

Presence of second phases was also identified as being an important factor in grain refinement. It was observed that for a solute such as Ce, where the solid solubility with Mg is extremely low, the formation of second phases was inevitable even at low solute content (Figure 4.27). The existing Ce-rich intermetallics might have acted as nucleation sites or as growth poisoners, resulting in a finer microstructure. Grain size of pure Mg reduced from 647 μm to 53 μm once 0.125 at% Ce was added.

The presence of second phases was also observed in the Mg-16Li alloy (Figure 4.6). According to the phase diagram, binary Mg-Li alloys are not expected to contain any intermetallics. However, the presence of impurities such as oxygen might promote the formation of the Mg-Li intermetallics like those observed in Figure 4.6. A finer microstructure in the highest Li containing alloy was in fact observed. Nevertheless the observed grain size reduction could have been

caused both by the increased solute content or the formation of the second phases. In any case, the effect of solute elements on grain size is as important as that of nucleant particles, since solute elements play a significant role in controlling the growth of nucleated grains and in subsequent nucleation [48].

5.6 Deformation tests

Deformation tests on the four alloy specimens revealed that the deformation characteristics of a metal are dependent on a series of factors. Some of which include crystal structure, grain size, temperature, strain, strain rate, etc. Results obtained with the samples rolled for 7 passes demonstrated that the as-cast grain structure may influence the rolllability and deformation of a metal. It was seen that large columnar grains, like those found in the pure Mg sample, are detrimental to rolling. When the sample is rolled, cracks appear along the grain boundaries of the columnar grains, as can be distinguished in Figure 5.11, where the macrographs of the grain structure and the rolled sample are compared.

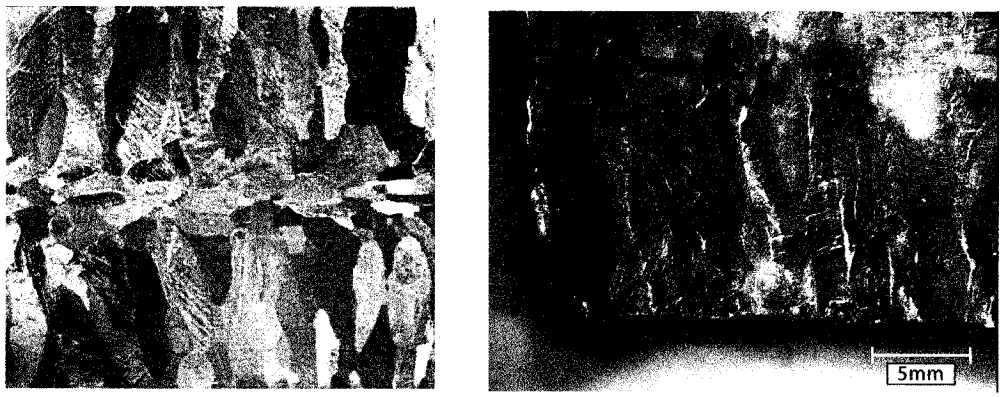

Figure 5.11: Pure Mg samples showing the (a) large columnar grain structure before rolling and the (b) resultant cracks along the grain boundaries after rolling at 150°C

On the other hand, alloys with a fine equiaxed as-cast grain size were found to be more rollable showing a smooth surface and smooth cross-section, with no visible cracks. Figure 5.12 shows the surface and cross-section of the Mg-3Al-1Zn rolled sample.

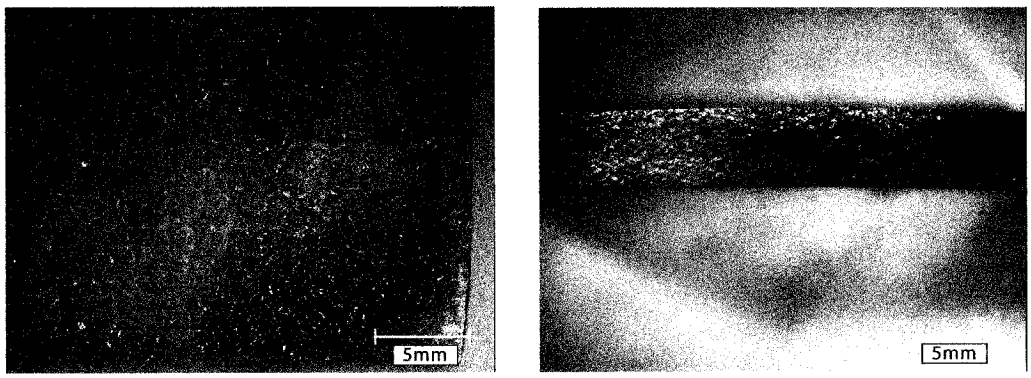

Figure 5.12: Mg-3Al-1Zn sample rolled for 7 passes at 150°C showing a smooth (a) rolled surface and smooth (b) rolled cross-section.

Rolling tests carried out to higher strains (15 passes) were found to be somewhat different from those carried out with lower strains. It was observed that the alloy with the lowest c/a ratio such as Mg-2Li-1Zn gave the best results even if its grain size was not as fine as that observed for Mg-3Al-1Zn. Somehow the Mg-3Al-1Zn sample always disintegrates (Figure 4.29) showing deep cracks along the surface and broken off ends. This behavior is not completely understood, but the presence of brittle second phases ($Mg_{17}Al_{12}$) may have a role. Further research on the rolling characteristics of these and other alloys needs to be carried out in order to give more accurate conclusions.

Overall, the microstructure of the alloys seemed to strongly correlate with the compression behavior. It was distinguished that if an alloy had a better quality microstructure (finer equiaxed grains), then the compression results gave more consistent flow curve shapes, as can be observed for Mg-3Al-1Zn (Figure 4.30b) and Mg-2Li-1Zn (Figure 4.30c). Furthermore, qualitative analysis of the compressed surfaces after 0.2 strain compression revealed that Mg-3Al-1Zn performed particularly well given that it had a smooth surface after compression. Conversely, the pure Mg sample with columnar grains was seen to fail even if it had a lower c/a ratio than the Mg-3Al-1Zn. A relationship between axial ratio and compression behavior was not observed on the compressed samples. A summary of the results obtained for the three alloys can be found in Table 5.5.

Table 5.5: Summary of Formability Results for the Three Alloys

Alloy	c/a	a-space (Å)	c-space (Å)	Grain Structure	Rolling		Compression Surface
					ε = 0.3	ε = 0.55	
Mg-1Zn-2Li	1.6190	3.2009	5.1823	E	G	VG	Dimpled Smooth
Mg	1.6240	3.2088	5.2111	C	P	P	Rough, sheared
Mg-1Zn-1In	1.6241	3.2069	5.2084	C + E	G	G	Moderately smooth
Mg-3Al-1Zn	1.6246	3.1993	5.1976	FE	VG	VG	Smooth

***Grain structure**: E = Equiaxed, C = Columnar, FE = Fine Equiaxed*
***Rolling:** VG = Very Good, G = Good, P = Poor*

Although the results obtained in this study are very interesting, the exact relationship between lattice parameters and deformation mechanisms is yet to be determined. The deformation characteristics of an alloy are dependent on a variety of parameters each of them important in their own way. Further work needs to be carried out where these parameters are monitored consistently both on commercial and experimental Mg alloys. TEM analysis of the interplanar spacings, burgers vectors, and CRSS of the non-basal planes would shed some light on the effects the different solutes have on formability. Additionally, single crystal studies would eliminate the grain size effect and would help understand the relationship of the Mg crystal structure and the deformation behavior of the Mg based alloys.

CHAPTER 6 - CONCLUSIONS

1) The hcp crystal structure of Mg could be altered through solid solution alloying with Li, In, Zn, and Ce. It was seen that lattice parameters expand or contract depending on the size of the solute or the number of its valence electrons.

2) A solute size difference effect was observed for Mg binary alloys containing a Zn concentration ranging from 0.2 at% to 0.72 at%. Addition of Zn to pure Mg contracted both the a- and c-spacing due to its smaller atomic (metallic) size with respect to Mg. Both lattice parameters contracted proportionally leaving the axial ratio unchanged.

3) Addition of 0.06 at% Ce caused a small change in the lattice parameters conceivably due to its large solute size difference with respect to Mg. However, these lattice parameter changes are difficult to measure given the low solubility of Ce in Mg. In Mg-Ce binary alloys, Ce-rich precipitates were found to be precipitating along the grain boundaries as well as inside the grains. Determination of an accurate amount of dissolved Ce in Mg was not possible given that precipitates are found even at low solute levels.

4) Lattice parameter changes attributable to the modification of the unit cell electronic concentration are found in Mg-Li and Mg-In binary alloys.

5) Addition of Li (2.3 at% - 16 at%) to Mg decreased the electronic concentration, causing a contraction of both lattice dimensions. Li caused the c-spacing to contract much more than the a-spacing and hence a decrease of the axial ratio occurred.

6) Increasing the concentration of In (0.1 at% - 0.3 at%) in Mg caused an increase of the axial ratio conceivably due to a increase in electronic concentration (e/a).

7) Modifications to the lattice dimensions of the hcp structure in Mg-In alloys could be attributed to a combination of a solute size and valency effect. At low In concentrations, changes in lattice parameters can be associated with atomic size differences, where a larger atomic (metallic) size of In expands the lattice in both directions. As the In concentration increased a lattice parameter contraction was seen, presumably due to the fact that the bond type changes from metallic to covalent. This lattice parameter contraction is much less than expected and can be explained by the competition of the two factors, i.e: increasing electronic concentration of the unit cell that expands the lattice and the size effect that contracts it.

8) The critical concentration where In causes electron overlap along the B face of the Brillouin zone causing the expansion of the c-spacing was found to be 2.3 at%.

9) Linear functions obtained when lattice parameters were plotted against the solute atomic % found that that the slope of the line is dependent on the individual effect that the solute (solute size, valence or both) on the parameter. While the intercept is proportional to the purity of the starting pure Mg used to make the alloys.

10) An empirical relationship, between the axial ratio (c/a) and the electronic concentration (e/a) of Mg hcp alloys was determined to be:

$$c/a = -0.34(e/a)^2 + 1.38(e/a) + 0.20$$

11) Multicomponent alloys prepared with combinations of the studied solute elements (0.3 wt% Ce, 1.0 wt% In, 1 wt% Zn and 2 wt% Li) were found to behave similarly to the binary alloys in terms of lattice parameter and axial ratio changes. Alloys containing Li were found to be the only alloys with an axial ratio change. Alloys containing In did not exhibit any axial ratio change since at 1 wt%, In does not increase the electronic concentration to an extent where the axial ratio changes.

12) Interplanar spacing modifications were found to follow the same trend as the changes observed for the lattice parameters. Hence, if a solute caused an expansion of the lattice parameters, the interplanar spacing was also observed to expand. Changes to the basal {0002} d-spacing were always one half the changes of the c-spacing. On the other hand, the $\{10\bar{1}0\}$ prismatic and the $\{1\bar{1}22\}$ pyramidal d-spacings were affected by both the a- and c-spacing.

13) It is known that activation of non-basal slip can occur if the CRSS for non-basal planes decreases (i.e. d-spacing increase) or if the CRSS of the basal plane increases (d-spacing decrease). Non-basal d-space increase was seen for In additions up to 0.25 at% and a basal d-space decrease was seen with an indium concentration that lies between 2 at% and 10 at%. These concentrations have the potential of activating some non-basal slip and change the balance of deformation mechanisms, making the texture of rolled sheet more random.

14) As-cast grain structure influences the rollability and deformation of a metal. A homogeneous equiaxed grain structure is preferred since it makes the metal more rollable and less prone to cracking along the edges. Among the solutes studied, Zn grain refined the structure of Mg much better than In or Li given its high growth restriction factor (GRF). A high GRF is indicative of better growth restriction and more effective grain refinement even when added at low solute levels.

15) Additionally, presence of second phases in Mg-Ce alloys also caused grain refinement of Mg. Ce-rich intermetallics can either act as nucleation sites or poisons growth of new grains.

16) Microstructure of the alloys was also found to strongly correlate with the compression behavior of the alloy. Where a better quality (fine equiaxed) grain structure gave more consistent flow curve shapes and a smoother compressed sample surface.

CHAPTER 7 - SUGGESTIONS FOR FUTURE WORK

1) XRD tests with larger range of compositions, supersaturated samples and additional solute elements should be carried out to determine their effects on lattice parameters.

2) High temperature XRD or neutron diffraction analysis can be carried out to see the effects of solutes on the lattice parameters at elevated temperatures. These would be important for hot deformation behavior of magnesium alloys.

3) Systematic studies of other multicomponent alloys prepared with two or three alloying additions are required. EPMA should be carried out on these alloys to determine the amount of solute present in solid solution and how the solubility of each solute is affected when solutes are mixed.

4) Single crystal studies on binary and multicomponent alloys would eliminate the grain size effect on deformation and shed some light on the relationship of the lattice parameters and their effect on the deformation characteristics.

5) TEM analysis of the alloys where interplanar spacing, burgers vectors, and activation of basal and non-basal slip would be important in elucidating the effect of axial ratio and lattice parameter changes on deformation.

6) Longer term work can address a systematic investigation to determine the individual and combined influences of parameters temperature, microstructure, lattice parameters, strain, strain rate, texture, and alloying elements.

7) Tensile tests are required to determine the formability of the alloys. These tests can then be compared to rolling and compression tests to study the different deformation mechanisms.

REFERENCES

[1] E.F. Emley, Principles of Magnesium Technology, Pergamon Press, London, 1966.

[2] K.H. Matucha, "Structure and Properties of Non Ferrous Alloys", Materials Science and Technology: A Comprehensive Treatment; Vol. 8, ed, R.W. Cahn, P. Haasen, E.J. Kramer, VCH, Weinheim; New York; Basel; Cambridge; Tokyo, Vol. 8, 1996.

[3] I.J. Polmear, "Light Alloys, Metallurgy of the Light Metals", Metallurgy & Materials Science Third Edition, Arnold, a division of Hodder Headline PLC, 1995, pp.196-247.

[4] B.L.Mordike and T. Ebert, "Magnesium Properties-applications-potential", Mat. Scie and Eng, A302, 2001, pp 37-45.

[5] M. Avedesian and H. Baker ed., ASM Specialty Handbook: Magnesium and Magnesium Alloys. ASM International, Ohio, 1999

[6] K.U. Kainer and F. von Dutch, "The Current State of Technology And Potential for further Development of Magnesium Applications." Magnesium Alloys and Technologies, ed, K.U.Kainer, Wiley-VCH Verlag GmbH & Co. KGaA, Weinheim, 2003, pp. 1-22

[7] K. Scheme and E. Hornbogen, "Rapidly Solidified Mg-Li Base Superlight Alloys." Proceedings of the International Conference on Light Metals, ed, T. Khan, G.Effenberg, ASM International, Amsterdam, 1990, pp 797-803.

[8] G.V. Raynor, The Physical Metallurgy of Magnesium and its Alloys, Pergamon Press, New York, 1959

[9] Magnesium Electron Website. www.magnesium-elektron.com

[10] R. Gradinger and P. Stolfig, "Magnesium Wrought Alloys for Automotive Applications." Magnesium Technology 2003, ed., H. I. Kaplan, TMS 2003.

[11] S.R. Agnew, "Wrought Magnesium: A 21st Century Outlook." TMS, Vol. 56 2004, No. 5, pp. 20-21

[12] H. Friedrich and S. Schumann, " Research for a new age of magnesium in the automotive industry", Journal of Materials Processing Technology, Vol. 117, 2001, pp. 276-281.

[13] F. Moll, M. Mekkaoui, S. Schumann and H. Friedrich, "Application of Magnesium Sheets in Car Body Structures." Magnesium: Proceedings of the 6th International Conference Magnesium Alloys and Their Applications. Ed, K.U. Kainer, Germany, pp. 936-942

[14] E. Doege and K. Droder, "Sheet metal forming of magnesium wrought products – formability and process technology" Journal of Materials Processing Technology. 115, 2001, pp 14-19

[15] A. Staroselsky and L. Anand, "A constitutive model for hcp materials deforming by slip and twinning: application to magnesium alloy AZ31B" , International Journal of Plasticity, Vol 19, 2003 p.

[16] F.J. Humpreys and M. Hatherly, Recrystallization and Related Annealing Phenomena, 2nd Ed, Pregamon Press, Oxford, 2004.

[17] M.D, Nave and M.R. Barnett, "Microstructures and textures of pure magnesium deformed in plane-strain compression" Scripta Materialia, Vol 51, 2004, pp. 881-885.

[18] E.A. Ball and P.B. Prangell, "Tensile-Compressive Yield Asymmetries in High Strength Wrought Magnesium Alloys", Scripta Metallurgica Materialia, Vol. 31, 1994, pp. 111-116.

[19] S. Ando and H. Tonda, "Non-Basal Slips in Magnesium and Magnesium-Lithium Alloy Single Crystals." Materials Science Forum, Vols 350-351 2000, pp. 43-48

[20] O. Duygulu and R. Agnew, " The Effect of Temperature and Strain Rate on Tensile Properties of Textured Magnesium Alloy AZ31B Sheet", Magnesium Technology 2003, ed., H. Kaplan, TMS 2003, pp. 237-242

[21] H. Somekawa and M.Kohzu, S. Tanabe and K.Hogashi, "The Press Formability of Alloy AZ31", Materials Science Forum, Vols. 350-351 2000, pp 177-182

[22] H.J. McQueen and D.L.Bourell, J. Mat. Shaping Tech, 5, 1987, p 53.

[23] M. Barnett, private presentation, McGill University, 2004

[24] S. Agnew and O. Duygulu, "A Mechanistic Understanding of the Formability of Magnesium: Examining the Role of Temperature on the Deformation Mechanisms." Materials Science Forum Vols. 419-433, 2003, pp. 177-188

[25] G. Sambasiva and Y.V.R.K. Prasad, "Strengthening Mechanisms in Hot-Rolled Magnesium and Magnesium Alloys" Materials Letters, Vol. 1, No 5, 6, 1983, pp. 171-17

[26] M.A. Meyers, O. Vohringer, V.A. Lumbarda, Acta Materiala, 49, 2001, pp. 4025.

[27] M. R. Barnett, "Inflluence of grain size on the compressive deformation of wrought Mg-3Al-1Zn", Acta Materiala 52, 2004, pp. 5093-5103.

[28] H. Haferkamp, M. Niemeyer, R. Boehm, U. Holzkamp, C. Jaschik and V. Kaese, "Development, Processing and Applications Range of Magnesium Lithium Alloys", ", Materials Science Forum Vols. 350-351, 2000, pp 31-42

[29] T.Mukai, M. Yamanoi and K. Higashi, "Ductility Enhancement in Magnesium Alloys under Dynamic Loading", Materials Science Forum Vols. 350-351, 2000, pp 97-102

[30] Z. Drozd, Z. Trojanova and V. Gartnerova, "Deformation Behavior of Mg-Li Alloys at Room and Elevated Temperatures." Magnesium: Proceedings of the 6th International Conference Magnesium Alloys and Their Applications. Ed, K.U. Kainer, Germany, pp. 936-942

[31] F. W. Bach, M. Schaper and C. Jaschik, " Influence of Lithium on hcp Magnesium Alloys", Materials Science Forum Vols. 419-422, 2003, pp1037-1042

[32] V. Singh, R.K.Singh and C.R. Chakravorty, "Ultra Light Alloys for Aerospace Applications", 35th Annual Convention of the Institute of Indian Foundrymen, India, 1986, pp 49-51

[33] Phase Diagrams of Binary Magnesium Alloys, AA. Nayed-Hashemi and J.B. Clark, EDS, ASM Metals Park, Ohio, USA, 1988.

[34] F.E. Hauser, P.R. Landon and J.E Dorn, Trans. ASM, 50, 1958, pp. 856.

[35] W. Hume-Rothery, Electrons, Atoms, Metals, and Alloys, Dover Publications, Inc., New York, 1963.

[36] W. Hume-Rothery and G.V. Raynor,The Structure of Metals and Alloys, 3rd Edition, London, Institute of Metals, 1956.

[37] W.B. Pearson, A Handbook of Lattice Spacings and Structures of Metals and Alloys, Pergamon Press,Oxford, London, Edinburgh, New York, Paris, Frankfurt, 1958

[38] D.S. Clark and W.R. Varney, Physical Metallurgy for Engineers, D.Van Nostrand Company, Inc, Princeton, New Jersey, New York, 1962

[39] F.W. von Batchelder and R.F. Raeuchle, "Lattice Constants and Brillouin Zone Overlap in Dilute Magnesium Alloys" Physical Review, Vol 105, No 1, (1957),pp 59-61

[40] R.S Busk, "Lattice Parameters of Magnesium Alloys", Journal of Metals, Transactions AIME, Vol 188, (1950), pp 1460-1464

[41] G.V. Raynor, "The Lattice Spacings of the Primary Solid Solutions of Silver, Cadmium, and Indium in Magnesium', Proc. Roy. Soc, Vol.174, No.959, (1940), pp.457-471.

[42] B.D. Cullity and S.R. Stock, Elements of X-ray Diffraction, 3rd Ed, Prentice Hall, New Jersey, 2001.

[43] Pure Magnesium Standard 004-0770

[44] V.K. Pecharsky and P.Y. Zavalij, Fundamentals of Powder Diffraction and Structural Characterization of Materials, Kluwer Academic Publishers, Boston, 2003.

[45] Annual Book of ASTM Standards, Vol. 03.01, ASTM, Philadelphia, 2000.

[46] E. Teatum, K. Gschneidner, and J. Waber, 1960, LA-2345, U.S. Department of Commerce, Washington, D.C.

[47] Y.C Lee, A.K Dahle, and D.H. StJohn, "The Role of Solute in Grain Refinement of Mg", Metallurgical and Materials Transactions , Vol 31A, (2000), pp. 2895

[48] M. Easton and D. StJohn: Metall. Mater. Trans A, 1999, vol 30A, pp 1613-23.

APPENDIX A

Preliminary XRD results were obtained on powder samples. Both fine and course pure magnesium powder samples were tested (Figure A.1).

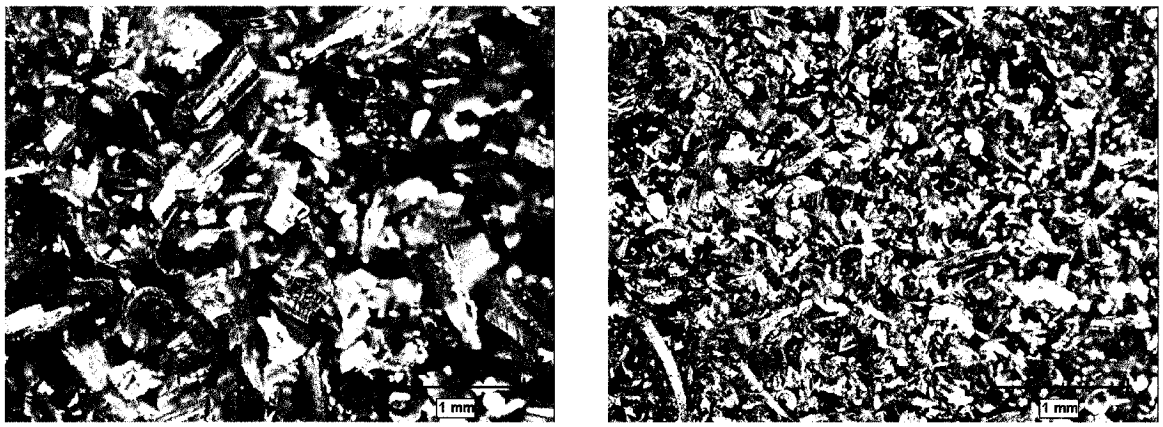

(a) (b)

Figure A.1: Macrographs of (a) coarse and (b) fine pure magnesium powder

Table A.1 lists the calculated lattice parameters for pure magnesium solid and powder samples. Standard values are also given in the table. Fine powder gives the most accurate value with a 0.03% difference from the standard.

Table A.1: Lattice Parameters for Pure Magnesium Solid and Powder Samples

Condition	a	c	c/a calc	c/a ref	% Ref
Solid	3.2089	5.2036	1.6216	1.6237	0.2068
Coarse	3.2035	5.2056	1.6250	1.6237	-0.1308
Fine	3.2086	5.2109	1.6240	1.6237	-0.0328